

**Vibration-induced mobilization of trapped non-aqueous  
phase liquids in porous media**

by

**Wenqing Li**

A dissertation submitted to the graduate faculty  
in partial fulfillment of the requirements for the degree of

**DOCTOR OF PHILOSOPHY**

Major: Chemical Engineering

Program of Study Committee:  
R. Dennis Vigil (Major Professor)

James C. Hill

Derrick K. Rollins

Igor A. Beresnev

J. Adin Mann

Iowa State University

Ames, Iowa

2006

Copyright © Wenqing Li, 2006. All rights reserved.

UMI Number: 3229099

### INFORMATION TO USERS

The quality of this reproduction is dependent upon the quality of the copy submitted. Broken or indistinct print, colored or poor quality illustrations and photographs, print bleed-through, substandard margins, and improper alignment can adversely affect reproduction.

In the unlikely event that the author did not send a complete manuscript and there are missing pages, these will be noted. Also, if unauthorized copyright material had to be removed, a note will indicate the deletion.

**UMI**<sup>®</sup>

---

UMI Microform 3229099

Copyright 2006 by ProQuest Information and Learning Company.

All rights reserved. This microform edition is protected against unauthorized copying under Title 17, United States Code.

ProQuest Information and Learning Company  
300 North Zeeb Road  
P.O. Box 1346  
Ann Arbor, MI 48106-1346

Graduate College  
Iowa State University

This is to certify that the doctoral dissertation of  
Wenqing Li  
has met the dissertation requirements of Iowa State University

Signature was redacted for privacy.

**Major Professor**

Signature was redacted for privacy.

**For the Major Program**

## TABLE OF CONTENTS

ABSTRACT.....	v
CHAPTER 1. INTRODUCTION .....	1
1.1. Background .....	1
1.2. Dissertation organization .....	2
1.3. References.....	3
CHAPTER 2. GENERAL CONCEPTS .....	5
2.1. Application background .....	5
2.2. Dissolution study of trapped immiscible ganglia.....	6
2.3. Traditional remediation technology .....	6
2.4. The elastic wave stimulation technology .....	7
2.5. The capillary-physics mechanism.....	9
2.6. References.....	11
2.7. Figure captions.....	13
CHAPTER 3. REVIEW OF TWO-PHASE FLOW NUMERICAL SIMULATIONS .....	18
3.1. Introduction to two-phase flow .....	18
3.2. Modeling separated flow.....	19
3.3. Modeling dispersed flow.....	23
3.4. Modeling packages .....	25
3.5. Motivation of the research .....	28
3.6. References.....	28
CHAPTER 4. VIBRATION-INDUCED MOBILIZATION OF TRAPPED OIL GANGLIA IN POROUS MEDIA: EXPERIMENTAL VALIDATION OF A CAPILLARY-PHYSICS MECHANISM .....	31
Abstract.....	31
4.1. Introduction .....	32
4.2. Experimental apparatus and protocol.....	34
4.3. Results and discussion .....	36
4.4. Summary .....	39
4.5. Acknowledgements.....	40
4.6. References.....	40
4.7. Figure captions.....	42

CHAPTER 5. VIBRATION-INDUCED MOBILIZATION OF TRAPPED OIL GANGLIA IN POROUS MEDIA: DROPLET FLOW AND STIMULATION EFFECTS IN A REALISTIC CONVERGENCE DIVERGENCE CHANNEL.....	51
Abstract .....	51
5.1. Introduction .....	53
5.2. Problem formulation and numerical method .....	55
5.3. Results and discussion .....	60
5.4. Summary .....	67
5.5. Acknowledgements.....	67
5.6. References.....	68
5.7. Table and figure captions.....	68
 CHAPTER 6. DROPLET BREAKUP DRIVEN BY INTERFACIAL TENSION IN CONSTRICTED CAPILLARY TUBES.....	 85
Abstract .....	85
6.1. Introduction .....	86
6.2. Criterion to initiate droplet breakup.....	88
6.3. Problem formulation and numerical method .....	90
6.4. Results and discussion .....	91
6.5. Summary .....	97
6.6. References.....	98
6.7. Table and figure captions.....	98
 CHAPTER 7. CONCLUSIONS .....	 115
7.1. Summary .....	115
7.2. Recommendations for future studies .....	117
 APPENDIX. PAPER: ELASTIC WAVES PUSH ORGANIC FLUIDS FROM RESERVOIR ROCK .....	 120
 ACKNOWLEDGEMENTS.....	 121

## ABSTRACT

Acoustic wave stimulation, such as vibration-induced mobilization, is a promising enhancement approach to remove trapped NAPLs (Non-Aqueous Phase Liquids) usually encountered in multiphase flows through porous media, especially the remediation of underground water contamination and incomplete petroleum recovery from oil reservoirs, with advantages of high efficiency, low cost and environmental safety relative to traditional mobilization methods.

According to a simple hypothesized capillary-physics mechanism, specific predictions can be deduced that vibration will be the most effective in mobilizing trapped non-aqueous phase liquids with a comparative higher acceleration amplitude and lower vibration frequency.

Quasi-two-dimensional glass micro-model experiments were carried out and it was shown that for fixed acceleration amplitude TCE (trichloroethylene), the trapped organic phase, was more quickly displaced as the vibration frequency decreased from 60 *Hz* to 10 *Hz*. And for fixed vibration frequency, TCE displacement became more and more efficient as the acceleration amplitude increased from 0.5  $m/s^2$  to 5.0  $m/s^2$ .

Moreover, numerical simulations were performed using FLUENT to investigate single droplet flow and the related stimulation effects of vibration. Implementing vibration was demonstrated to be more helpful and efficient to mobilize a trapped droplet in capillary tubes. For fixed acceleration amplitude, the efficiency increases as the vibration frequency decreases from 50 *Hz* to 10 *Hz*. For fixed vibration frequency, the average bulk flow rate increase and the time necessary to mobilize the trapped droplet decrease as the acceleration amplitude increase.

In addition, analysis of droplet breakup in constricted capillary tubes driven by interfacial tension was performed. A criterion was derived to determine whether droplet breakup could be initiated in sinusoidally constricted tubes, and was further validated by simulations and published data. Droplet breakup was shown to be strongly dependent on the shape of the constriction, viscosity ratio, and interfacial tension, but not on density ratio.

In all, the work together with the capillary physics mechanism can make it possible to understand the physics of the mobilization effect of low frequency vibration, which can then be applied to the predictions of the stimulation effect in the field after further full parameter space investigations are performed.

# CHAPTER 1. INTRODUCTION

## 1.1. Background

Multiphase flow in porous media is a complicated phenomenon not yet completely understood, but with important applications, especially in the field of engineering. For example, multiphase flow processes are usually encountered in groundwater. Organic solvents enter an aquifer due to leakage from underground tanks, pipeline ruptures, or accidental surface spills of industrial or agricultural waste; hence, they form contamination of underground aquifers. Another example is in the area of petroleum engineering, in which immiscible residual oil is displaced by water from a reservoir or via water flooding. There are an abundance of experimental and theoretical investigations on multiphase flow, especially the cases such as using an immiscible liquid displacement to enhance oil recovery and finding a more efficient way to remove organic contamination in underground water (Abad-Guerra, 1976; Beresnev and Johnson, 1994; Bradford, *et al.*, 1998; Dobronravov, 2002; Medlin, *et al.*, 1983; Melrose and Brandner, 1974; Mohanty, *et al.*, 1980; Payatakes *et al.*, 1980; Payatakes, 1982).

A common feature of liquid-liquid flow in porous media is the capillary entrapment of dispersed phase. A variety of solutions for mobilizing trapped organic phase have been used, which include but are not restricted to water flooding (pump and treat technology), adding surfactants to lower interfacial surface tension, increasing dissolution of dispersed phase with cosolvents, using electro-osmosis, biological remediation, and exerting elastic waves on the system. Among the approaches to mobilize trapped unwanted organic phase, the elastic wave stimulation is considered to be a very promising means in terms of efficiency, cost, and environmental safety compared with commonly used traditional methods.

One of the most comprehensive reviews of elastic wave stimulation was written by Beresnev and Johnson (1994). Anecdotal evidence has suggested that elastic waves improve permeability of fluids, hence mobility. However, until recently have well-controlled laboratory experiments demonstrated this effect (Roberts *et al.*, 2001). Field-scale studies

have also shown promising results when seismic waves were applied to whole reservoir. Recently a great deal of work has also been done to discern possibility of enhanced petroleum recovery using elastic waves (Hilpert *et al.*, 2000; Roberts *et al.*, 2001, 2003; Poesio *et al.*, 2002). Several mobilization mechanisms, based on the effect of elastic waves to overcome capillary forces by which the dispersed phase was trapped, were proposed by Graham and Higdon (2000), Hilpert *et al.* (2000), Iassonov and Beresnev (2003) and Beresnev *et al.* (2005). However, the capillary-physics mechanism of elastic wave stimulation proposed by Beresnev *et al.* (2005) is one of the most promising explanations for mobilization and flow enhancement of trapped dispersed phase under the implementation of elastic waves, such as vibration.

This research is composed of three major parts. The first part involves the experimental validation of the potential capillary-physics mechanism in terms of the overall vibratory stimulation effects using a two-dimensional glass micro-model. The second part continues the study further from the perspective of a single trapped droplet in a typical capillary tube using a computational fluid dynamics method to not only verify the flow enhancement effect but also to discern more mechanism-related details, and the effect of some other factors as well. The third part studies droplet breakup and its dynamics driven by interfacial tension only in constricted capillary tubes, which lays the foundation for further combined elastic wave stimulation study of oscillatory forcing and breakup.

## **1.2. Dissertation organization**

The goals of this research are to verify and hence better understand the capillary-physics mechanism of trapped dispersed phase mobilization and flow enhancement in a capillary tube or a porous network by using vibratory forcing, a kind of elastic wave, as well as preliminary study of droplet breakup in a capillary tube driven by interfacial tension. The dissertation is divided into several chapters. Chapter 2 contains a thorough review of previous work and more background information emphasizing the related theories and experimental studies. Chapter 3 focuses on the numerical simulation review of two-phase flow. Chapter 4 consists of a published paper: Vibration-induced mobilization of trapped oil

ganglia in porous media: Experimental validation of a capillary-physics mechanism. Chapter 5 is a manuscript which describes further study of vibratory-induced mobilization of trapped oil ganglia in porous media, especially the droplet flow and stimulation effects in a more realistic convergence divergence channel which is much closer to an on-site application. Chapter 6 is a manuscript on droplet breakup and its dynamics in constricted capillary tubes driven by interfacial tension. Chapter 7 reaches the general conclusions from this research and recommendations for future work.

### 1.3. References

- Abad-Guerra, B.P., (1976). Methods for restoring productivity to gas wells in the Clinton sand of Ohio: A laboratory and field experiment: Ph.D. thesis. Pennsylvania State University.
- Beresnev, I.A., and Johnson, P.A., (1994). Elastic-wave stimulation of oil production: A review of methods and results. *Geophysics*, 59(6), 1000-1017.
- Beresnev, I.A., Vigil, R.D., Li, W., Pennington, W.D., Turpening, R.M., Iassonov, P.P., and Ewing, R.P., (2005). Elastic waves push organic fluids from reservoir rock. *Geophysical Research Letter*. 32(13), L13303, doi:10.1029/2005GL023123.
- Bradford, S.A., Abriola, L.M., Rathfelder, K.M., (1998). Flow and entrapment of dense nonaqueous phase liquids in physically and chemically heterogeneous aquifer formations. *Advances in Water Resources*, 22(2), 117-132.
- Dobronravov, O.V., (2002). A new technology of reservoir stimulation through exposure to weak seismic waves. *First Break*, 20, 376-382.
- Graham, D.R., and Higdon, J.J.L., (2000). Oscillatory flow of droplets in capillary tubes. Part 2. Constricted tubes. *Journal of Fluid Mechanics*, 425, 55-77.
- Hilpert, M.; Jirka, G.H., and Plate, E.J., (2000). Capillarity-induced resonance of oil blobs in capillary tubes and porous media. *Geophysics*, 65(3), 874-883.
- Iassonov, P.P., and Beresnev, I.A., (2003). A model for enhance fluid percolation in porous media by application of low-frequency elastic waves. *Journal of Geophysics Research*, B 108(3), 2138.

- Medlin, W.L., Masse, L., and Zumwalt, G.L., (1983). Method for recovery oil by means of a gas drive combined with low amplitude seismic excitation: USA Patent 4 417 621.
- Melrose, J.C., and Brandner, C.F., (1974). Role of capillary forces in determining microscopic displacement efficiency for oil recovery by waterflooding. *Journal of Canadian Petroleum Technology*, 13(4), 54-62.
- Mohanty, K.K., Davis, H.T., and Scriven, L.E., (1980). Physics of oil entrapment in water-wet rock, SPE 9406.
- Payatakes, A.C., Ng, K.M., and Flumerfelt, R.W., (1980). Oil ganglion dynamics during immiscible displacement: model formulation. *AIChE Journal*, 26(3), 430-443.
- Payatakes, A.C., (1982). Dynamics of oil ganglia during immiscible displacement in water-wet porous media. *Annual Review of Fluid Mechanics*, 14, 365-393.
- Poesio, P., Ooms G., and Barake, S., (2002). An investigation of the influence of acoustic waves on the liquid flow through a porous material. *The Journal of the Acoustical Society of America*, 111(5), 2019-2025.
- Roberts, P.M., Sharma, A., Uddameri, V., Monagle, M., Dale, D.E., and Steck, L.K., (2001). Enhanced DNAPL transport in a sand core during dynamic stress stimulation. *Environmental Engineering Science*, 18(2), 67-79.
- Roberts, P.M., Esipov, I.B., and Majer, E.L., (2003). Elastic wave stimulation of oil reservoirs: Promising EOR technology? *The Leading Edge*, 22(5), 448-453.

## CHAPTER 2. GENERAL CONCEPTS

### 2.1. Application background

In the field of environmental engineering, several investigations have indicated that organic chemicals are the main substances causing extensive and severe water contamination. Moreover, many organic pollutants are hydrophobic; so, they generally form separate non-aqueous phases rather than immediately dissolve into the groundwater. These fluids are usually referred to as Non-Aqueous Phase Liquids (NAPLs).

Although the concentrations of NAPLs in groundwater are small, the solubilities of most NAPLs are still high enough to severely degrade drinking water quality. For example, the solubility of TCE (trichloroethylene) in contaminated water is around  $10^{-3}$  mg/L, which is about  $10^5$  times the maximum concentration limit in drinking water (Pankow and Cherry, 1996). Moreover, most NAPLs dissolve extremely slowly, so they lead to long-term water contamination. So far, what we can do is to either remedy the polluted water or monitor it while natural processes accomplish the cleaning (Krupka and Martin, 2001). In addition, some researchers are working on special approaches to remove NAPL effectively, such as Reddi and Challa (1994), and Reddy and Saichek (2003).

In the field of petroleum engineering, roughly 60% of crude oil in trapped reservoirs remains trapped in small pores. Hence, the enhancement of oil mobility and recovery is an important issue as the worldwide demand for petroleum rises.

There are many forces that control the trapping and mobilization of NAPL, such as capillary, viscous, and buoyancy forces. NAPL will be generally trapped when capillary forces overweight the sum of viscous and buoyancy forces. In addition, many factors affecting the process of trapping and mobilization include the properties of the porous media (for example, the shape, size, and wetting behavior of porous media), the fluid properties (for example, the density, viscosity, interfacial tension between the fluids, the phase behavior of the fluids, the contact angle between fluids and porous media), the pressure gradient, and gravity etc. (Morrow and Songkran, 1981).

To remove the NAPL effectively it is necessary to study the dissolution process of NAPL in porous media. Dissolution of NAPL is the result of a number of factors, which include the characteristics of porous media (especially, the interfacial area), the fluid properties as well as the aqueous flow field, the flow rate, and the ganglia geometry.

## **2.2. Dissolution study of trapped immiscible ganglia**

Many models have been built to simulate the trapping, mobilization, breakup, and dissolution behavior of NAPL in some specific fields (Lowry and Miller, 1995; Hunt *et al.*, 1988; Geller and Hunt, 1993). At the same time, a series of experimental techniques were designed to study the behavior of NAPL in porous media and to elucidate the mechanisms and controlling factors of the process. These techniques include column dissolution studies (Miller *et al.* 1990), invasive technique (also called *in situ* polymerization technique, Conrad *et al.*, 1992; Powers *et al.*, 1992, & 1994), non-invasive techniques (also called dynamic two-dimensional and three-dimensional methods), etc. The commonly used techniques are dynamic three-dimensional methods rather than two-dimensional methods (Wilson *et al.*, 1990), which usually miss some key controlling factors. The dynamic three-dimensional techniques include NMR (Nuclear Magnetic Resonance) imaging technique (Baldwin and Gladden, 1996), Gamma attenuation technique (Imhoff *et al.*, 1994), X-ray tomography technique (Imhoff *et al.*, 1996), PIV (Particle Image Velocimetry) technique, PTV (Particle Tracking Velocimetry) technique (Rashidi and Dickenson, 1996), PVI (Photoluminescent Volumetric Imaging) technique (Montemagno and Gray, 1995), and PLIF (Planar Laser Induced Fluorescence, Fontenot and Vigil, 2002; Chen and Wada, 1986).

## **2.3. Traditional remediation technology**

A number of remediation techniques have been invented to tackle the prevalent problem: the long-term contamination of NAPL in underground water. These techniques consist of, but are not restricted to, pump-and-treat method, water flooding, bio-remediation, electro-osmotic flow enhancement, and enhanced recovery using surfactants or cosolvents.

These techniques are based mainly on increasing the NAPL solubility or decreasing the capillary forces or contact area of NAPL with water.

However, each technique has its disadvantages and limited effectiveness with either prohibitive expense and time or perhaps causing secondary contamination. No single method has been found to completely remove contaminant NAPLs from groundwater systems effectively. For example, the pump-and-treat technique undergoes the following processes: the contaminated water is pumped out of the ground and treated; the clean water is released back to the ground. Although the pump-and-treat technique is easy to understand, it is not only expensive and slow but also not effective in many situations (Pankow and Cherry, 1996) since both the dissolution of NAPL is a slow process when the solubility of NAPL is low and the diffusion of dissolved contaminant is also slow. The pump-and-treat method is effective in some cases by adding surfactants in the system to reduce the high capillary forces responsible for trapping. However, the introduction of more chemicals into the system causes secondary contamination since the surfactants themselves may be toxic and harmful. In all, there is a definite need for a new treatment technology without existing disadvantages of the current remediation approaches.

#### **2.4. The elastic wave stimulation technology**

The elastic wave stimulation method is a promising technique, although there is still a great deal of work needed to do before it can be reliably implemented in a field-scale.

Numerous investigators studied the enhancement effects of high frequency waves (ultrasound) on the transport of NAPL removal, which requires high intensity to be effective. This method works well at ranges up to about 20cm from the radiation source, but it is impractical for use in a field-scale where the target is usually more than 20cm apart from the acoustic actuator (Roberts *et al.*, 2001). Consequently several researchers have shifted to studies of low-frequency vibrations to enhance NAPL transport in porous media and have already performed some laboratory experiments. Reddi and Challa (1994) examined the effects of vibrating or shaking the studied system and concluded that the remediation was indeed enhanced by disturbing the pore structure. However, pore structure changes are

unlikely to occur in a field-scale. During the experiments, they investigated the effects of some factors such as vibration amplitude. No frequency effects were studied.

Beresnev and Johnson (1994) gave a comprehensive review of both methods and results in laboratory experiments and field case studies with elastic wave stimulation. Although many researchers studied the effects of earthquakes, which cause a kind of elastic wave, on oil production, the results are not desirable with some wells showing increased oil production while others show no change, or even decrease in productivity. Since the mechanisms behind these effects are unknown, it is impossible to predict the effects of elastic waves quantitatively in a given reservoir.

Moreover, in a more recent study by Roberts *et al.* (2001), it appeared that mechanical stress stimulation could enhance the transport of a trapped NAPL by applying an acoustic actuator to a water-saturated sand core sample at the frequencies ranging from 25 to 100 *Hz*. In the experiments, a small amount of commonly used industrial solvent, TCE (trichloroethylene), was added into water as a contaminant, and the results showed that TCE concentration in the effluent increased by as much as 20 times when vibration was applied to the sample. At the same time, they found that increasing the amplitude of the stimulation increased the concentration of TCE in the effluent. However, they stated that “the physical mechanisms responsible for the observed phenomenon are not fully understood. Further research is required before this promising new technology can be applied reliably to contaminated groundwater aquifers.”

In addition, Fontenot (2001) performed the study of low frequency pulsation effects on non-aqueous phase liquid movement and dissolution in porous media using a two dimensional micro-model. By examining the effects of low frequency flow pulsations on TCE removal, it was found that the lower the pulsation frequency, the more effective the removal of NAPL. Moreover, increasing the amplitude of pulsation was found to increase NAPL removal. In addition, the author stated that the combination of a nonionic surfactant with pulsation resulted in improved NAPL transport, with the same trends mentioned above.

However, a reasonable mechanism for ganglia transport enhancement under elastic wave was urged to be proposed and verified before the promising remediation technique could be applied in a field-scale extensively.

## 2.5. The capillary-physics mechanism

As it was mentioned before, several mobilization mechanisms were proposed to explain the enhancement mobilization of trapped NAPL under elastic wave stimulation. Among them, the simple capillary-physics mechanism presented by Beresnev *et al.* (2005) can explain all experimental observations and is therefore a leading candidate.

The primary reason for the entrapment of NAPL is capillary forces, which result from differences in the diameters of pore channels through which the NAPL is driven by external pressure gradient. As shown in Figure 2.1, assuming NAPL as a non-wetting phase, an extra capillary pressure is created on the internal side of the downstream meniscus as the NAPL enters the pore constriction. Because the radius of the left (upstream) meniscus  $R^{left}$  is greater than the radius of the right (downstream) meniscus  $R^{right}$ , an internal capillary pressure imbalance  $P_c^{right} - P_c^{left}$  is created, against the external pressure gradient. And the capillary pressure imbalance increases as the NAPL moves toward the narrowest part (center) of the constriction because of continuously increased deformation, and reaches the maximum when the NAPL ganglion arrives at the narrowest part and the downstream meniscus reaches its minimal radius. The imbalance increases as the ganglion moves into the constriction and the NAPL ganglion stops and is trapped when this imbalance equals the driving external pressure gradient  $\Delta P$  before the imbalance could reach the maximum value. To push the ganglion through, the external pressure gradient needs to exceed a certain “unplugging” threshold  $\Delta P_0$ .

Figure 2.2 presents the expected average flow rate as a function of external pressure gradient. The flow rate is zero (in the “no-flow” region) and the NAPL droplet will be trapped until the value of the current static pressure gradient  $\Delta P_s$  exceeds threshold  $\Delta P_0$ . After that, the flow starts to follow the normal Darcy law (in the “flow” region).

Thereafter, to mobilize the trapped fluid for the case when the static external pressure gradient  $\Delta P_s$  is lower than the unplugging threshold  $\Delta P_0$ , a longitudinal vibration of the wall, which is parallel to the pore axis, is applied to the system. The vibration of the wall induces an inertial force  $P_{osc}$  on the fluid with magnitude  $\rho_f a_0$  approximately, where  $\rho_f$  is the average density of the fluid and  $a_0$  is the acceleration amplitude of the vibration (Biot, 1956).

The instant total combined force on the fluid then becomes  $P_{osc} + \Delta P_s$ . A full cycle of the combined force and  $P_{osc}$  are shown in Figure 2.2 for a case where acceleration amplitude of vibration is sufficiently large enough that the total combined force ( $P_{osc} + \Delta P_s$ ) is greater than the unplugging threshold ( $\Delta P_0$ ) in part of a vibration cycle (usually in positive part). The trapped ganglion will move forward when the total combined force exceeds the threshold  $\Delta P_0$  in part of the positive half-cycle of vibration, and remains trapped as long as the total force is equal or less than the threshold in the rest cycle of vibration (Note that the total forcing is bigger than zero even in the negative half-cycle of vibration), which leads to a “nudging” motion of the trapped ganglion through the constriction. Finally the ganglion will be mobilized and enter into the downstream after a series of vibration cycles.

Two predictions based on this capillary-physics mechanism can be deduced. First of all, the enhancement effect will be strengthened as the acceleration amplitude of vibrations increases under fixed vibration frequency because increasing acceleration amplitude will increase the magnitude of  $P_{osc}$ , hence the total force. But the acceleration amplitude effect will level off as the acceleration amplitude continues to increase such that the total force will become negative in part of the negative half-cycle of vibration, hence the system will follow the usual Darcy flow. Secondly, the flow enhancement effect will be inversely proportional to the vibration frequency under fixed acceleration amplitude because only in part of the positive half-cycle of vibration when the total force is greater than the threshold a “nudging” motion of the ganglion can occur and the longer the helpful part over one period the more displacement of the ganglion. Moreover, there exists a threshold of frequency above which no flow enhancement effect occurs since the ganglion response time becomes larger compared with the vibration period. The response time (also called the viscous diffusion time, defined as  $\tau = \rho_f \frac{r^2}{\mu}$ , where  $\rho_f$  is the ganglion density,  $\mu$  is the dynamic viscosity, and  $r$  is the radius of the pore channel) is the characteristic time scale over which the fluid responds to a step force (Johnson, 1998).

This kind of minimum-amplitude and maximum-frequency threshold dependency is shown in Figure 2.3.

## 2.6. References

- Baldwin, C.A., and Gladden, L.F., (1996). NMR Imaging of nonaqueous-phase liquid dissolution in a porous medium. *AIChE Journal*, 42(5), 1341-1349.
- Beresnev, I.A., and Johnson, P.A., (1994). Elastic-wave stimulation of oil production: A review of methods and results. *Geophysics*, 59(6), 1000-1017.
- Beresnev, I.A., Vigil, R.D., Li, W., Pennington, W.D., Turpening, R.M., Iassonov, P.P., and Ewing, R.P., (2005). Elastic waves push organic fluids from reservoir rock. *Geophysical Research Letter*. 32(13), L13303, doi:10.1029/2005GL023123.
- Biot, M.A., (1956). Theory of propagation of elastic waves in a fluid-saturated porous solid. II. Higher frequency range, *Journal of Acoustical Society of America*, 28, 179-191.
- Chen, J.D., and Wada, N., (1986). A new technique for visualizing the distribution of oil, water, and quartz grains in a transparent, three-dimensional, porous medium. P.O. Box 833836, Richardson, TX 75083-3836, *Society of Petroleum Engineers*, 205-208.
- Conrad, S.H., Wilson, J.L., Mason, W.R., and Peplinski, W.J., (1992). Visualization of residual organic liquid trapped in aquifers. *Water Resources Research*, 28(2), 467-478.
- Fontenot, M.M., (2001). Study of transport and dissolution of a nonaqueous phase liquid in porous media: Effects of low-frequency pulsations and surfactants. PhD dissertation, Iowa State University.
- Fontenot, M.M., and Vigil, R.D., (2002). Pore scale study of non-aqueous phase liquid dissolution in porous media using planar laser-induced fluorescence, *Journal of Colloid and Interface Science*, 247(2), 481-489.
- Geller, J.T., and Hunt, J.R., (1993). Mass transfer from nonaqueous phase organic liquids in water-saturated porous media. *Water Resources Research*, 29(4), 833-845.
- Graham, D.R., and Higdon, J. J. L., (2000). Oscillatory flow of droplets in capillary tubes. Part 2. Constricted tubes. *Journal of Fluid Mechanics*, 425, 55-77.
- Hunt, J.R., Sitar, N., and Udell, K.S., (1988). Nonaqueous phase liquid transport and cleanup. 1. Analysis of mechanisms. *Water Resources Research*, 24(8), 1247-1258.

- Imhoff, P.T., Jaffé, P.R., and Pinder, G.F., (1994). An experimental study of complete dissolution of a nonaqueous phase liquid in saturated porous media. *Water Resources Research*, 30(2), 307-320.
- Imhoff, P.T., Thyrum, G.P., and Miller, C.T., (1996). Dissolution fingering during the solubilization of nonaqueous phase liquids in saturated porous media. *Water Resources Research*, 32(7), 1929-1942.
- Iassonov, P.P., (2001). Enhancement of fluid flow in porous media by application of low-frequency sonic vibrations, MS thesis, Iowa State University.
- Iassonov, P.P., and Beresnev, I.A., (2003). A model for enhanced fluid percolation in porous media by application of low-frequency elastic waves. *Journal of Geophysics Research*, B 108(3), 2138.
- Johnson, R.W., (1998). *The Handbook of Fluid Dynamics*, CRC Press, pp.9-11.
- Krupka, K.M., and Martin W.J., (2001). Subsurface contaminant focus area: Monitored natural attenuation (MNA)-programmatic, technical, and regulatory issues, PNNL (Pacific Northwest National Laboratory) paper.
- Lowry, M.I., and Miller, C.T., (1995). Pore-scale modelling of nonwetting-phase residual in porous media. *Water Resources Research*, 31(3), 455-473.
- Miller, C.T., Poirier-McNeill, M.M., and Mayer, A.S., (1990). Dissolution of trapped nonaqueous phase liquids: Mass transfer characteristics. *Water Resources Research*, 26(11), 2783-2796.
- Montemagno, C.D., and Gray, W.G., (1995). Photoluminescent volumetric imaging: A technique for the exploration of multiphase flow and transport in porous media. *Geophysical Research Letters*, 22(4), 425-428.
- Morrow, N. R.; and Songkran, B., (1981). Effect of viscous and buoyancy forces on nonwetting phase trapping in porous media. *Surface Phenomena in Enhanced Oil Recovery*, Ed. D.O. Shah, Plenum Publishing Corp., 387-411.
- Pankow, J.F., and Cherry, J.A., (1996). *Dense chlorinated solvents and other DNAPLs in groundwater*, Portland, Oregon, Waterloo Press.

- Powers, S.E., Abriola, L.M., and Weber, W.J. Jr., (1992). An experimental investigation of nonaqueous phase liquid dissolution in saturated subsurface systems: Steady state mass transfer rates. *Water Resources Research*, 28(10), 2691-2705.
- Powers, S.E., Abriola, L.M., and Weber, W.J. Jr., (1994). An experimental investigation of nonaqueous phase liquid dissolution in saturated subsurface systems: Transient mass transfer rates. *Water Resources Research*, 30(2), 321-332.
- Rashidi, M., and Dickenson, E., (1996). Small scale flow processes in aqueous heterogeneous porous media. FED, 239, 1996, ASME Fluids Engineering Division Conference, volume 4, 409-414, San Diego, CA.
- Reddi, L.N., and Challa, S., (1994). Vibratory mobilization of immiscible liquid ganglia in sands. *Journal of Environmental Engineering* (New York, N.Y.), 120(5), 1170-1190.
- Reddy K.R., and Saichek, R.E., (2003). Effect of soil type on electrokinetic removal of phenanthrene using surfactants and cosolvents. *Journal of Environmental Engineering, ASCE* 129(4), 336-346.
- Roberts, P.M., Sharma A., Uddameri, V., Monagle, M., Dale, D.E., and Steck, L.K., (2001). Enhanced DNAPL transport in a sand core during dynamic stress stimulation. *Environmental Engineering Science*, 18(2), 67-79.
- Roberts, P.M., Esipov, I.B., and Majer, E.L., (2003). Elastic wave stimulation of oil reservoirs: Promising EOR technology? *The Leading Edge*, 22(5), 448-453.
- Weiss, G., (1986). *Hazardous Chemicals Data Book*, 2<sup>nd</sup> edition, Noyes Data Corporation: Park Ridge, N.J., 1986, pp.974.
- Wilson, J.L., Conrad, S.H., Mason, W.R., Peplinski, W., and Hagan, E., (1990). Laboratory investigation of residual liquid organics from spills, leaks, and the disposal of hazardous wastes in groundwater. (Order No. PB90-235797). pp.285.

## 2.7. Figure captions

Figure 2.1. Schematic of droplet flow through a horizontal straight channel with a constriction under a static pressure gradient  $\Delta P$ . The radii of the trailing and leading droplet meniscii are labeled as  $R^{left}$  and  $R^{right}$ , respectively (as shown,  $R^{left} > R^{right}$ ).

The corresponding internal capillary pressures are given by  $P_c^{left}$  and  $P_c^{right}$ .

According to the general form of the Laplace equation for non-spherical menisci,

$P_c^{left} = \sigma / R^{left}$ ,  $P_c^{right} = \sigma / R^{right}$  and therefore  $P_c^{right} > P_c^{left}$ , where  $\sigma$  is the interfacial

tension between the two phases. The ganglion is trapped only when

$P_c^{right} - P_c^{left} = \Delta P$  is satisfied.

Figure 2.2. Average flow rate as a function of the combined forces of static external pressure gradient and vibratory forces, explaining the capillary-physics mobilization mechanism.

Figure 2.3. Average flow rate as a function of the amplitude of vibratory forcing, showing the existence of both minimum-amplitude and maximum-frequency thresholds.

Frequency is the parameter of the curves.

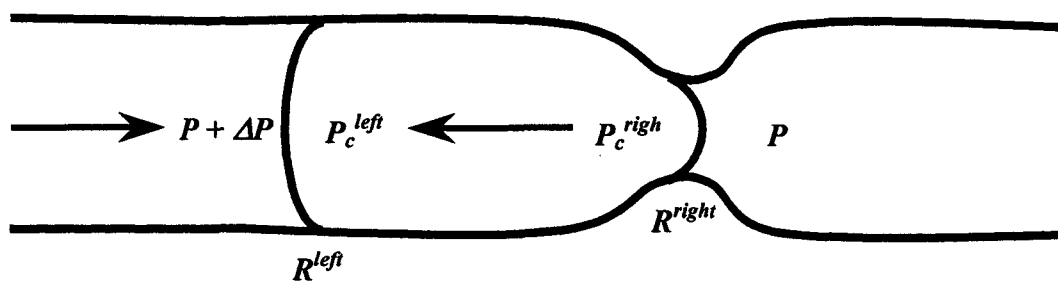


Figure 2.1

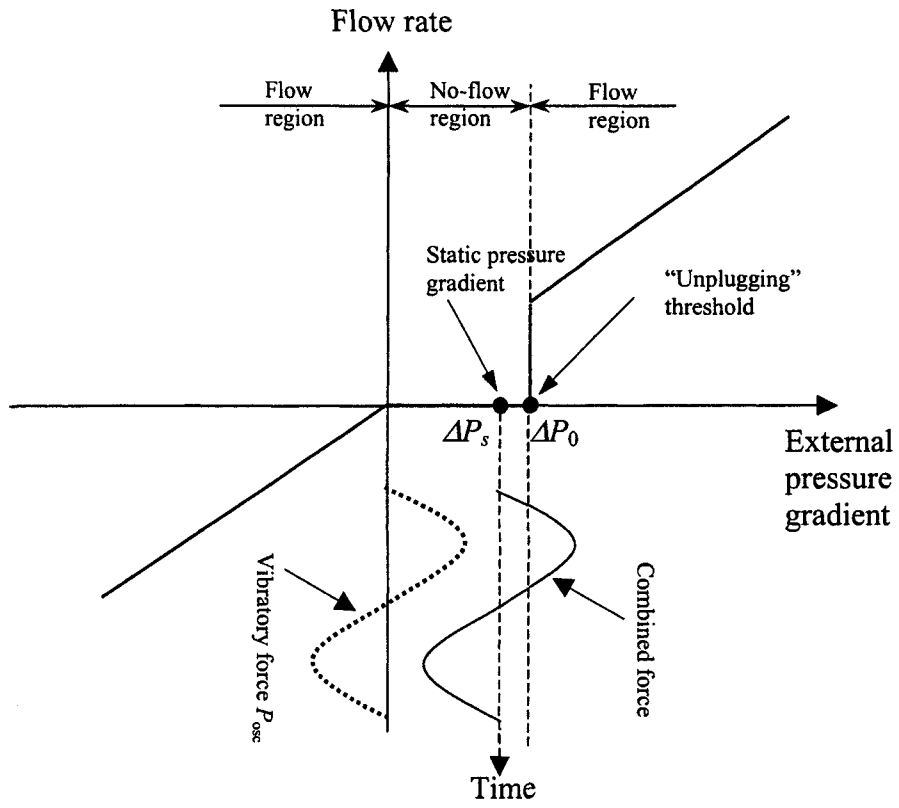


Figure 2.2

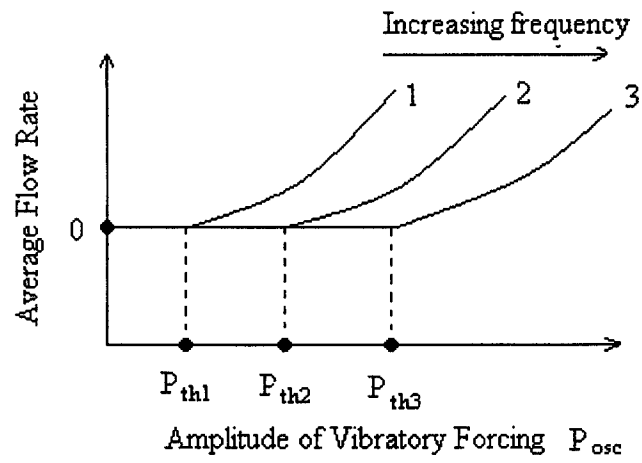


Figure 2.3

## CHAPTER 3. REVIEW OF TWO-PHASE FLOW NUMERICAL SIMULATIONS

### 3.1. Introduction to two-phase flow

Multiple-phase flow is a quite common phenomenon in nature, such as the formation and movement of clouds in air, dust in air, sediment in water, and in technology, especially in the field of engineering including chemical engineering, petroleum engineering and environmental engineering, etc. Examples include trickle bed reactors, secondary oil recovery, and contamination and remediation of underground water by non-aqueous phase liquids. Due to the numerous applications involving multiple-phase flow and to delve the mechanisms behind the phenomena, many investigators have conducted experimental studies and numerical studies as well.

Multiple-phase flow can be very complex due to complicated combination of phases, such as gas-solid-liquid, liquid-liquid-gas-solid, etc., and flow structures like film flow, plug flow, bubbly flow, particulate flow or complex combinations of the flows. But two-phase flow is the simplest case of multi-phase flow, which in general is the combination of any two from gas, liquid and solid phases. However, it is still very complicated from the perspective of flow structure and phase interaction, such as mass transfer, reaction, mixing, energy transfer, and interfacial action. Hence it is very difficult to accurately model even dispersed two-phase flow. Two-phase flow for immiscible phases, especially the immiscible liquid-liquid case, is again the simplest case in two-phase flow where no mass transfer is assumed between the two phases. The assumption is reasonable when the solubility of one phase is negligible in the other phase, such as the two-phase flow system of gasoline and water, the system of non-aqueous phase liquid and water, etc.

Some classification methods are made for two-phase flow problems. Ishii (1975) grouped two-phase flow into four categories, flow of gas-liquid, gas-solid, liquid-solid, and immiscible liquid-liquid, depending on the mixtures of phases in the flow. Notice that immiscible liquid-liquid flow is actually a single phase flow with two components rather than a two-phase flow. However, it is usually considered to be a two-phase mixture hence is a

kind of two-phase flow. At the same time, Ishii (1975) divided two-phase flow into three classes: separated flows (such as film flow, annular flow), transitional or mixed flows (such as plug or slug flow, bubbly annular flow, droplet annular flow), and dispersed flows (such as bubbly flow, droplet flow, particulate flow), according to the interfacial structure and the flow structure. Moreover, other classifications of two-phase flow were made for a specific combination of phases and flow structure. For example, Kunii and Levenspiel (1991) showed a specific classification for fluidization problems where solid particles flow in a gas phase or a liquid phase.

There are numerous models that can be used to simulate a two-phase flow. Based on the classifications, models for two-phase flow can be chosen according to some factors, such as flow structure, flow phases, what kind of specific applications, etc., among which, the flow structure is the most important factor. For example, in the classification of Ishii (1975), modeling separated and dispersed flows are very different since the flow structure is significantly different between the two classes. The interface between the two phases is more important and significant in a separated flow than in a dispersed flow because in a dispersed flow it is hard and impossible to calculate the interface between the two phases due to expensive computation (although the interface is also important sometimes). Hence, in general, in a dispersed flow, some kind of average quantities are calculated rather than the exact interfacial structure and position, which is totally different in a separated flow where the exact structure and position of interface is computed. The totally different flow structure results in different models that have different tasks. In other words, in a separated flow, the simulation models are needed to track the exact interface between the two phases, however, in a dispersed flow, the simulation models are necessary to study the bulk flow rather than to obtain the exact position of the interface.

### **3.2. Modeling separated flow**

In a separated flow modeling, one can possibly setup flow governing equations for each single phase and a moving boundary balance equation between the two phases if the structure of the interface is not too complex. The material in each phase is considered to be a

continuum and is occupying same space. Therefore, a new “material”, mixture of these two interacting materials with certain proportions, is introduced. As for the interface tracking methods, the usual methods are the marker and cell method (Harlow and Welch, 1965), the front-tracking method (Unverdi and Tryggvason, 1992), the volume-tracking method (Noh and Woodward, 1976; Hirt and Nichols, 1981; Youngs, 1982; Rudman, 1997), and the level set method, among which, the last two methods are extensively being used by researchers recently.

### **3.2.1. The marker and cell method**

The well-known marker and cell (MAC) method is one of the earliest techniques for simulating free surface flow. In the MAC method, a set of discrete Lagrangian marker particles is moving with the fluid and is used to indicate fluid configuration (Harlow and Welch, 1965). Although the MAC method can deal with arbitrary free surface two-phase flow theoretically, there are difficulties in particle re-presentation of the fluid configuration (for example, it can result in false regions of void due to a finite number of particles used) and expensive computation if a large number of markers are used.

### **3.2.2. The front-tracking method**

In the front-tracking method, a sharp Lagrangian interface or a front (represented by a set of connected line segments) is used to separate the two phases. In Unverdi and Tryggvason (1992), the flow field is discretized by a finite difference method on a stationary Eulerian grid, and the interface is explicitly represented by a separate and unstructured grid, which moves through the stationary grid and is re-meshed as the computations proceed and the interface deforms continuously. However, expensive computation is required because the method needs re-mesh and re-construct the moving grid and the interface as the calculations proceed.

### **3.2.3. The volume-tracking method**

In the volume-tracking method, a fractional volume function is defined to identify the fraction of a mesh cell that is filled with one of the fluids. The interface is constructed from

the fractional volume function (also called the color function) and it is updated after the fractional volume function is updated. A number of advection techniques are used to maintain interfaces as sharp as possible, such as the simplified line interface calculation (SLIC) method (Noh and Woodward, 1976), the volume of fluid (VOF) method of Hirt and Nichols (Hirt and Nichols, 1981), the volume of fluid method of Youngs (Youngs, 1982), and the flux-corrected transport (FCT)-VOF method (Rudman, 1997), are used to solve the advection equation of the fractional volume function.

The SLIC method of Noh and Woodward uses a direction-split algorithm where the interface in a mesh cell is reconstructed using a straight line parallel to one of the co-ordinate directions. In each direction sweep, only cell neighbors in the sweep direction are used to reconstruct the interface (Noh and Woodward, 1976). Also, the original VOF method of Hirt and Nichols uses an approximate interface reconstruction parallel to one of the co-ordinate directions, but all the cell neighbors are used to estimate the surface normal and the interface is determined parallel to which coordinate direction according to the relative magnitudes of the surface normal components (Hirt and Nichols, 1981). The VOF of Youngs (Youngs, 1982) uses a more accurate interface reconstruction algorithm than the above two methods. The interface direction is estimated first. Then a line segment with the estimated orientation, which cuts the cell in such a way that the fractional fluid volume is known, approximates the interface within the cell. After that, new fluxes will be updated based on the new geometry and velocity distribution. The FCT-VOF (Rudman, 1997) uses a suitable combination of high order (non-monotonic) upwind and downwind schemes, rather than a simple combination of first order (monotonic) upwind and downwind fluxes in the donor-acceptor scheme of VOF of Hirt and Nichols, to eliminate both the diffusiveness of the upwind scheme and the instability of the downwind scheme. Although the FCT-VOF is more accurate than both the SLIC method of Noh and Woodward and the original VOF method of Hirt and Nichols, it is inferior to the method originally proposed by Youngs (1982). But it is unique because an approximate interface reconstruction is not required in order to keep sharp interface, and it is readily extended to three dimensions and curvilinear co-ordinate systems.

The VOF method is conservative and easy to implement, and can deal with configuration changes of the interface comparatively accurately. However, a higher order of

accuracy is hard to achieve because the fractional volume function is not continuous. Also, it is less accurate to calculate properties of the interface such as norm and curvature than the level set method. Moreover, it is usually computationally extensive.

#### 3.2.4. The level set method

The level set method was firstly introduced by Osher and Sethian (1988). Lately Osher and Fedkiw (2003) gave a general description of the approach. In the level set method, a continuous signed function (called the level set function)  $\phi$  is introduced as an auxiliary function to represent the shortest distance of the Eulerian grid to the interface. Hence, the zero level set of  $\phi$  means the interface. Since the level set function can advect with the related flow field, the zero level set can also be updated with the flow to follow the exact position of the interface.

To account for the interfacial tension forcing on the interface and model the interfacial tension effect, the interface is considered to be an interfacial region with uniform width in practice rather than a surface only. Hence, the interfacial condition can be incorporated into the momentum equation as an additional force term (Brackbill, *et al.*, 1992). Moreover, it makes the surface force model continuous and a two-phase flow can be treated as a single-phase flow but with varied fluid properties through the interfacial region.

A typical example of the level set approach applied for incompressible two-phase flow is given by Sussman *et al.* (1994), in which a motion of air bubbles in water and falling water drops in air were calculated and the level set approach was extended to the case where large density and viscosity ratios as well as surface tension coexist. Sussman *et al.* (1998) is another example to compute a two-phase flow using the level set method.

The biggest advantage of the level set approach is that it is easy to reconstruct the interface from the level set function and to obtain a higher accuracy solution due to the continuity of the level set function. However, in general, the level set approach is mass non-conservative. In other words, loss or gain of mass might during the calculations. To avoid the problem caused by the level set method alone, Sussman and Puckett (2000) presented a coupled level set and volume-of-fluid (CLSVOF) method, in which some of the advantages of the VOF method and the level set method were combined together and hence the coupled

method was generally better than either method alone. Using the coupled method it is possible to have a solution with good mass conservation (coming from VOF method) and to adequately approximate properties of the interface such as the norm and curvature (based on the level set function). However, some kind of simplicity of the original level set method has to be sacrificed in the coupled method. Another way to improve the performance of the original level set method is to use a special level set function, such as Olsson and Kreiss (2005). They used a smeared out Heaviside function (zero in one fluid and one in the other for a two-phase flow), other than the standard Heaviside level set function, to obtain a second order accuracy solution and very good mass conservation.

### **3.3. Modeling dispersed flow**

It is impossible to compute dispersed flows using an interface tracking method because of the high complexity and plenty of interfaces between the phases. So, other strategies are needed to model dispersed flows. Two extensively used approaches, the Lagrangian-Eulerian method and the Eulerian-Eulerian method, are briefly discussed below for completeness.

#### **3.3.1. The Lagrangian-Eulerian approach**

The Lagrangian-Eulerian approach, usually used for a particle-fluid system with only a few particles, uses the similar concept in the MAC method mentioned above. Particles are introduced and moving in the continuous phase that is computed in an Eulerian reference frame. Crowe *et al.* (1998) described three different strategies accounting for the influence between the particles and the fluid: the one-way coupling (only the influence of the neighborhood fluid to the particles is considered), the two way-coupling (the interactive influence between the particles and the surrounding fluid is considered, i.e., the influence of the particles to the fluid and the fluid to particles are both incorporated), and the four-way coupling (besides the influence between the particles and the surrounding fluid, the influence between particles are also considered). A typical implementation was shown by Patankar and Joseph (2001), in which they used an Eulerian-Lagrangian scheme to simulate particulate

flows. In the scheme, the continuity and momentum equations for the fluid phase were solved on an Eulerian grid and the particle motion was assumed to be governed by Newton's law thus following the Lagrangian approach. Also, the momentum equations for the fluid and the particles were coupled and solved.

### 3.3.2. The Eulerian-Eulerian approach

The Eulerian-Eulerian approach, also called the two-fluid model, is widely used. It treats each phase as a continuum, and both phases (even though they are often not different phases of the same material) in the mixture interpenetrate each other and occupy the same space. So mass, momentum, and energy balance equations for both phases and jump equations between phases must be solved together. But suitable averaging method must be used since the exact information for both phases is hard to obtain. Although averaging usually causes information loss, fortunately it makes little difference in the solutions for engineering problems. Among the averaging methods, the ensemble averaging method (for more details see Drew, 1983 and Drew and Passman, 1999), which can describe the values of mechanical variables, and the local volume averaging method (for more details see Anderson and Jackson, 1967, and Jackson, 2000), which uses regional averaging of mechanical properties instead of point values, are two commonly used methods.

However, the Eulerian-Eulerian approach have more unknown variables than equations. Therefore, closure laws, usually coming from empirical assumptions (also called the non-granular model, for further information see example: Enwald *et al.* 1996) or kinetic theory of gases (also called the granular model, for further information see examples: Jenkins and Savage, 1983; Lun *et al.*, 1984; Gidaspow, 1994, and Goldschmidt *et al.*, 2001), are necessary to make the problem solvable. Another classification of closure laws was described in Enwald *et al.* (1996). They divided the closure laws into three types: constitutive laws (relating physical properties using axioms and experimental data), transfer laws (using empirical equations to describe the interaction between the phases occurring at the interface), and topological laws (describing the spatial distribution of a flow variables, e.g., concentration or velocity distribution of one phase).

In the Eulerian-Eulerian approach, a coarser mesh and longer time step can be used rather than the finer mesh (less than the smallest length scale) and shorter time step (shorter than the time scale of the fastest fluctuation) needed in the Lagrangian-Eulerian approach (note that the stability requirements must be satisfied for both approaches), hence computational time will be reduced dramatically.

### **3.4. Modeling packages**

#### **3.4.1. FLUENT**

FLUENT is the world's largest provider of computational fluid dynamics software and is a typical choice for simulation of multi-phase flow, including two phase flow. FLUENT has its defined flow regimes, on which the model is chosen. FLUENT provides two approaches for the numerical calculation of multiphase flows: The Euler-Lagrange approach and the Euler-Euler approach. The Lagrangian discrete model in FLUENT is based on the Euler-Lagrange approach, and appropriate for the case where the dispersed phase occupies a low volume fraction, such as spray dryers, coal and liquid fuel combustion. On the other hand, FLUENT provides three different Euler-Euler multiphase models: the Volume of Fluid model, the Mixture model, and the Eulerian model. The Volume of Fluid model uses a surface tracking technique based on a fixed Eulerian mesh and is appropriate for the case of two or more immiscible fluids. This is the model we are going to use in the numerical studies shown in chapters 5 and 6. The mixture model is designed for two or more phases (fluid or particulate) where the phases are treated as interpenetrating continua. The Eulerian model is the most complex of the multiphase models in FLUENT.

As for the Volume of Fluid model, a variable called the volume fraction for the phase is introduced in the computational cell for each additional phase you add, and the volume fractions of all the phases must sum to unity in each location. Based on the known volume fraction, all properties and variables are obtained by volume averaging. The set of equations for the later numerical studies, including volume fraction equation, momentum equations, and energy equation, are listed in chapter 5. In the method, convection and diffusion fluxes through the control volume faces are required to be balanced with source terms in the control

volume, and FLUENT provides four schemes for the calculation of face fluxes: implicit, Euler-explicit, donor-acceptor, and geo-reconstruct, among which the geo-reconstruct scheme is the most accurate by using a special interpolation treatment to the cells near the interface. Moreover, the Volume of Fluid method can also include the effects of surface tension along the interface between each pair of phases by specifying a surface tension coefficient or set of them. Furthermore, it can account for wall adhesion by using FLUENT defined contact angle between the phases and walls. All of the above advantages make the Volume of Fluid method a good choice to do numerical experiments for vibratory stimulation of multiphase flow through capillary tubes.

In addition, FLUENT has some other special models, such as model for solidification and melting using an enthalpy-porosity formulation besides the models for multiphase flow described above. More descriptions and details about the difference, choices, and mechanisms among the models see the manual of FLUENT (FLUENT, 2003).

### **3.4.2. FEMLAB**

FEMLAB is the first engineering tool that performs equation-based multi-physics modeling in an interactive environment. It is possible to model a multi-physics problem by combining any number of specialized physics application modes. Since the finite element method is adopted by FEMLAB, the simulation results are more accurate for interface tracking and FEMLAB requires less computing time than FLUENT although greater memory is consumed (Hanke, 2004). Moreover, FEMLAB exhibits a performance that rivals its competitors among the three leading packages-FLUENT, ANSYS, and FEMLAB.

The continuum - constitutive equation approach, which is based on a diffusive flux multiphase model, and the level set approach are two common simulation approaches in FEMLAB involving multiphase flow. The level set method of multiphase flow in FEMLAB eliminates all the complexities required for free surface tracking and makes the geometric properties of the interface easily determined. The level set function is continuous and the related partial differential equation can be handled with common numerical methods. Both fixed and adaptive grids may be used for steady-state study, and it is easy to extend to an

arbitrary number of dimensions and to do a natural treatment of breakup and merging of the interface.

Although there are some successful simulation cases using the level set approach to model the interface between two fluids, such as the case of a rising bubble, so far the level set approach is not fully available and supported by FEMLAB to simulate a case like ours, vibratory stimulation of two immiscible fluids flowing through porous media, especially a constricted channel or a convergence – divergence network.

### 3.4.3. Self-coding

Although the commercial CFD packages are available to solve multiphase flow problems, they have disadvantages such as the lack of flexibility, specified optimization, and computational efficiency. For example, the finite element meshing method isn't adopted by FLUENT, and adaptive meshing and time-dependent algorithms can't be used simultaneously in FEMLAB. However, self-coding, based on governing equations, boundary conditions, initial conditions, grid generation algorithm, and solver schemes for the specific case, is always available and efficient though it is often difficult to construct.

A typically successful case (close to our study) by self-coding was done by Graham and Higdon (2000a, 2000b) concerning the oscillatory flow of droplets in capillary straight and constricted tubes. In their papers, firstly a special technique called elliptic grid generation was adopted to efficiently track the free interface and maintain accuracy when the physical domain was mapped to a simplified one. Hence adaptive meshing could be used throughout the calculation. Then the Galerkin finite element method was used to simultaneously solve the governing equations (continuity and momentum equations) and the elliptic grid generation equations as well as boundary and initial conditions. For steady-state study, the system of nonlinear algebraic equations was solved iteratively with Newton's method and UMFPACK, a code that implements a frontal method. For unsteady time dependent flow, a predictor-corrector, an explicit Adams-Bashforth prediction first then an implicit trapezoidal rule correction, was adopted. The above algorithm was shown to be accurate enough based on convergence tests compared with previously published results.

### 3.5. Motivation of the research

While many researchers are still working on the study of acoustic stimulation to enhance NAPL transport, unfortunately very little experimental information concerning the mechanisms behind the process is available. Furthermore current experiments are not sufficiently realistic to predict the effects of low-frequency irradiation on a real field-scale system.

The purpose of the research is to examine the effects of low frequency (lower than 50 Hz) vibration, a kind of acoustic stimulation, on NAPL remediation by using a two-dimensional physical micro-model and computational fluid dynamics packages. We will inspect the effects of frequency and acceleration amplitude of vibration, and some other factors as well, to validate the potential capillary-physics mechanism and hence clarify some details, then provide a base for further study of NAPL in porous media and lay a solid foundation for improving the mobilization of capillary-trapped ganglion. Moreover, preliminary study will be carried out about droplet breakup driven by interfacial tension in capillary tubes.

### 3.6. References

- Anderson, T.B., and Jackson, R., (1967). A fluid mechanical description of fluidized beds: equations of motion. *Industrial and Engineering Chemistry Fundamentals*, 6(4), 527-539.
- Brackbill, J.U., Kothe, D.B., and Zemach, C., (1992). A continuum method for modeling surface tension. *Journal of Computational Physics*, 100(2), 335-354.
- Crowe C.T., Sommerfeld, M., and Tsuji, Y., (1998). *Multiphase flows with droplets and particles*, CRC Press, Boca Raton, Fla.
- Drew D.A., (1983). Mathematical modeling of two-phase flow. *Annual Review of Fluid Mechanics*, 15, 261-291.
- Drew D.A. and Passman S.L., (1999). *Theory of multicomponent fluids*, New York: Springer-Verlag.

- Enwald, H., Peirano, E., and Almstedt, A.-E., (1996). Eulerian two-phase flow theory applied to fluidization. *International Journal of Multiphase Flow*, 22 (Supplement 1), 21-66.
- FLUENT Inc., (2003). FLUENT 6.1 User's Guide.
- Gidaspow, D., (1994). Multiphase flow and fluidization: continuum and kinetic theory descriptions with applications, Academic Press, Boston.
- Goldschmidt, M.J.V., Kuipers, J.A.M., and Van Swaaij, W.P.M., (2001). Hydrodynamic modeling of dense gas-fluidised beds using the kinetic theory of granular flow: effect of coefficient of restitution on bed dynamics. *Chemical Engineering Science*, 56(2), 571-578.
- Graham, D.R., and Higdon, J.J.L., (2000a). Oscillatory flow of droplets in capillary tubes. Part 1. Straight tubes. *Journal of Fluid Mechanics*, 425, 31-53.
- Graham, D.R., and Higdon, J.J.L., (2000b). Oscillatory flow of droplets in capillary tubes. Part 2. Constricted tubes. *Journal of Fluid Mechanics*, 425, 55-77.
- Hanke, M., (2004). Benchmarking FEMLAB 3.0a: Laminar Flows in 2D.  
<http://www.psci.kth.se/Activities/Reports/Results/2004/benchm.pdf>.
- Harlow F.H. and Welch J.E., (1965). Numerical calculation of time-dependent viscous incompressible flow of fluid with free surface. *Physics of fluids*, 8(12), 2182-2189.
- Hirt, C.W. and Nichols, B.D., (1981). Volume of fluid (VOF) method for the dynamics of free boundaries. *Journal of computational physics*, 39(1), 201-225.
- Ishii M., (1975). Thermo-fluid dynamic theory of two phase flow. Eyrolles, Paris.
- Jackson, R., (2000). The dynamics of fluidized particles, Cambridge University Press, New York.
- Jenkins, J.T., and Savage, S.B., (1983). A theory for the rapid flow of identical, smooth, nearly elastic, spherical-particles. *Journal of Fluid Mechanics*, 130, 187-201.
- Kunii D. and Levenspiel O., (1991). Fluidization Engineering, 2<sup>nd</sup> edition, Boston: Butterworth-Heinemann.
- Lun, C.K.K., Savage, S.B., Jeffrey, D.J., and Chepuruiy, N., (1984). Kinetic theories for granular flow: inelastic particles in Couette flow and slightly inelastic particles in a general flow field. *Journal of Fluid Mechanics*, 140, 223-256.

- Noh, W.F. and Woodward, P., (1976). SLIC (Simple line interface calculation), in A.I. van Dooren and P.J. Zandbergen (editors), *Lecture notes in physics*, 59, 330-340.
- Olsson, E. and Kreiss, G., (2005). A conservative level set method for two phase flow. *the Journal of computational physics*, in press.
- Osher S. and Fedkiw R., (2003), *Level set methods and dynamic implicit surfaces*, Springer-Verlag, New York.
- Osher S. and Sethian J.A., (1988). Fronts propagating with curvature-dependent speed: Algorithms based on Hamilton-Jacobi formulations. *Journal of computational physics*, 79(1), 12-49.
- Patankar, N.A., and Joseph, D.D., (2001). Modeling and numerical simulation of particulate flows by the Eulerian-Lagrangian approach. *International Journal of Multiphase Flow*, 27(10): 1659-1684.
- Rudman M., (1997). Volume-tracking methods for interfacial flow calculations. *International journal for numerical methods in fluids*, 24(7), 671-691.
- Sussman, M., Smereka, P. and Osher, S., (1994). A level set approach for computing solutions to incompressible two-phase flow. *Journal of computational physics*, 114(1), 146-159.
- Sussman, M., Fatemi, E., Smereka, P., and Osher, S., (1998). An improved level set method for incompressible two-phase flows. *Computers and Fluids*, 27(5-6), 663-680.
- Sussman, M. and Puckett, E.G., (2000). A coupled level set and volume-of-fluid method for computing 3D and axisymmetric incompressible two-phase flows. *Journal of computational physics*, 162(2), 301-337.
- Unverdi S.O., and Tryggvason G., (1992). A front-tracking method for viscous, incompressible, multi-fluid flows. *Journal of computational physics*, 100(1), 25-37.
- Youngs, D.L., (1982). Time-dependent multi-material flow with large fluid distortion, in K.W. Morton and M.J. Baines (editors), *Numerical methods for fluid dynamics*, Academic Press, New York, 273-285.

## **CHAPTER 4. VIBRATION-INDUCED MOBILIZATION OF TRAPPED OIL GANGLIA IN POROUS MEDIA: EXPERIMENTAL VALIDATION OF A CAPILLARY- PHYSICS MECHANISM**

Wenqing Li, R. Dennis Vigil, Igor A. Beresnev, Pavel Iassonov, Robert Ewing

Published in *Journal of Colloid and Interface Science*, 289 (2005), 193

### **Abstract**

The development of methods for mobilizing residual organic liquids trapped in porous media is becoming increasingly important as world demand for oil increases and because of the need to remediate aquifers degraded by slow-dissolving organic contaminants. Low-frequency elastic wave stimulation is one such technique, but until recently the lack of a mechanistic understanding of the effects of vibration on mobilization of oil ganglia has prevented the method from being applied predictably in the field. Recently, a simple capillary physics mechanism has been developed to explain vibration-induced mobilization of trapped non-wetting organic phase in porous media. Specific predictions that follow from this hypothesized mechanism are that vibrations will be most effective in mobilizing trapped oil when the acceleration amplitude is within an optimal range of values (that depend on the magnitudes of the capillary forces trapping the ganglia and the imposed static pressure gradients) and for sufficiently low vibration frequencies. In this paper we describe two-dimensional glass micromodel experiments that support these predictions.

### **Keywords**

Elastic wave stimulation, multiphase flow, porous media, acoustic stimulation, enhanced oil recovery, non-aqueous phase liquids

#### 4.1. Introduction

Multiphase flow in porous media is a complicated and incompletely understood problem with important practical applications to enhanced oil recovery, environmental remediation, and chemical reaction engineering. A common feature of these systems is the capillary entrapment of dispersed phase ganglia in small pores. For aqueous-organic liquid-liquid systems, several strategies for mobilizing residual oil in porous media have been proposed, including using water flooding (U.S. EPA., 1990), adding surfactants to lower interfacial surface tension (Oostrom *et al.*, 1999; Fountain, *et al.*, 1991; Pennell, *et al.*, 1994), increasing oil dissolution with cosolvents (Jawitz *et al.*, 2003; Reddy, *et al.*, 2003), using electro-osmosis (Reddy *et al.*, 2003; Iyer, 2001), and irradiating the medium with elastic waves (Beresnev and Johnson, 1994; Reddi and Challa, 1994; Roberts *et al.*, 2003). Several investigators have studied the use of ultrasonic waves to enhance the transport of a trapped oil phase in water, but this method requires high intensity irradiation to be effective, and even then it typically works well only for ranges less than a meter from the acoustic actuator, thereby rendering it impractical for use on the field scale (Roberts *et al.*, 2001).

Because of the limitations of ultrasonic irradiation, interest in elastic wave stimulation (EWS) has become focused on low frequency irradiation, which does not suffer from attenuation over short length scales. Beresnev and Johnson (1994) have provided a comprehensive review of methods and results for both laboratory experiments and field case studies using EWS. However, despite the existence of some early studies and anecdotal evidence, such as changes in oil field productivity during earthquakes, well-controlled experiments that quantitatively demonstrate the efficacy of low frequency EWS on ganglia mobilization have been lacking. Progress has also been limited by the absence of a validated pore-scale mechanistic explanation for ganglia transport enhancement.

Recently Beresnev *et al.* (2005), building on numerical simulations by Graham and Higdon (2000) and Iassonov and Beresnev (2003), have articulated a simple capillary-physics mechanism to explain ganglia mobilization by low frequency vibrations by considering the behavior of a single non-wetting droplet trapped at the entrance to a constriction in a tubular channel, as illustrated in Figure 4.1. The most salient feature of this

constricted pore geometry is that an excess capillary pressure is built on the internal side of the downstream meniscus as the droplet enters the pore constriction because the radius of the left (upstream) meniscus  $R^{left}$  is greater than the radius of the right meniscus  $R^{right}$ . Hence, an internal capillary-pressure imbalance  $P_c^{right} - P_c^{left}$  is created that resists the external gradient. As the droplet moves towards the narrowest part of the constriction, this capillary pressure imbalance increases. However, before this maximum capillary imbalance is reached, the droplet will become trapped if  $P_c^{right} - P_c^{left}$  becomes sufficiently large that it equals the driving static external pressure gradient,  $\Delta P_s$ . In such cases, the external gradient must be increased above an unplugging threshold,  $\Delta P_0$ , in order for the droplet to pass through the constriction.

In view of these considerations, the expected average flow rate as a function of external pressure gradient is shown in Figure 4.2. The expectation is that no flow occurs (and the droplet will be trapped) unless the static gradient  $\Delta P_s$  exceeds  $\Delta P_0$ . As  $\Delta P_s$  is increased from zero to  $\Delta P_0$ , only the equilibrium position of the trapped droplet changes (such that the resisting capillary pressure imbalance is identical in magnitude to  $\Delta P_s$ ). For values of  $\Delta P_s$  greater than the unplugging threshold, the flow would be expected to follow the Darcy law.

If the static external gradient  $\Delta P_s$  is below the unplugging threshold  $\Delta P_0$  and a longitudinal vibration of the wall parallel to the pore axis is applied, an inertial force  $P_{osc}$  on the fluid will be induced with the amplitude of approximately  $\rho_f a_0$ , where  $\rho_f$  is the average density of the fluid and  $a_0$  is the acceleration amplitude of the wall (Biot, 1956). The instantaneous total combined positive force on the fluid then becomes  $P_{osc} + \Delta P_s$ . One cycle of this combined force is shown on a vertical scale in Figure 4.2 for an acceleration amplitude sufficiently large so that  $P_{osc} + \Delta P_s$  exceeds  $\Delta P_0$  during part of the vibration cycle. In the positive half-period of vibrations, when the total forcing exceeds  $\Delta P_0$ , the ganglion is instantly unplugged and moves forward, whereas, when the vibration reverses direction, the ganglion is once again plugged. Consequently a rectification effect occurs, leading to a “nudging” motion of the ganglion through the constriction in the positive half-cycles. After a number of cycles, the ganglion is mobilized.

At least two specific predictions based on this mobilization mechanism follow. First, for a fixed vibration frequency, the effect will grow with increasing acceleration amplitude of vibrations, which will simply increase the amplitude of  $P_{osc}$ . However, as the acceleration amplitude continues to increase, eventually no further ganglia mobilization will be realized as the negative half cycles of each vibration will begin sampling large parts of the negative flow portion of the flow curve in Figure 4.2 and the system will conform to the usual Darcy flow. Second, the net displacement of the ganglion over one period of vibrations will depend on how much time it spends in the unplugged position. For constant acceleration amplitude, therefore, the effect will be inversely proportional to the frequency. Furthermore, for sufficiently large frequencies, the vibrations will become ineffectual as the ganglia response time becomes large compared to the vibration period. The ganglion response time, sometimes called the “viscous diffusion time”, is the characteristic time scale over which the fluid responds to a step forcing,  $\tau = \rho_f r^2 / \mu$ , where  $r$  is the radius of the pore channel and  $\mu$  is the dynamic viscosity (Johnson, 1998).

The purpose of this study is to validate these predictions using a two-dimensional etched-glass micromodel.

#### 4.2. Experimental apparatus and protocol

An etched glass quasi-two-dimensional micromodel, a shaker, and a digital camera were used to study the effects of external vibration on the transport of oil ganglia in a water-flooded pore network. The horizontally-mounted micromodel consists of a 50 x 50 square lattice of circular “pores” connected by straight channel “throats”, as shown in Figure 4.3. The non-uniform pore and throat diameters are approximately normally distributed and have mean values of 2.30 *mm* and 0.76 *mm*, respectively. The distance between the centers of nearest-neighbor pores is 3.80 *mm*. The total length of the lattice is 19 *cm*. Mirror images of the pattern were etched to a depth of approximately 0.30 *mm* using precision sandblasting (Bancheros Glass & Etching Inc.). Following etching, the plates were aligned and annealed in a muffle furnace. The resulting total volume of the voids (pores + throats) was approximately 1.6 *cm*<sup>3</sup> and the porosity was 0.44.

At the beginning of each experiment the air in the initially empty micromodel was displaced by pressurized carbon dioxide (which is more water-soluble than air) for approximately ten minutes in order to reduce the long-term presence of trapped gas bubbles. Deionized water was then pumped into the micromodel at a low flow rate until all the gas was displaced and the pores and throats were completely filled with water. Subsequently, the water flow was turned off and trichloroethylene (TCE), which is a typical organic groundwater contaminant with density  $1.46 \text{ g/cm}^3$  at  $20^\circ\text{C}$  (David, 1998-1999a) and viscosity  $0.545 \text{ mPa sec}$  at  $25^\circ\text{C}$  (David, 1998-1999b), was pumped into the micromodel until nearly all the water was displaced. The interfacial tension between TCE and water is  $0.0345 \text{ N/m}$  (Weiss, 1986). The TCE contained catalytic amounts of organic dye (Oil Blue N) to facilitate visualization. Oil Blue N is insoluble in water. Once the micromodel was filled with TCE, the flow of organic fluid was stopped and a gravity feed system, described below, was used to push deionized water through the micromodel at a constant pressure drop (typically  $700 \text{ Pa}$ ). The resulting water flow rate through the micromodel increased slowly with time as ganglia were mobilized and displaced, thereby increasing the permeability. Over the course of a typical experiment, the average volumetric flow rate of water was  $0.08 \text{ ml/min}$ , which corresponds to a mean residence time of  $20 \text{ min}$ .

In order to ensure that a constant pressure drop was maintained across the flow cell and to eliminate pulses associated with fluid pumping, a gravity-driven fluid feed system was used during the water flood portion of the experiment. A Masterflex peristaltic cartridge pump was used to deliver degassed deionized water from a sealed reservoir to a filled  $140 \text{ ml}$  flask suspended over a shallow overflow box, thereby maintaining a constant height free surface at the top of the flask. A 1/8-inch tube (TYGON) was used to carry water from the flask to the feed port of the micromodel. A similar tube carried effluent from the exit port of the micromodel to a collection vessel. Because the volumetric flow rates used in these studies are low, the only portion of the exit tube that is continuously and completely filled with effluent is the region between the exit port and the location where the tube reaches its maximum elevation. In the remaining portion of the exit tube the fluid flows drop-wise as it empties into the effluent collection vessel. As a consequence of this design, flow through the micromodel is driven by a constant pressure gradient that is determined by the difference

between the elevations of the free surface at the top of the feed flask and the highest point in the exit tube. Hence, the constant pressure driving force can easily be manipulated by simply changing the relative elevations of the feed flask and the maximum exit tube height.

The displacement of TCE by water was monitored using an optical imaging system. Specifically, a Canon PowerShot A40 color digital camera connected to a PC was mounted on a stage directly above the micromodel, as shown schematically in Figure 4.4. Captured images of the micromodel have a resolution of 1200 x 1600 pixels. Uniform illumination of the micromodel was provided by 5000 K light transmitted from a light box (CL-5000M, CABIN) mounted approximately two inches underneath the horizontal micromodel. The image-analysis software Image-Pro Plus 4.5.1 was used to calculate the fractional area of pores and throats occupied by the dye-containing TCE. In a typical no-vibration experiment, the TCE reached a constant residual saturation of approximately 15% of the pore/throat area within 300 *hours* after commencing the water flood.

Horizontal vibration of the micromodel parallel to the imposed external pressure gradient was carried out using a Bruel & Kjaer vibration exciter (Type 4809). The micromodel was mounted in a Teflon-sleeved frame (which allowed the glass micromodel to translate smoothly), and the assembly was connected to the vibration exciter shaft. The displacement amplitude and the frequency of the vibration exciter shaft were controlled by a function generator (Phillips PM5134) and a power amplifier (Bruel & Kjaer type 2706). The resulting acceleration amplitude of the micromodel was measured using an Industrial Monitoring Instrumentation accelerometer (Model 326A02). In addition, a pressure transducer (Cole Parmer) placed upstream of the micromodel was used to measure the water inlet pressure.

### 4.3. Results and discussion

#### 4.3.1. Estimation of conditions for ganglia entrapment

Using the general form of the Laplace equation for non-spherical menisci, the maximum difference in capillary pressure along a trapped ganglion in the micromodel can be estimated as  $P_c^{right} - P_c^{left} = \sigma (1/R^{throat} - 1/R^{pore}) = 61 Pa$ , where  $\sigma$  is the TCE/water interfacial

tension and  $R^{throat}$  and  $R^{pore}$  are the respective mean radii. The typical length of entrapped ganglia in the absence of vibrations was observed to be approximately four lattice units, therefore the capillary pressure gradient trapping the ganglia was approximately  $61 Pa / (4 \times 0.0038 m) = 4.0 \times 10^3 N/m^3$ . Since all experiments were conducted under a  $700 Pa$  total external pressure drop, the pressure gradient exerted on ganglia by the water was on average only approximately  $700 Pa / 0.19 m = 3.7 \times 10^3 N/m^3$ , which was less than the value necessary to mobilize the ganglia. Based upon these calculations, it is possible to estimate the magnitude of the equivalent oscillatory body force  $\rho_f a_0$  needed to mobilize trapped fluid in the micromodel if the experiment were conducted with vibration. In particular, the maximum oscillatory body force exerted on the TCE ganglia would be  $0.73 \times 10^3 N/m^3$  for an acceleration amplitude of  $0.5 m/sec^2$ , which would result in a combined total forcing of  $4.4 \times 10^3 N/m^3$ , which would exceed the threshold to overcome the resistive capillary force. Hence, vibration experiments were performed using acceleration amplitudes of at least  $0.5 m/sec^2$ .

#### 4.3.2. Repeatability of experiments

Three water flood experiments were performed in the absence of vibration until the TCE reached a constant residual saturation, as shown in Figure 4.5. The overall trends of the three curves are similar, especially during the initial stages of displacement, but they become more divergent as they approach asymptotic residual saturation ( $\sim 10\%$ - $20\%$  of the initial TCE volume fraction). These differences are probably attributable to statistical fluctuations associated with the lattice size (only  $50 \times 50$  nodes). In particular, the residual saturation will depend sensitively upon the initial percolation pathways.

Three experimental runs were also conducted at a vibration frequency of  $10 Hz$  and acceleration amplitude of  $3.5 m/sec^2$  from the time the water was introduced into the micromodel until the TCE in the micromodel reached residual saturation. Figure 4.6 shows the normalized area of the residual TCE as a function of time for these three experiments. The repeatability for these conditions is excellent and better than that found for the no-vibration case. Because the vibratory forcing acts on all parts of the micromodel simultaneously and without discrimination, the likelihood of developing percolation

pathways that bypass large portions of the flow cell (thereby leading to larger fluctuations from one experiment to the next) is diminished.

#### 4.3.3. Frequency effect

Experiments under vibration were carried out at a constant acceleration amplitude of  $3.5 \text{ m/sec}^2$  and at frequencies of 10, 30, 60 *Hz*, to discern the effect of vibration frequency on ganglia mobilization. The order of magnitude of the ganglion response time in the experiment can be estimated as  $\tau \approx 10^3 \text{ kg/m}^3 \times (10^{-3} \text{ m})^2 / 10^{-3} \text{ Pa sec} = 1 \text{ sec}$ , showing that both of the mechanisms of the frequency-dependence of the mobilization outlined in the Introduction are operational under the conditions of the experiment. Frequencies lower than 10 *Hz* were not investigated because, for fixed acceleration amplitude, the required displacement amplitude increases according to the inverse relation  $a_x \propto \frac{1}{f^2}$ , where  $f$  is the frequency, which results in displacement amplitudes outside the range of capability of the shaker.

Results are presented in Figure 4.7, which shows the normalized residual TCE area as a function of time. Also plotted are the results for the no-vibration case. In all cases with vibration, the TCE area declined much quicker and reached a lower asymptotic residual saturation than for the case with no vibrations. Furthermore, an inverse dependence of TCE removal rate on the frequency was observed, as anticipated by the capillary physics mechanism outlined earlier, with the highest rate occurring at the lowest frequency (10 *Hz*). Moreover, the difference between the TCE displacement curves for the experiments carried out at 30 and 60 *Hz* was not as large as the difference between the curves for the 10 and 30 *Hz* cases, which can be understood recalling that the vibration periods in the former two cases were already much smaller relative to the ganglion response time, explaining the inefficiency of vibrations at such high frequencies.

#### 4.3.4. Acceleration amplitude effect

Three experiments at a fixed vibration frequency of 30 *Hz* were performed for acceleration amplitudes of 0.5, 1.8, 3.5, and 5.0  $\text{m/sec}^2$ . Plots of normalized TCE area as a

function of time for these experiments, as well as for the no-vibration case are shown in Figure 4.8. It can be seen that as the acceleration amplitude is increased, the rate of displacement of TCE increases and the asymptotic TCE residual saturation drops, as predicted by the capillary physics mechanism. It also appears that as the acceleration amplitude is increased, eventually no further decreases in the residual saturation will be observed. As was discussed above, based upon the mean pore and throat diameters, the minimum acceleration amplitude needed to mobilize trapped ganglia can be estimated to be  $0.5 \text{ m/s}^2$ . The experimental result for this acceleration amplitude is consistent with this prediction.

#### 4.4. Summary

Quasi-two-dimensional glass-micromodel experiments were carried out to validate predictions of a capillary physics mechanism of organic-ganglia mobilization under the influence of low frequency vibrations. For fixed acceleration amplitude, TCE is more quickly displaced in a water flood experiment as the vibration frequency decreases from 60 to 10 *Hz*. For fixed vibration frequency, TCE displacement is more efficient as the acceleration amplitude was increased from  $0.5 \text{ m/s}^2$  to  $5.0 \text{ m/s}^2$ . These findings are consistent with trends predicted by the capillary physics mechanism.

The increase in the rate of TCE production proportional to the amplitude and inversely proportional to the frequency is explained by the vibrations preventing the entrapment of ganglia at any given instant of time: ganglia that would have been trapped in a non-aided flow are able to overcome the capillary barrier due to the nudging effect when the system undergoes vibrations.

Additional studies are necessary to generalize these findings before low frequency vibratory stimulation can be employed reliably in the field. In particular, experiments need to be carried out for more realistic pore and throat dimensions and converging-diverging pore geometries typically found in oil reservoirs. Also, the effects of fluid and solid properties, as well as interfacial and wetting characteristics need to be elucidated. However, the results of this work demonstrate that even a model based upon a simplified representation of the pore

scale phenomena can provide significant insight into the behavior of more complicated systems and can be used to verify underlying physics.

#### 4.5. Acknowledgements

This work was supported by the National Science Foundation award EAR-0125214 and the Department of Energy award DE-FC26-01BC15165. The authors would like to thank J. Adin Mann for providing the function generator, amplifier and vibrator used in this work, and W. Pennington and R. Turpening for stimulating discussions.

#### 4.6. References

- Beresnev, I.A., and Johnson, P.A., (1994). Elastic-wave stimulation of oil production: A review of methods and results. *Geophysics*, 59(6), 1000-1017.
- Beresnev, I.A., Vigil, R.D., Li, W., Pennington, W.D., Turpening, R.M., Iassonov, P.P., and Ewing, R.P., (2005). Elastic waves push organic fluids from reservoir rock. *Geophysical Research Letter*. 32(13), L13303, doi:10.1029/2005GL023123.
- Biot, M.A., (1956). Theory of propagation of elastic waves in a fluid-saturated porous solid. II. Higher frequency range, *Journal of Acoustical Society of America*, 28, 179-191.
- David, R.L., (1998-1999a). CRC Handbook of Chemistry and Physics, 79<sup>th</sup> ed., CRC Press, Washington, D.C., pp.3-164.
- David, R.L., (1998-1999b). CRC Handbook of Chemistry and Physics, 79<sup>th</sup> ed., CRC Press, Washington, D.C., pp.6-170.
- Fountain, J.C., Klimek, A., Beikirch, M.G., and Middleton, T.M., (1991). The use of surfactants for *in situ* extraction of organic pollutants from a contaminated aquifer. *Journal of Hazardous Materials*, 28(3), 295-311.
- Graham, D.R., and Higdon, J.J.L., (2000). Oscillatory flow of droplets in capillary tubes. Part 2. Constricted tubes. *Journal of Fluid Mechanics*, 425, 55-77.

- Iassonov, P.P., and Beresnev, I.A., (2003). A model for enhanced fluid percolation in porous media by application of low-frequency elastic waves. *Journal of Geophysics Research*, B 108(3), 2138.
- Iyer, R., (2001). Electrokinetic remediation. *Particulate Science and Technology*, 19(3), 219-228.
- Jawitz, J.W., Dai, D.P., Rao, P.S.C., Annable, M.D., and Rhue, R.D., (2003). Rate-limited solubilization of multicomponent nonaqueous-phase liquids by flushing with cosolvents and surfactants: Modeling data from laboratory and field experiments. *Environmental Science & Technology*, 37(9), 1983-1991.
- Johnson, R.W., (1998). *The Handbook of Fluid Dynamics*, CRC Press, pp.9-11.
- Oostrom, M., Hofstee, C., Walker, R.C., and Dane, J.H., (1999). Movement and remediation of trichloroethylene in a saturated heterogeneous porous medium: 1. Spill behavior and initial dissolution. *Journal of Contaminant Hydrology*, 37(2), 179-197.
- Pennell, K.D., Jin, M., Abriola, L.M., and Pope, G.A., (1994). Surfactant enhanced remediation of soil columns contaminated by residual tetrachloroethylene. *Journal of Contaminant Hydrology*, 16(1), 35-53.
- Reddi, L.N., and Challa, S., (1994). Vibratory mobilization of immiscible liquid ganglia in sands. *Journal of Environmental Engineering* (New York, N.Y.), 120(5), 1170-1190.
- Reddy, K.R., ASCE, M., and Saichek, R.E., (2003). Effect of soil type on electrokinetic removal of phenanthrene using surfactants and cosolvents. *Journal of Environmental Engineering*, 129(4), 336-346.
- Roberts, P.M., Esipov, I.B., and Majer, E.L., (2003). Elastic wave stimulation of oil reservoirs: Promising EOR technology? *The Leading Edge*, 22(5), 448-453.
- Roberts, P.M., Sharma, A., Uddameri, V., Monagle, M., Dale, D.E., and Steck, L.K., (2001). Enhanced DNAPL transport in a sand core during dynamic stress stimulation. *Environmental Engineering Science*, 18(2), 67-79.
- U.S., EPA., (1990). *Handbook on in Situ Treatment of Hazardous Waste Contaminated Soils*, EPA/540/2-90/002, Environmental Protection Agency, Washington, D.C.
- Weiss, G., (1986). *Hazardous Chemicals Data Book*, 2<sup>nd</sup> ed., Noyes Data Corporation, Park Ridge, NJ., pp.974.

#### 4.7. Figure captions

Figure 4.1. Schematic of droplet flow through a horizontal straight channel with a constriction under a static pressure gradient  $\Delta P$ . The radii of the trailing and leading droplet meniscii are labeled as  $R^{left}$  and  $R^{right}$ , respectively (as shown,  $R^{left} > R^{right}$ ). The corresponding internal capillary pressures are given by  $P_c^{left}$  and  $P_c^{right}$ .

Figure 4.2. Average flow rate as a function of the combined static pressure and vibratory pressure, explaining the mobilization mechanism.

Figure 4.3. Photograph of the two-dimensional micromodel filled with dyed TCE.

Figure 4.4. Schematic of experimental apparatus layout.

Figure 4.5. Measured TCE area (normalized by initial TCE area equal to the total void area) versus time for three repeated experiments with no vibration.

Figure 4.6. Measured TCE area (normalized by initial TCE area) versus time for three repeated experiments with vibration frequency of 10 Hz and acceleration amplitude of  $3.5 \text{ m/sec}^2$ .

Figure 4.7. Normalized TCE area versus time for experiments carried out at different vibration frequencies but at constant acceleration amplitude ( $3.5 \text{ m/sec}^2$ ). Also plotted for comparison is the result for the case with no vibration. ( $\diamond$ : No vibration, +: 10 Hz,  $\Delta$ : 30 Hz,  $\square$ : 60 Hz)

Figure 4.8. Normalized TCE area versus time for experiments carried out at different acceleration amplitudes but at constant vibration frequency (30 Hz). Also plotted for comparison is the result for the case with no vibration. ( $\square$ : No vibration,  $\Delta$ :  $0.5 \text{ m/s}^2$ , x:  $1.8 \text{ m/s}^2$ ,  $\diamond$ :  $3.5 \text{ m/s}^2$ , +:  $5.0 \text{ m/s}^2$ )

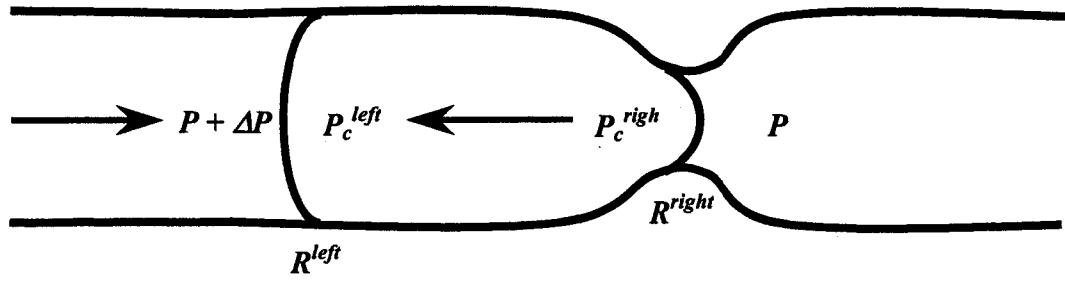


Figure 4.1

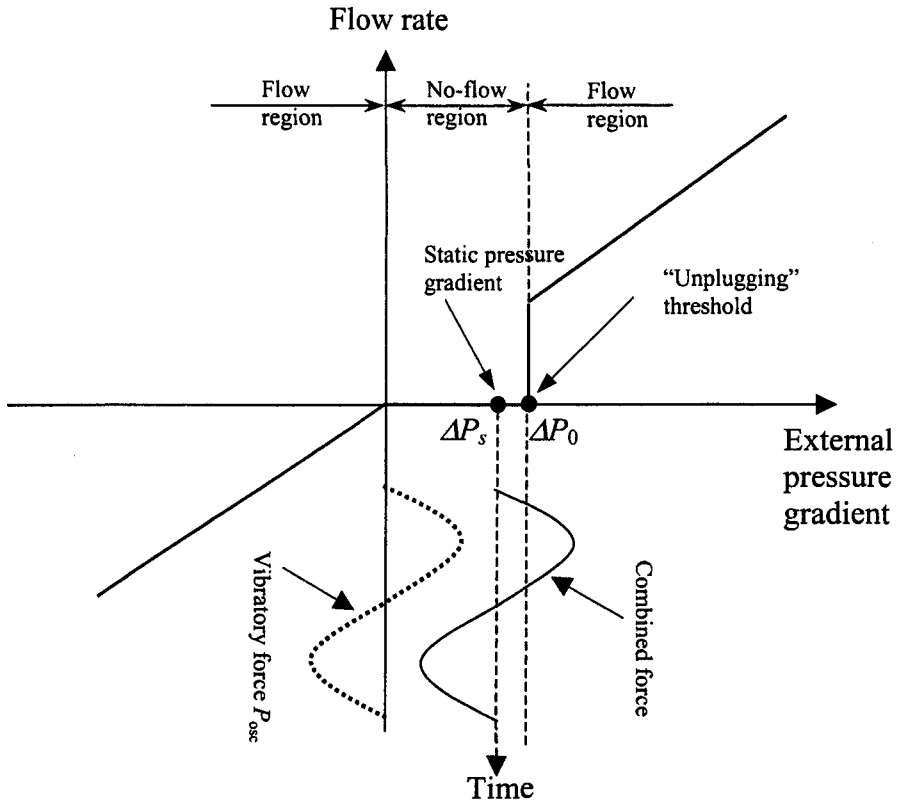


Figure 4.2

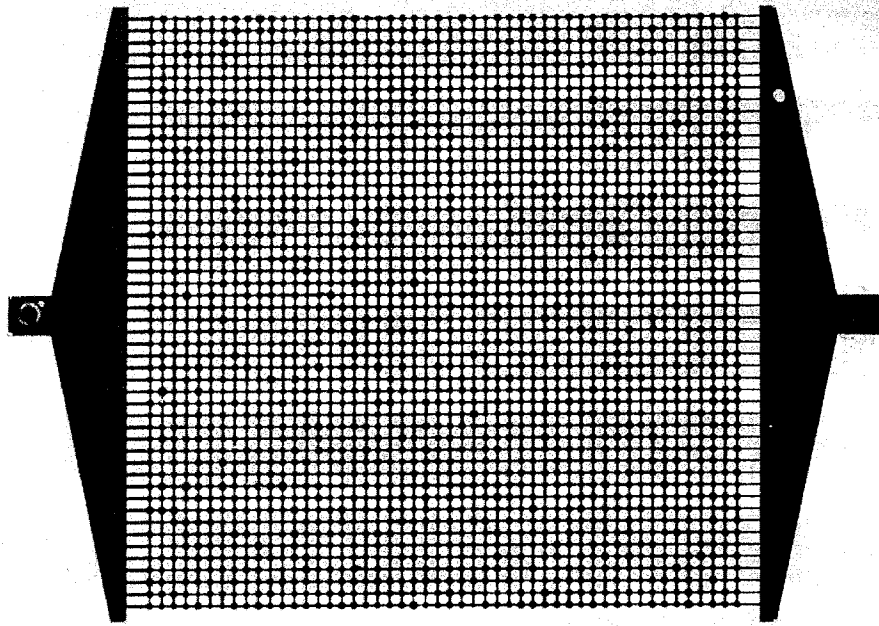


Figure 4.3

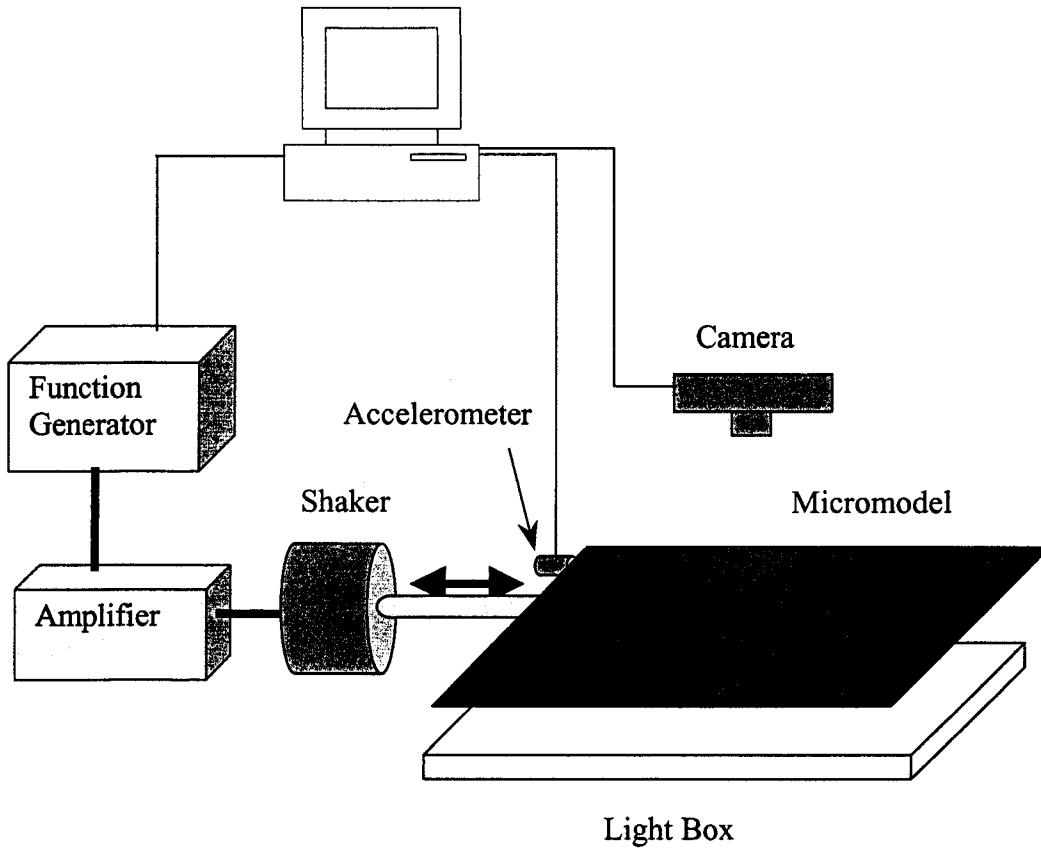


Figure 4.4

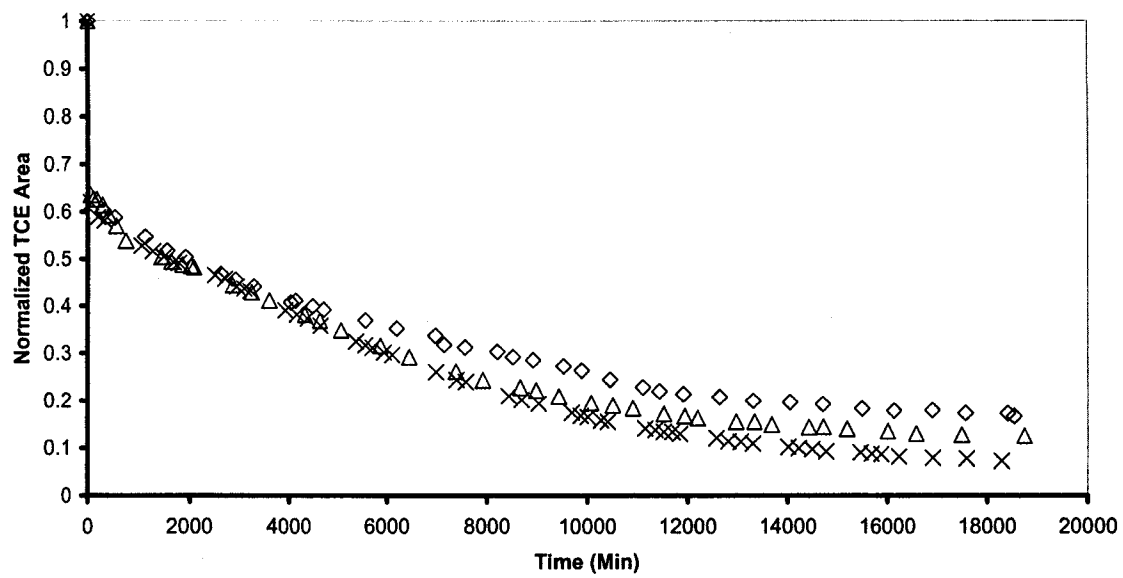


Figure 4.5

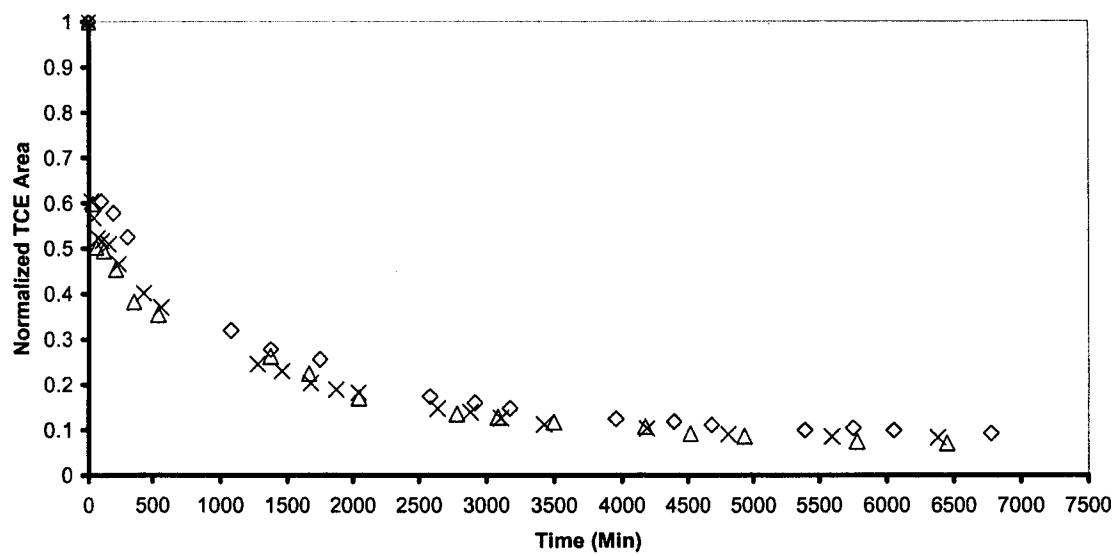


Figure 4.6

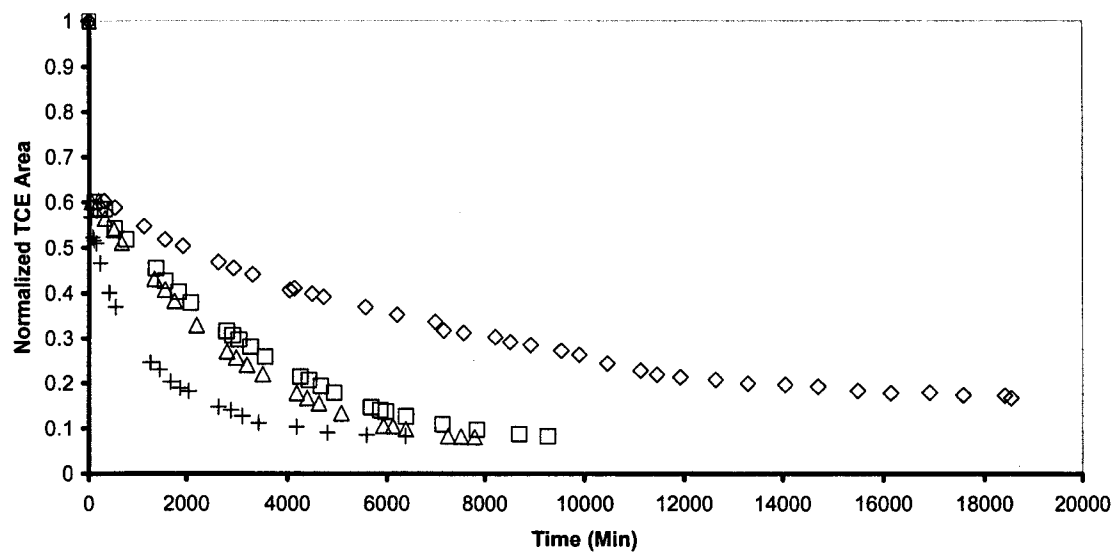


Figure 4.7

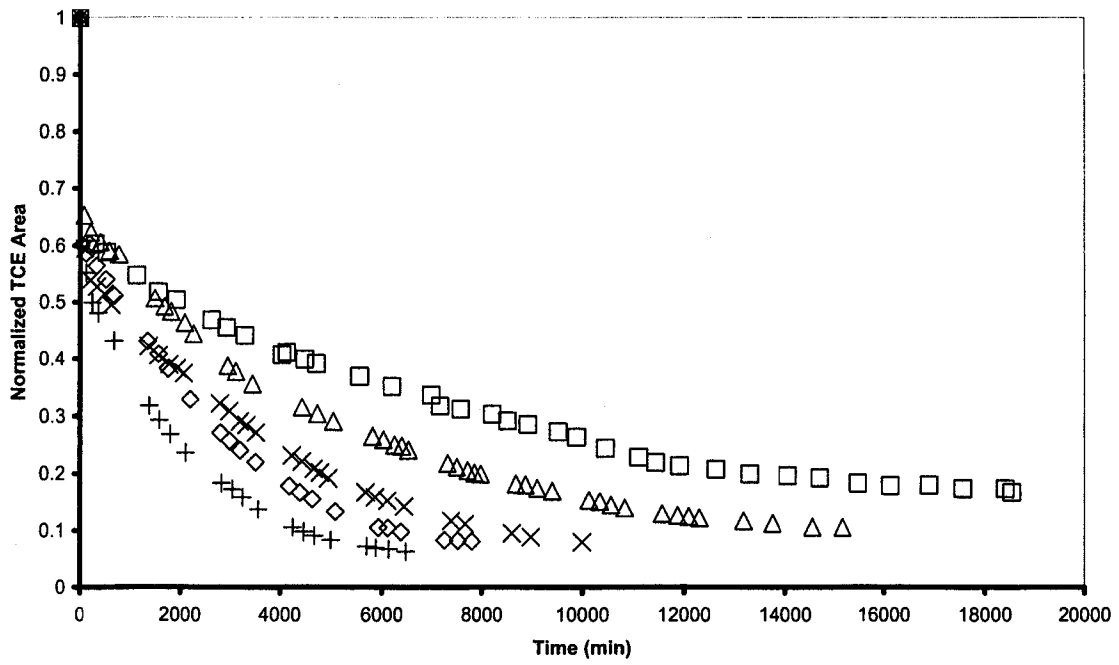


Figure 4.8

## **CHAPTER 5. VIBRATION-INDUCED MOBILIZATION OF TRAPPED OIL GANGLIA IN POROUS MEDIA: DROPLET FLOW AND STIMULATION EFFECTS IN A REALISTIC CONVERGENCE DIVERGENCE CHANNEL**

Wenqing Li, R. Dennis Vigil, Igor A. Beresnev

A paper to be submitted to *Journal of Colloid and Interface Science*

### **Abstract**

Enhancement of the mobility of residual oil in petroleum engineering is becoming increasingly important as world petroleum demand continues its rapid rise and easily accessed supplies are depleted. In addition, the efficient removal of dense non-aqueous phase liquid contaminants trapped in underground aquifers is still a major issue in the field of environmental remediation. One promising and environmentally benign method for mobilizing trapped oil ganglia in porous media is to use low-frequency vibrations. Recently, a simple capillary physics mechanism has been developed to explain the stimulation effects of low-frequency vibrations, and several predictions based upon this mechanism have been verified by carefully controlled experiments. In this paper, the effects of vibrations on the mobilization of trapped oil ganglia are studied using computational fluid dynamics simulations for the flow of a droplet in a constricted capillary channel using realistic length scales typically found in oil reservoirs and underground aquifers. These simulations show that the vibrations become more effective in mobilizing trapped oil droplets as the vibration frequency decreases and the acceleration amplitude increases, which is consistent with predictions based upon the capillary physics mechanism as well as experimental evidence.

### **Keywords**

Elastic wave stimulation, multiphase flow, porous media, acoustic stimulation, enhanced oil recovery, non-aqueous phase liquids, computational fluid dynamic, CFD, FLUENT

## 5.1. Introduction

Beresenev, et al. (2005) hypothesized a simple capillary physics mechanism to explain how low-frequency vibrations could mobilize oil ganglia trapped in constricted pores. Their analysis is based on consideration of a single droplet trapped in a straight but constricted channel under a fixed external pressure gradient. If the superposition of a vibratory force on the static pressure gradient is sufficiently large to overcome (at least during some part of the vibration cycle) the capillary forces that hinder the flow of the droplet, then mobilization will occur. Hence, it is possible to reduce the minimum external pressure gradient required to attain the unplugging threshold to overcome the inhibitory capillary forces. A more detailed analysis of the superposition of a vibratory body force on the static pressure gradient leads to at least two specific predictions including: (1) mobilization of ganglia by vibrations should become more effective at lower (but non-zero) vibration frequencies than high frequencies, and (2) mobilization of ganglia by vibrations should become more effective as the acceleration amplitude of the vibrations increases, but this improvement will reach a plateau as the acceleration amplitude reaches sufficiently large values. These predictions have been confirmed by recent optical experiments carried out by Li *et al.* (2005) using a quasi two-dimensional glass micro-model attached to a shaker.

The purpose of this study is to further validate the predictions of the capillary physics mechanism for ganglia mobilization by carrying out a computational fluid dynamics (CFD) study of the behavior of a single trapped droplet in a straight constricted pore. Although a number of studies have previously examined droplet flow through constricted tubes using CFD methods, the existing literature does not explicitly address mobilization in micron sized or smaller pores due to the imposition of vibratory body forces. For example, Leyrat-Maurin and Barthes-Biesel (1994) developed a model for a low Reynolds number flow of a capsule passing through a constriction under the condition of either constant flow rate or constant pressure drop, but in the absence of any imposed oscillating body forces.

The most closely related studies were carried out by Graham and Higdon (2000a; 2000b), who investigated the motion of droplets in both straight and constricted capillary tubes subjected to the combined action of a mean pressure gradient and an oscillatory body

force. They demonstrated that a threshold pressure gradient exists for droplet unplugging when the flow is driven only by a static pressure. The superposition of an oscillatory body force was shown to be helpful for mobilizing trapped droplets when the oscillatory force exceeded a system-related threshold and the oscillatory frequency was kept below a critical value. However, most of their simulation were based on the assumption that the material-property number,  $\rho_f \sigma h / \mu^2$ , was zero. Because  $h$  represents the minimum radius of the constriction,  $\mu$  is the viscosity of the fluid,  $\rho_f$  is the density of the droplet, and  $\sigma$  is the interfacial tension between the two phases, it is impossible for the material-property number to be zero unless the interfacial tension goes to zero, which means that there is no capillary force. Moreover, when one applies Graham and Higdon's dimensionless simulation results to pores with sizes relevant to oil ganglia trapped in reservoir rock, the oscillatory frequencies obtained are greater than 1000 Hz. These high frequencies are ineffective for fluid mobilization because the vibration period is significantly shorter than the fluid response time and are not of interest in field applications. For example, Graham and Higdon report results for dimensionless frequency  $f = 0.00127$  ( $f = \mu a / (\gamma \tau)$ ). Using the viscosity  $\mu = 5.45 \times 10^{-4} \text{ kg / m.s}$  (David, 1998-1999b) for a typical organic solute, trichloroethylene (TCE); interfacial tension  $\gamma = 0.0345 \text{ N / m}$  (Weiss, 1986) for water-TCE; and a pore radius  $a = 4 \times 10^{-5} \text{ m}$ , the oscillatory frequency ( $1/\tau$ ) is approximately 2000 Hz.

Other problems exist when one tries to apply Graham and Higdon's simulation results to practical situations. For example, one cannot use their results to calculate the critical periodic frequency ( $1/\tau$ ) for a new oscillatory forcing  $F_w$  from the relationship they obtained between a critical dimensionless frequency ( $L/U_1\tau$ ) and an oscillatory forcing  $F_w$  because the bulk fluid velocity ( $U_1$ ) in the expression, which is under the condition of a single phase flow at the same mean forcing  $F_o$ , would change with  $F_w$ . Moreover, some of Graham and Higdon's dimensionless results, when applied to realistic pore geometries, produce significantly higher estimates of the minimum acceleration amplitudes needed to mobilize trapped ganglia than do the dimensional simulations presented in this paper. For example, in the description of their unsteady simulation results, they report that the critical oscillatory force  $F_w$  was about 0.21 when the dimensionless frequency  $f$  was 0.00127 under the

conditions that the relative drop size  $a/h=2$ , the viscosity ratio  $\lambda = 1$ , the density ratio  $\rho_D = 1$ , and  $F_o = 0.03$ . For pore mouth radii  $h = 2 \times 10^{-5} m$  and using their definitions

$F_o = G_o h^2 / \gamma$  and  $F_w = G_w h^2 / \gamma$ , the required critical oscillatory force is

$G_w = 18.11 \times 10^6 N/m^3$  and the constant force is  $G_o = 2.59 \times 10^6 N/m^3$ . Therefore, the critical acceleration amplitude can be estimated to be  $1.28 \times 10^4 m/s^2$  (using  $1.46 g/cm^3$  as the density of TCE from David, 1998-1999a) after subtracting the predefined constant body force in our case (equivalent to the static pressure drop  $\Delta P_s$ ,  $1300 Pa$ , divided by the length on which the pressure drop is imposed,  $L=6.4 \times 10^{-4} m$ ) from the required total force,  $F_o + F_w$ . Graham in Higdon's predicted acceleration amplitude threshold ( $1.28 \times 10^4 m/s^2$ ) is significantly larger than our simulation result,  $1900 m/s^2$ , for the same vibration frequency of  $2000 Hz$ .

Hence, despite the fact that Graham and Higdon's extensive simulations have shed considerable light on the understanding of how vibrations can enhance droplet flow in constricted tubes, the applicability of their results to realistic pore diameters is very limited. In particular, we are interested in the behavior of systems undergoing low frequency vibrations relevant to field-scale applications, typically in the range of  $1\sim 100 Hz$ . The remainder of the paper describes simulations using the commercial CFD software FLUENT that apply to these realistic pore diameters and practical vibration frequencies.

## 5.2. Problem formulation and numerical method

### 5.2.1. Problem formulation

We consider the flow of an immiscible oil droplet in a continuous water phase through a single straight constricted pore. Figure 5.2 shows the pore geometry, which was constructed with NURBS (Non-Uniform Rotational B-Spline) curve walls in the center portion and straight walls in the upstream and downstream portions. The constant pressure gradient can be implemented by setting as an equivalent constant body force or a set of boundary conditions such as setting the inlet pressure and the outlet pressure pair, which is

more reasonable and easier to simulate compared with the equivalent body force setting, hence we implement the constant pressure gradient by setting the inlet and outlet pressure pair in later simulations. The vibratory force can be accomplished by adding additional momentum source terms to the momentum equations using FLUENT's user-defined function feature. The specific source terms that must be added to the axial and radial momentum

equations are as follows:  $S_z = \rho[A_a \sin(2\pi ft) - \frac{A_a}{2\pi f} \cos(2\pi ft) \frac{\partial v_z}{\partial z}]$  and

$S_r = -\rho \frac{A_a}{2\pi f} \cos(2\pi ft) \frac{\partial v_r}{\partial z}$ , respectively.

### 5.2.2. Multiphase model

Three major multiphase models based on the Euler-Euler approach are available in FLUENT (Release: 6.1.22), the VOF (Volume of Fluid) model, the Mixture model and the Eulerian model. However, the VOF model is the most appropriate for simulating the behavior of a single droplet, and it can model two or more immiscible fluids by solving a single set of momentum equations and tracking the volume fraction of any phase throughout the domain. Other typical applications of the VOF model include the motion of large bubbles (gas or liquid) in a liquid and the steady or transient tracking of any liquid-gas interface. Unfortunately there are some limitations for the VOF model, such as the fact that the segregated solver must be used rather than the coupled solver, all control volumes must be filled with either a single fluid phase or a combination of phases rather than void regions where no fluid of any type fluid is present, only one of the phases can be compressible, species mixing and reacting flow cannot be modeled, and the second-order implicit time-stepping formulation cannot be used (FLUENT, 2003).

### 5.2.3. The governing equations

The governing equations for the two-dimensional axisymmetric pipe flow include the volume fraction equation (5.1), the continuity equation (5.2), the axial momentum equation (5.3), the radial momentum equation (5.4), and the energy equation (5.5).

$$\frac{\partial \alpha_q}{\partial t} + \vec{v} \cdot \nabla \alpha_q = \frac{S_{\alpha_q}}{\rho_q} \quad (5.1)$$

$$\frac{\partial \rho}{\partial t} + \frac{\partial}{\partial z}(\rho v_z) + \frac{\partial}{\partial r}(\rho v_r) + \frac{\rho v_r}{r} = 0 \quad (5.2)$$

$$\begin{aligned} \frac{\partial}{\partial t}(\rho v_z) + \frac{1}{r} \frac{\partial}{\partial z}(r \rho v_z v_z) + \frac{1}{r} \frac{\partial}{\partial r}(r \rho v_r v_z) = -\frac{\partial p}{\partial z} + \\ \frac{1}{r} \frac{\partial}{\partial z} \left[ r \mu \left( 2 \frac{\partial v_z}{\partial z} - \frac{2}{3} \left( \frac{\partial v_z}{\partial z} + \frac{\partial v_r}{\partial r} + \frac{v_r}{r} \right) \right) \right] + \frac{1}{r} \frac{\partial}{\partial r} \left[ r \mu \left( \frac{\partial v_z}{\partial r} + \frac{\partial v_r}{\partial z} \right) \right] \end{aligned} \quad (5.3)$$

$$\begin{aligned} \frac{\partial}{\partial t}(\rho v_r) + \frac{1}{r} \frac{\partial}{\partial z}(r \rho v_z v_r) + \frac{1}{r} \frac{\partial}{\partial r}(r \rho v_r v_r) = -\frac{\partial p}{\partial r} + \\ \frac{1}{r} \frac{\partial}{\partial z} \left[ r \mu \left( \frac{\partial v_r}{\partial z} + \frac{\partial v_z}{\partial r} \right) \right] + \frac{1}{r} \frac{\partial}{\partial z} \left[ r \mu \left( 2 \frac{\partial v_r}{\partial r} - \frac{2}{3} \left( \frac{\partial v_z}{\partial z} + \frac{\partial v_r}{\partial r} + \frac{v_r}{r} \right) \right) \right] - \\ 2 \mu \frac{v_r}{r^2} + \frac{2}{3} \frac{\mu}{r} \left( \frac{\partial v_z}{\partial z} + \frac{\partial v_r}{\partial r} + \frac{v_r}{r} \right) \end{aligned} \quad (5.4)$$

$$\frac{\partial}{\partial t}(\rho E) + \nabla \cdot (\vec{v}(\rho E + p)) = \nabla \cdot (k \nabla T + \vec{\tau} \cdot \vec{v}), \quad (5.5)$$

Where,

$\alpha_q$  : the  $q$ th fluid's volume fraction satisfying the constraint  $\sum_{q=1}^n \alpha_q = 1$  for total  $n$

( $n=2$  for two-phase flow) fluid phases in the system.

$v_z, v_r$  : axial and radial velocity, respectively.

$\vec{v}$  : velocity vector having two components  $v_r$  and  $v_z$  here.

$S_{\alpha_q}$  source term for the  $q$ th fluid (zero for this study).

$\rho_q$ : density of the  $q$ th fluid.

$\mu_q$  : viscosity of the  $q$ th fluid.

$\rho$  : density of the controlled domain calculated by the expression  $\rho = \sum_{q=1}^n \alpha_q \rho_q$  .

$\mu$  : viscosity of the controlled domain calculated by the expression  $\mu = \sum_{q=1}^n \alpha_q \mu_q$  .

$z$ : axial coordinate.

$r$ : radial coordinate.

$p$ : static pressure.

$k$ : thermal conductivity.

$T$ : temperature.

$\bar{\tau}$ : stress tensor.

$E$ : the internal energy per unit mass.

The energy equation (5.5) is not used in our calculations because we consider only isothermal systems. A simple immiscible two-phase incompressible flow is assumed because water is the continuous phase and TCE is the trapped oil bubble. Moreover, gravitational body forces are ignored and no rotation is assumed.

Furthermore, there are two external vibratory force terms added on the right hand sides of equations (5.3) and (5.4), respectively, which are coming from the vibration imposed on the whole geometry. Assuming that the system is vibrating in a sinusoidal wave with acceleration amplitude  $A_a$  and frequency  $f$  starting with the negative  $z$  axial direction first with phase angle of zero, it can easily be shown that the external force terms for equations

(5.3) and (5.4) are given by the expressions:  $S_z = \rho[A_a \sin(2\pi ft) - \frac{A_a}{2\pi f} \cos(2\pi ft) \frac{\partial v_z}{\partial z}]$  and

$S_r = -\rho \frac{A_a}{2\pi f} \cos(2\pi ft) \frac{\partial v_r}{\partial z}$ , respectively.

Finally, another source term, the additional tangential stress term, due to the surface tension between the two fluids, is also considered in the VOF model (hence it is called the surface tension model or continuum surface force model in FLUENT) in the form of

$S_{st} = \sigma \frac{\rho \kappa_1 \nabla \alpha_1}{(\rho_1 + \rho_2)/2}$ , where  $\sigma$  is the surface tension between the two phases;  $\kappa = \nabla \cdot \frac{n}{|n|}$ ,

which is the curvature; and  $n = \nabla \alpha_q$ , which is the surface normal defined as the gradient of the volume fraction of the  $q$ th phase. The wall adhesion is integrated with the surface tension model by specifying the contact angle (thereby it results in the adjustment of the curvature of the surface near the wall through the specific calculations of unit normals near the wall, hence it adjusts the source terms due to surface tension).

#### 5.2.4. The simulated geometry and computational grid

The simulated geometry is shown in Figure 5.2, which is an axisymmetric 2D (two-dimensional) constricted tube. The lengths of the upstream and the downstream portions with straight walls are each  $160\ \mu\text{m}$ , and the diameters are  $120\ \mu\text{m}$ . The center part of the geometry is enveloped by NURBS (Non-Uniform Rotational B-Spline) curve walls with the largest diameter of  $120\ \mu\text{m}$  at the inlet and the outlet and the smallest diameter of  $40\ \mu\text{m}$  in the center. Because calculations of surface tension effects on quadrilateral and hexahedral meshes have higher accuracy than those on triangular and tetrahedral meshes, quadrilateral meshes are used. A typical computational mesh is generated by the mesh generation package GAMBIT (version 2.2.30) and presented in Figure 5.3. Note that the meshing clusters to the walls and is almost uniformly distributed in the axial direction.

#### 5.2.5. Boundary and initial conditions

In the study, water is used as the continuous phase and trichloroethylene (TCE) is used as the oil bubble. Consequently the corresponding properties of the two phases such as densities, viscosities and interfacial tension are specified. No slip boundary conditions are set on the walls. The gauge pressure at the inlet is specified as  $1300\ \text{Pa}$  for the vibration effect studies and other different specific values for the unplugging threshold studies without vibration, while the gauge pressure at the outlet is always specified as  $0\ \text{Pa}$ , which is consistent with the natural condition. And the contact angle on the wall is set as  $170^\circ$ .

After initializing the simulations by setting all pressure, axial velocity, radial velocity, and bubble volume fraction values as zeros, a circular region with radius  $40\ \mu\text{m}$  is patched symmetrically upstream of the constriction to denote the initial position of the oil bubble.

#### 5.2.6. Solution methods and convergence criterion

A control-volume based technique is used by FLUENT to convert the governing equations to algebraic equations that can be solved numerically. The following solution strategies for the VOF model are used to improve the accuracy and convergence of the solutions: PRESTO scheme (PREssure Stagging Option) for pressure interpolation scheme,

the second-order discretization scheme for the volume fraction equation (in order to sharpen the interface between phases), PISO (Pressure Implicit with Splitting of Operators) for pressure-velocity coupling scheme (allowing for increased values on all under-relaxation factors without a loss of solution stability), a second order upwind discretization scheme for momentum equations, and the most accurate Geometric Reconstruction scheme for the VOF model in FLUENT (to obtain the fluid-fluid interface by interpolation). The segregated solver provided by FLUENT solves the governing equations sequentially.

Several iterations must be performed before a converged solution is obtained at each time step because of the nonlinear and coupled governing equations and the implicit formulation. In each iteration, the following steps must be taken and continued until the convergence criteria are met: the fluid properties are updated based on the current solution or initial values; the momentum equations are solved in turn to update the velocity field; a “Poisson-type” equation for the pressure correction is derived from the continuity equation and the linearized momentum equation, and then it is solved to obtain the necessary corrections to the velocity field, pressure field and face mass fluxes such that continuity is satisfied; the vibratory and surface tension source terms are updated; finally the convergence criteria are checked.

As for the convergence criteria, scaled residuals, which are defined by the ratios of total residuals summed over all the computational cells to the corresponding total absolute values, are more appropriate than raw un-scaled residuals for most problems. Therefore these scaled residuals are used to determine convergence. Specifically, all scaled residuals were required to be less than  $10^{-4}$  for convergence to be satisfied. More rigorous convergence criteria do not significantly change the accuracy of the solution.

### **5.3. Results and discussion**

#### **5.3.1. Mesh sensitivity study**

The accuracy of the numerical simulations depends on the meshing on which the simulation is done. In general, the more refined the computational mesh, the higher the accuracy of the solution. Of course, a longer calculation time will be needed because more

computational nodes are involved and a smaller time step is required (resulting from the decreased minimum space interval). When the mesh is fine enough, the simulation results won't change much by further mesh refinement.

To verify the accuracy of the numerical scheme, mesh sensitivity studies were conducted based on three different mesh resolutions, as shown in Table 5.1. The trapped drop profiles are shown for these three meshes in Figure 5.4 for the case in which the flow is driven by a static external pressure gradient only (no vibrations) which is lower than the unplugging threshold needed to make the droplet pass through the constriction. All the drop profiles are similar, although as expected, Mesh 3 has the sharpest interface while Mesh 1 has the most vague interface, and Mesh 2 is in the middle level. The corresponding pressure profiles along the main axis when the drop is trapped are presented in Figure 5.5, which shows very little variation in the pressure profiles as the mesh resolution is changed. Given the similarity among the different meshes in terms of the trapped drop profiles and the pressure profiles as a function of axial position, it was concluded that Mesh 2 was sufficient for the calculations from the perspective of accuracy, calculation time, and computational cost, and hence it was used extensively in this work.

### **5.3.2. Results for a constant external pressure gradient only**

We begin our study under a fixed external pressure gradient only before we characterize the behavior of the droplet flow subject to a vibratory force or combination of a constant and a vibratory force.

For droplet flow, the drop velocity and bulk velocity will depend on the droplet deformation along with the continuous phase passing through the convergence divergence tube for the case of constant physical fluid properties. Furthermore, the deformation of the drop is also related to the initial drop size. To make the drop pass through the constricted capillary tube, the larger the initial size, the more deformation (hence the higher external forces) is needed. The smaller the drop size, the less deformation is required. If the drop diameter is smaller than the constriction diameter, than the drop can pass without undergoing any deformation. Since our goal is to investigate the stimulation effects of trapped droplet in a constricted tube under vibratory forces, a droplet with a diameter larger than the

constriction is a necessity. Throughout this study, the diameter of the initial drop was chosen to be twice the diameter of the narrowest part of the constriction, i.e.  $80\ \mu\text{m}$ .

According to the mechanism hypothesized by Beresenev, *et al.* (2005), there exists an unplugging external pressure gradient threshold at which the droplet will pass through the constriction. When this threshold is surpassed, the pore will become unplugged and the flow rate should increase with further increases in the pressure gradient. This expected behavior was indeed observed as can be seen in Figure 5.6, which also shows that the unplugging pressure gradient is around  $1440\ \text{Pa}$ . Moreover, it can be seen that there is a nearly linear relationship between the average bulk flow rate and the applied pressure gradient whenever the pressure gradient is greater than the unplugging value, whereas average bulk flow rate is zero when the pressure gradient is below the unplugging threshold.

The positive dependence shown above can be understood that a shorter passing time is needed for the higher-pressure gradient case, which is consistent with the simulation results presented in Figure 5.7, which shows that the time percentages when the center of the trapped droplet passes through the middle point of the constricted tube and when the most right hand side of the droplet passes through the outlet decrease as the pressure gradient increases, in a fixed total running time period. Since the two sets of time percentages have similar trends, although a larger difference between them is observed for a higher-pressure gradient, either of them is enough to characterize the efficiency of pressure gradient in terms of droplet mobilization and flow enhancement. Hence, only the time percentage when the center of the droplet passes through the middle point of the constricted tube is reported in the later discussions.

Actually different droplet behaviors are shown along the capillary tube. In the beginning the drop flows almost without deformation in the upstream, but gradually changes its shape as it gets close to the constricted area, and reaches the maximum deformation as the droplet moves through the narrowest part of the tube. After the drop squeezes through the throat of the channel, the drop enters into the downstream, the wider section of the channel, by following the wall contour closely before separating from the wall and regaining its spherical shape in the remainder of the downstream portion of the flow. Droplet breakup can

occur as the drop emerges from the constriction if the applied pressure gradient is sufficiently large, but we do not consider such cases.

### **5.3.3. Results for combination of an external pressure gradient and a vibratory force**

Based on the discussion above, the external pressure gradient must be greater than the unplugging threshold to mobilize the trapped droplet if only a constant pressure gradient is imposed on the fluids. However, it is often difficult and inefficient to implement a high constant unplugging pressure gradient in the field. This required minimum pressure gradient can be reduced by adding a vibratory body force to the static pressure gradient. Moreover, using a vibratory force may eliminate the likelihood of forming narrow percolation pathways that bypass large pores and throats if only a static pressure gradient is applied.

Since implementation of a combination of vibratory forces and constant forces is a generalization of the two cases where either vibratory forces or constant forces are imposed, we conduct stimulations under the co-existence of them. To study the efficacy of vibratory forces, the external pressure gradient is chosen to be less than the unplugging threshold in the absence of vibrations.

Each simulation run was started with the droplet in a trapped position upstream of the constriction. This initial condition was obtained by placing the droplet far upstream of the constriction (so that it is not deformed) and by allowing it to become trapped under the condition of a static pressure gradient. Subsequently, the vibratory body force was added to the static pressure gradient and the droplet evolution was tracked. Simulations were carried both by fixing the vibration frequency and changing the vibration amplitude, as well as by fixing the acceleration amplitude and varying the vibration frequency.

#### **5.3.3.1. Acceleration amplitude effect**

Simulations were carried out at a constant frequency of 10 *Hz* and at several acceleration amplitudes in a relative total running time of 0.16 to the vibration period (0.1s), i.e. the ratio of total running time to the vibration period, 0.1s, is 0.16. Results are plotted in Figure 5.8, which shows the average bulk mass flow rate as a function of acceleration amplitude, and the unplugging acceleration amplitude as well. Similarly, two other series of

simulations were performed at constant frequencies of 20 Hz and 50 Hz. The flow rate plots for these simulations are presented in Figures 5.9 and 5.10, respectively.

These figures show the existence of a discrete unplugging acceleration amplitude for a fixed vibration frequency (approximately 125, 159, and 204  $m/s^2$  for the frequencies of 10, 20, and 50 Hz, respectively). Moreover, from the perspective of the total external force exerted on the fluids, the maximum total force needed to mobilize the trapped droplet here summing from the static pressure gradient and the observed unplugging value shown above (after converted to the same unit as the pressure gradient) is less than the unplugging external pressure gradient for the case described in section 5.3.2, which demonstrates one aspect of the efficiency of a vibration while a little longer time is needed to mobilize the trapped drop for the case with vibration.

Furthermore, in all cases with vibration, the average bulk mass flow rate increases when the acceleration amplitude increases, as anticipated from the capillary-physics mechanism described by Beresenev, *et al.* (2005), when the acceleration amplitude is higher than the unplugging threshold. However the increasing slope depends on both the vibration frequency and the length of running time. In general, the higher average mass flow will be achieved if the simulation is running longer due to the relative elongation of free flow in the downstream after the trapped drop passes through the most constricted part. Hence, a quicker increasing trend of flow rate will show up for a longer period run at a same vibration frequency. The comparison among frequencies under the same running time will be discussed later.

In addition, time percentage (the ratio of time length for the trapped droplet passing through the middle point of the capillary tube to one vibration period) as a function of acceleration amplitude is also reported in Figure 5.11 for those frequencies. It can be seen that as the acceleration amplitude increases, the time percentage declines at a same frequency. It also appears that as the frequency increases, the time percentage increases for a constant acceleration amplitude case (the amplitude must be greater than the unplugging values for all cases), which shows the vibration at a lower frequency is more efficient.

#### **5.3.3.2. Frequency effect**

The dependence of the average bulk mass flow rate on vibration frequency for fixed values of the acceleration amplitude is shown in Figure 5.12. The mass flow rate increases as the frequency declines at fixed vibration acceleration amplitude. Moreover, the lower the frequency, the more efficient the vibration is because a higher flow rate is observed as the frequency decreases for a fixed acceleration amplitude. Again, the positive dependence between flow rate and acceleration amplitude under a fixed frequency is consistent with the acceleration amplitude effect discussed before.

Moreover, as we pointed out in section 5.3.3.1, the time percentage (the ratio of time length for the trapped droplet passing through the middle point of the capillary tube to one vibration period) decreases as the frequency decreases (shown in Figure 5.11), which also illustrates that the vibration with a lower frequency is more effective. The reason is because the continuous effective unplugging time (the time length when the total forcing is greater the unplugging threshold) in one vibration period for a lower frequency case is longer than that for a higher frequency case since the vibration period for a lower frequency is longer than that for a higher frequency, although the proportion of effective unplugging time in one period is same, then it's helpful according to the physics capillary mechanism.

### **5.3.3.3. Mobilization threshold**

From the discussion above, we find that there is an unplugging threshold of acceleration amplitude for a fixed vibration frequency, below which no mobilization is observed and above which flow enhancement occurs. Generally we consider that mobilization occurs if the center of the trapped drop passes through the middle point of the constricted tube in a finite time. Under that assumption, repeated simulations were performed under different acceleration amplitudes with a fixed frequency in 1, 3, or 5 vibration cycles, until the critical acceleration amplitudes were found. Figure 5.13 shows the critical acceleration amplitudes as a function of frequency, and it can be seen that as the frequency increases, the critical acceleration amplitude increases in an approximately linear relationship in the lower frequency range (lower than 10 Hz) and with a slowly increased trend in the rest of the comparatively higher frequency region. These trends are similar to those reported by Graham and Higdon (2000b), although a dimensionless critical frequency and oscillatory

forcing were used in their work. The overall trend of critical acceleration amplitude as a function of frequency is similar for all running times, but the critical acceleration amplitude does not decrease as the length of running time decreases under a fixed vibration frequency. Moreover, the differences among the critical acceleration amplitudes for different running time are larger at a higher frequency than those at a lower frequency. Those differences are hard to discern in an extremely lower frequency range (lower than 10 *Hz*) while they are obvious in a higher frequency region. Furthermore, at fixed frequency, the difference of the critical acceleration amplitudes between 3 and 5 periods (running time) is not as large as the difference of the critical acceleration amplitude between 1 and 3 periods, although the running time differences are exactly the same. When the frequency is less than 10 *Hz*, the critical amplitude becomes independent of the number of vibration cycles. Therefore, increasing the running time is not helpful for mobilizing trapped droplets in the lower vibration frequency range (lower than 10 *Hz*), whereas it can decrease the critical acceleration amplitude in the higher frequency range (the longer the running time, the smaller decrease of the critical acceleration amplitude).

#### 5.3.3.4. Further discussion

Iassonov and Beresnev (2005) recently obtained a linear relationship between the required critical acceleration amplitude of the vibration,  $A_a$ , and the related frequency,  $f$ , for a trapped continuous ganglion occupying several adjacent pores, which means that the ratio  $A_a/f$  was a constant for ganglion unplugging. It implied that the wave intensity only, instead of the acceleration amplitude and the frequency of a wave, could be considered as the criterion of mobilization of trapped ganglia. Compared with the relationship we presented in Figure 5.13 above, the linear correlation between acceleration amplitude and frequency agrees well at very low frequencies (less than 10 *Hz*), but it deviates from this linearity at higher frequencies. This deviation may be a result of the fact that we consider droplets that occupy only a single pore and we run unsteady simulations in FLUENT, whereas Iassonov and Beresnev's analysis accounted for droplets occupying multiple pore bodies and a quasi-static approach is employed.

## 5.4. Summary

A series of CFD simulations were carried out using a commercial CFD package, FLUENT, to study the effects of vibratory body forces on droplet mobilization in a constricted capillary tube. An unplugging threshold, which depends on the characteristics of the whole system, is shown to exist. The droplet will be trapped if the total external force is less than the release threshold.

Adding a vibratory body force was shown to be helpful for mobilizing trapped droplets. For a fixed acceleration amplitude, the vibrations become more effective in mobilizing trapped droplets as the vibration frequency decreases from 50 Hz to 10 Hz. For fixed vibration frequency, the average bulk mass flow rate increases as the acceleration amplitude increases. These findings, which were calculated for realistic length pore sizes, are consistent with the predictions following from the capillary physics mechanism proposed by Beresnev *et al.* (2005) and with quasi two-dimensional micromodel experiments by Li *et al.* (2005). It was also shown that exposing trapped droplets to multiple vibration cycles may reduce the total force needed to mobilize trapped droplets when the vibration frequency is relatively high (~50-100 Hz). In contrast, for vibration frequencies less than approximately 10 Hz the release threshold does not decrease when exposing the droplet to multiple vibration cycles.

Although the CFD simulations reported here bolster the evidence for the validity of the capillary physics mechanism hypothesized by Beresnev *et al.* (2005), many further studies are needed before low-frequency elastic waves can be used predictably and reliably for field applications. For example, simulations must be undertaken using more realistic and complicated pore geometries and network connectivities to understand the interactions between multiple ganglia. Moreover many other aspects concerning vibratory stimulation of trapped droplets, such as its role in droplet coalescence and break up need further investigation.

## 5.5. Acknowledgements

This work was supported by the National Science Foundation award EAR-0125214 and the Department of Energy award DE-FC26-01BC15165. The authors would like to thank the anonymous reviewers for their helpful comments.

## 5.6. References

- Beresnev, I.A., Vigil, R.D., Li, W., Pennington, W.D., Turpening, R.M., Iassonov, P.P., and Ewing, R.P., (2005). Elastic waves push organic fluids from reservoir rock. *Geophysical Research Letter*. 32(13), L13303, doi:10.1029/2005GL023123.
- David, R.L., (1998-1999a). CRC Handbook of Chemistry and Physics, 79<sup>th</sup> ed., CRC Press, Washington, DC., pp.3-164.
- David, R.L., (1998-1999b). CRC Handbook of Chemistry and Physics, 79<sup>th</sup> ed., CRC Press, Washington, DC., pp.6-170.
- FLUENT Inc., (2003). FLUENT 6.1 User's Guide.
- Graham, D.R., and Higdon, J.J.L., (2000a). Oscillatory flow of droplets in capillary tubes. Part 1. Straight tubes. *Journal of Fluid Mechanics*, 425, 31-53.
- Graham, D.R., and Higdon, J.J.L., (2000b). Oscillatory flow of droplets in capillary tubes. Part 2. Constricted tubes. *Journal of Fluid Mechanics*, 425, 55-77.
- Iassonov, P.P., and Beresnev, I.A., (2005). Mobilization of entrapped organic fluids by elastic waves and vibrations. (submitted).
- Leyrat-Maurin, A., and Barther-Biesel, D., (1994). Motion of a deformable capsule through a hyperbolic constriction. *Journal of Fluid Mechanics*. 279, 135-163.
- Li, W., Vigil, R.D., Beresnev, I.A., Iassonov, P., and Ewing, R., (2005). Vibration-induced mobilization of trapped oil ganglia in porous media: Experimental validation of a capillary physics mechanism. *Journal of Colloid and Interface Science*, 289(1), 193-199.
- Weiss, G., (1986). Hazardous Chemicals Data Book, 2<sup>nd</sup> ed., Noyes Data Corporation, Park Ridge, NJ., pp.974.

## 5.7. Table and figure captions

Table 5.1. Meshing elements for three different meshes in the mesh sensitivity study.

Figure 5.1. Average flow rate as a function of the amplitude of vibratory forcing, showing the existence of both minimum-amplitude and maximum-frequency thresholds.

Frequency is the parameter of the curves.

Figure 5.2. Schematic of a convergence divergence channel (units:  $\mu\text{m}$ ).

Figure 5.3. A typical computational meshing for the channel.

Figure 5.4. The trapped drop profiles where the external pressure gradient is  $1300 \text{ Pa}$ , which is lower than the unplugging threshold, based on three different level meshes. (a) Mesh 1, (b) Mesh 2, and (c) Mesh 3 shown in Table 1.

Figure 5.5. The pressure profiles along the axis when the drops are trapped where the external pressure gradient is  $1300 \text{ Pa}$ , which is lower than the unplugging threshold, based on three different level meshes. (Red) Mesh 1, (Green) Mesh 2, (Black) Mesh 3 shown in Table 1.

Figure 5.6. The average bulk mass flow rate as a function of external pressure gradient as well as the unplugging external pressure gradient threshold.

Figure 5.7. Log of time percentage ( $\times$ ) when the center of the trapped drop passes through the middle point of the constricted tube, as well as the Log of time percentage ( $\square$ ) when the most right hand side of the drop passes through the outlet as a function of external pressure gradient, in a fixed total time period.

Figure 5.8. The average bulk mass flow rate as a function of acceleration amplitude. Conditions are frequency equals to  $10 \text{ Hz}$ , the relative total running time is 0.16 to a vibration period.

Figure 5.9. The average bulk mass flow rate as a function of acceleration amplitude. Conditions are frequency equals to  $20 \text{ Hz}$ , the relative total running time is 0.22 to a vibration period.

Figure 5.10. The average bulk mass flow rate as a function of acceleration amplitude. Conditions are frequency equals to  $50 \text{ Hz}$ , the relative total running time is 0.38 to a vibration period.

Figure 5.11. Log of time percentage when the center of the trapped drop passes through the middle point of the constricted tube as a function of acceleration amplitude for three distinguished frequency in a cycle. ( $\diamond$ ) 10 Hz, ( $\Delta$ ) 20 Hz, ( $\times$ ) 50 Hz .

Figure 5.12. The average bulk mass flow rate as a function of acceleration amplitude for five different frequencies in a relative total 0.16 running time to one vibration period at certain frequency. ( $*$ ) 10 Hz, ( $\times$ ) 20 Hz, ( $\Delta$ ) 32 Hz, ( $\square$ ) 40 Hz ( $\diamond$ ) 50 Hz.

Figure 5.13. Critical acceleration amplitude as a function of frequency for 1, 3, and 5 cycles running. ( $\times$ ) 1 cycle running, ( $\Delta$ ) 3 cycles running, ( $\square$ ) 5 cycles running.

Meshes	Axial nodes	Radial nodes
Mesh 1	111	31
Mesh 2	161	41
Mesh 3	321	81

Table 5.1

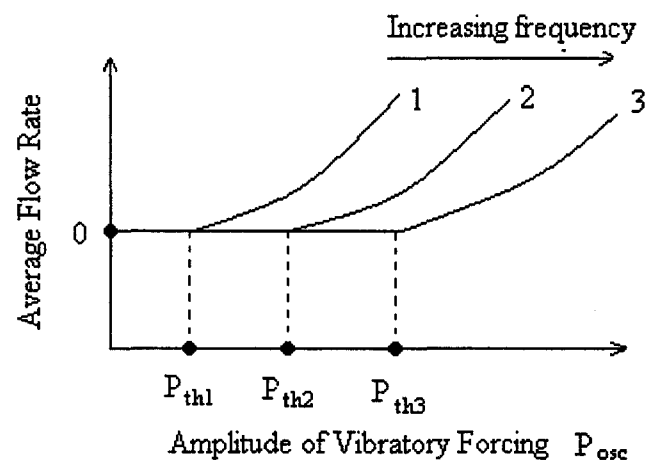


Figure 5.1

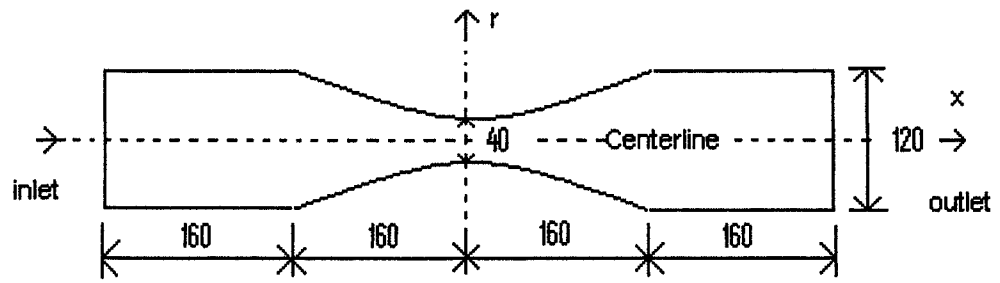


Figure 5.2

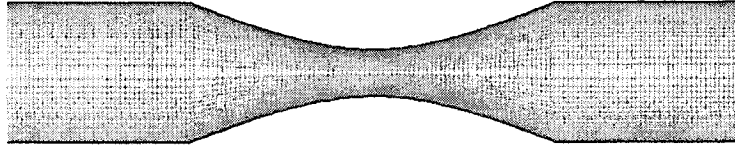


Figure 5.3

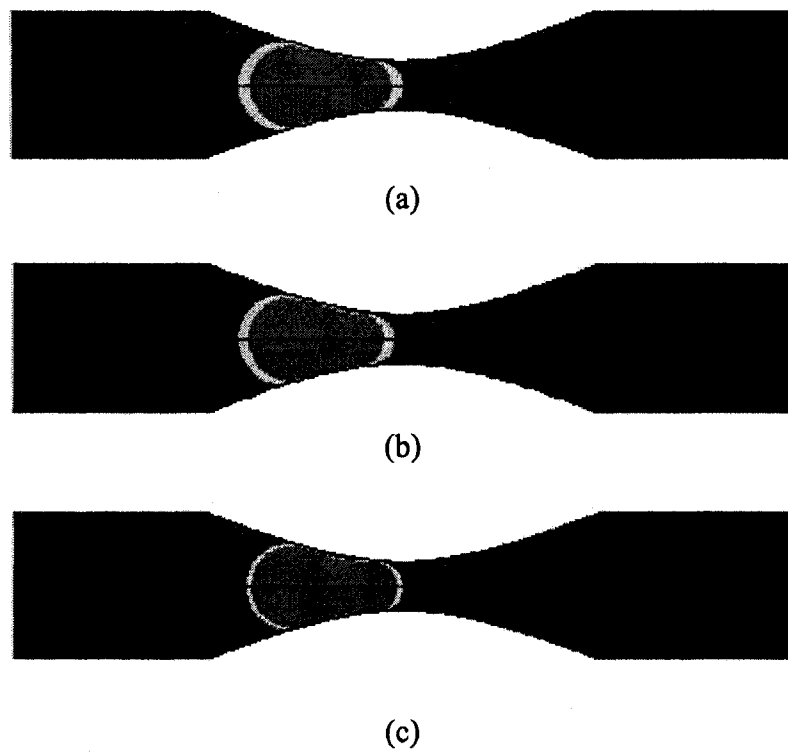


Figure 5.4

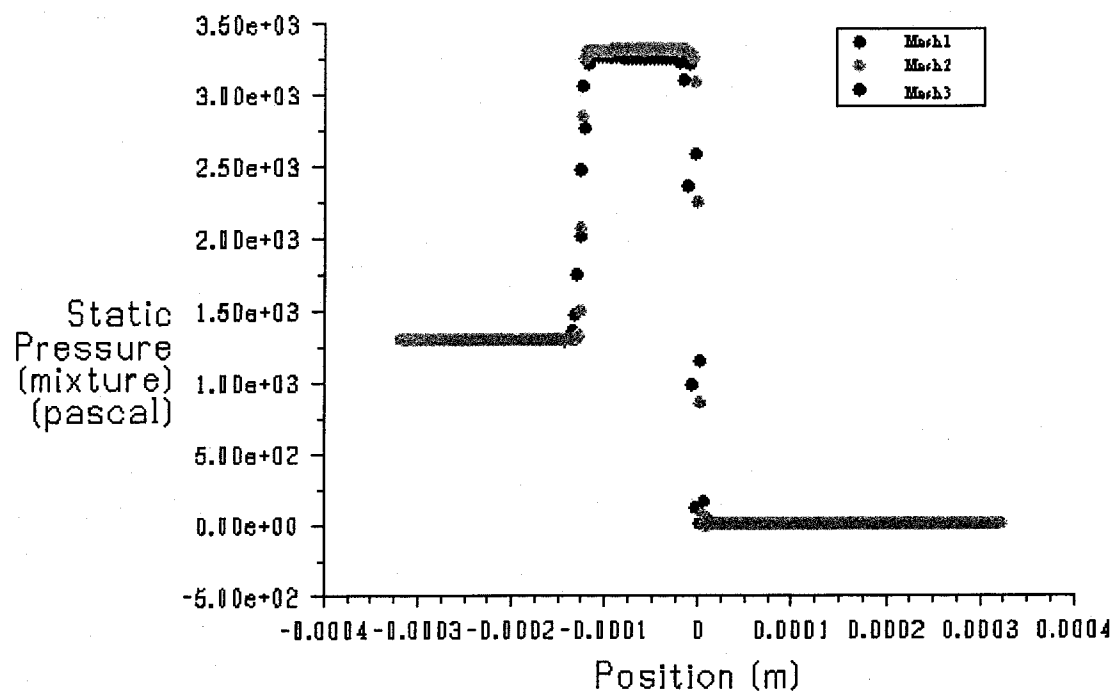


Figure 5.5

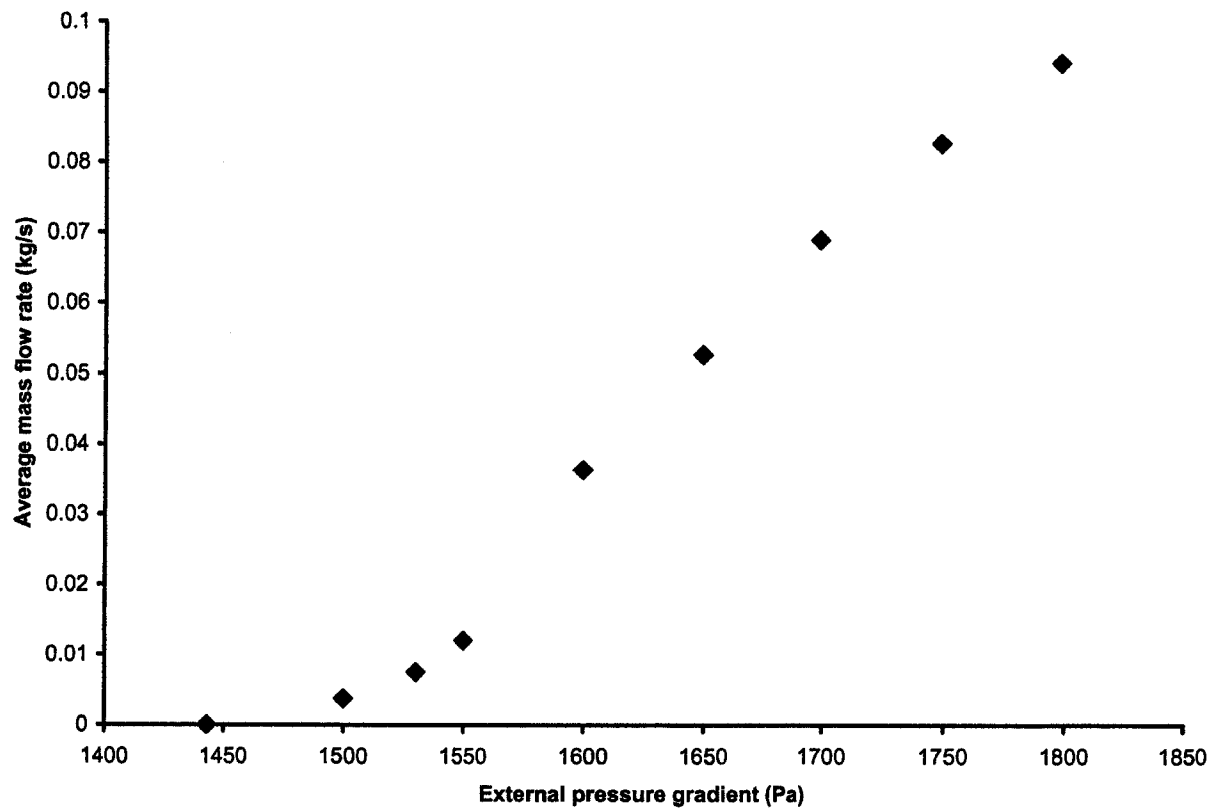


Figure 5.6

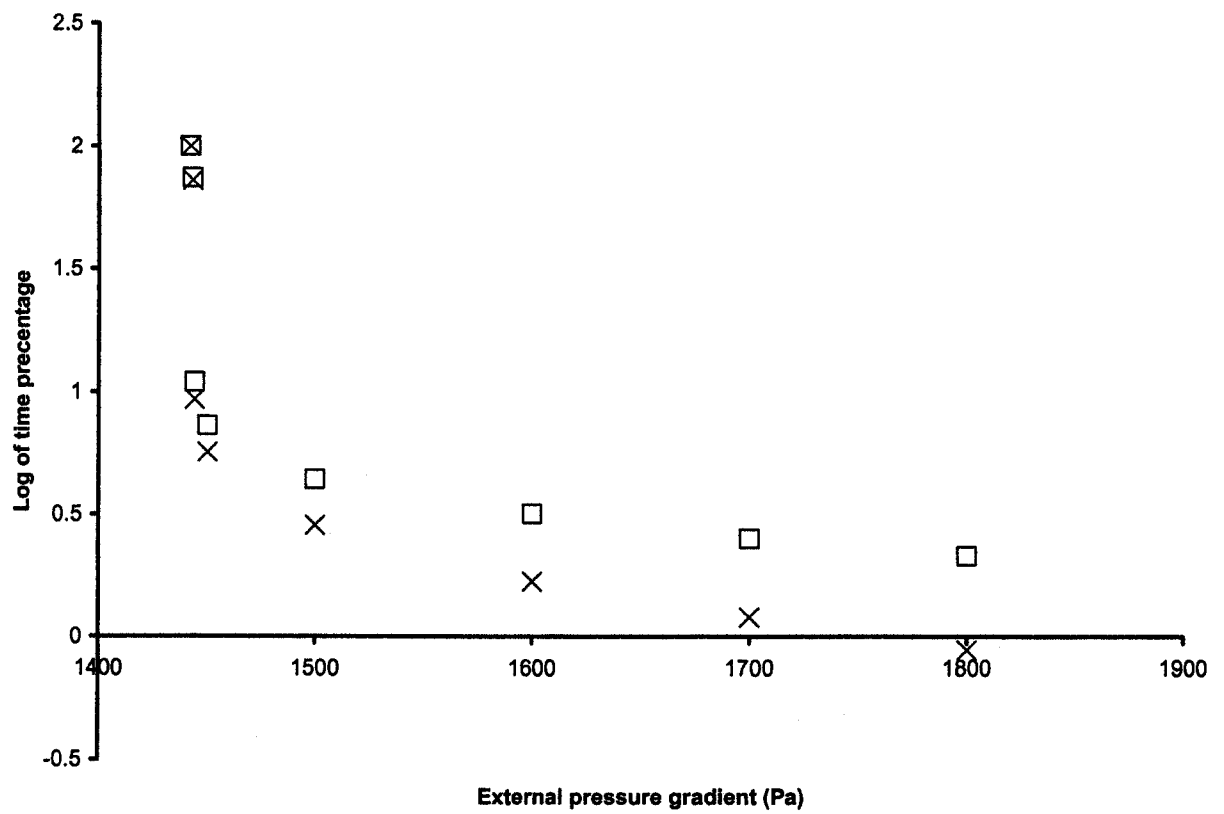


Figure 5.7

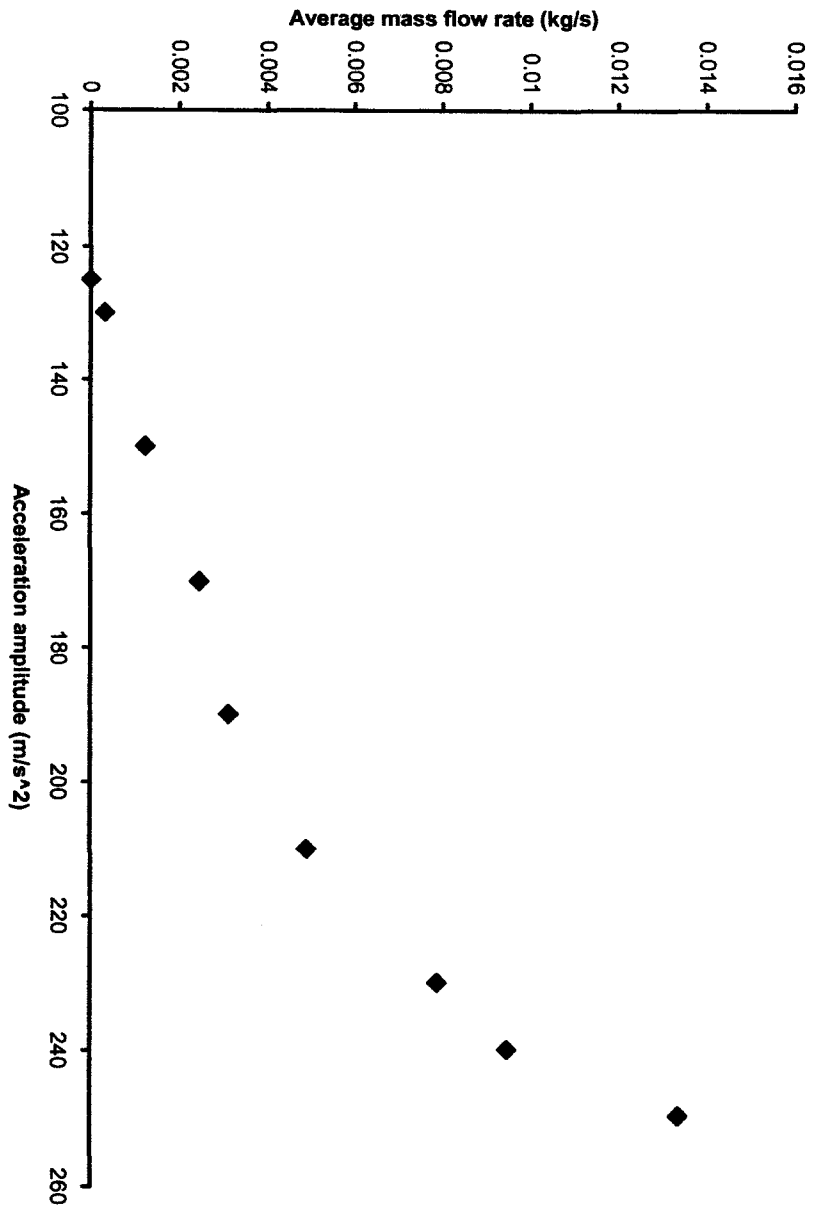


Figure 5.8

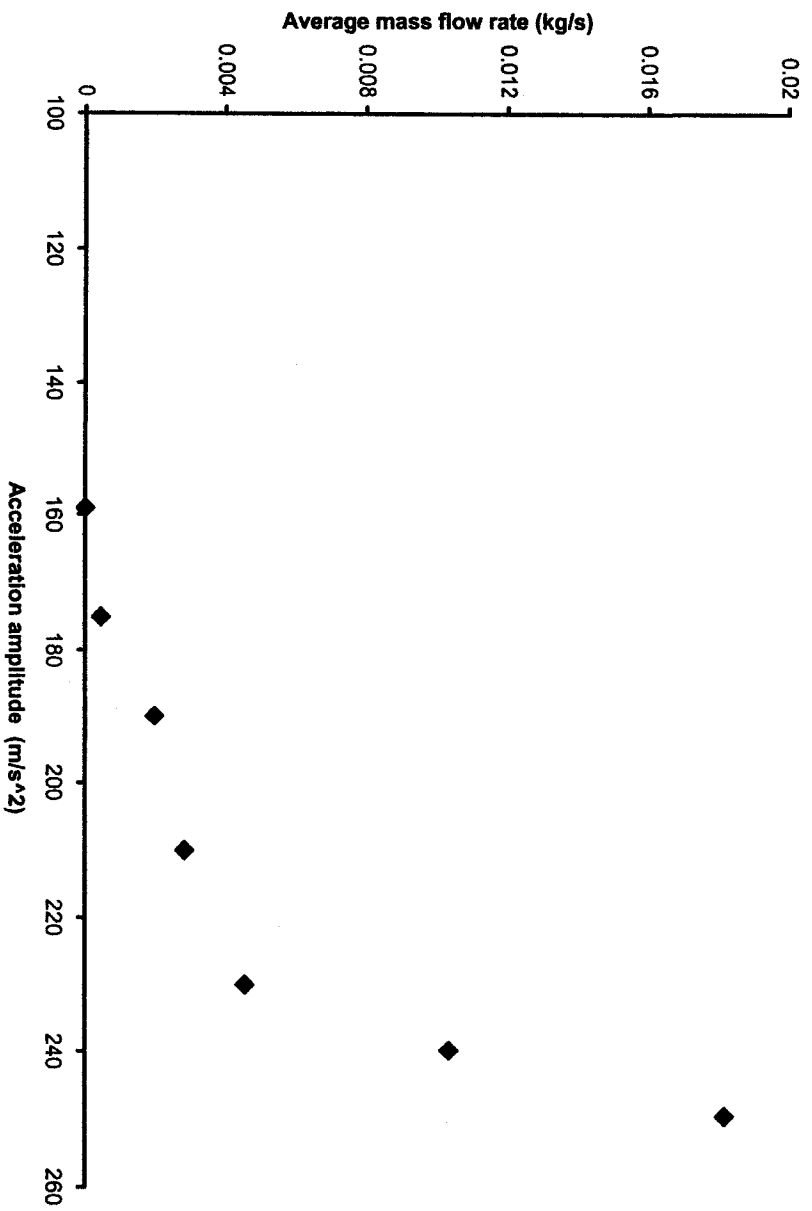


Figure 5.9

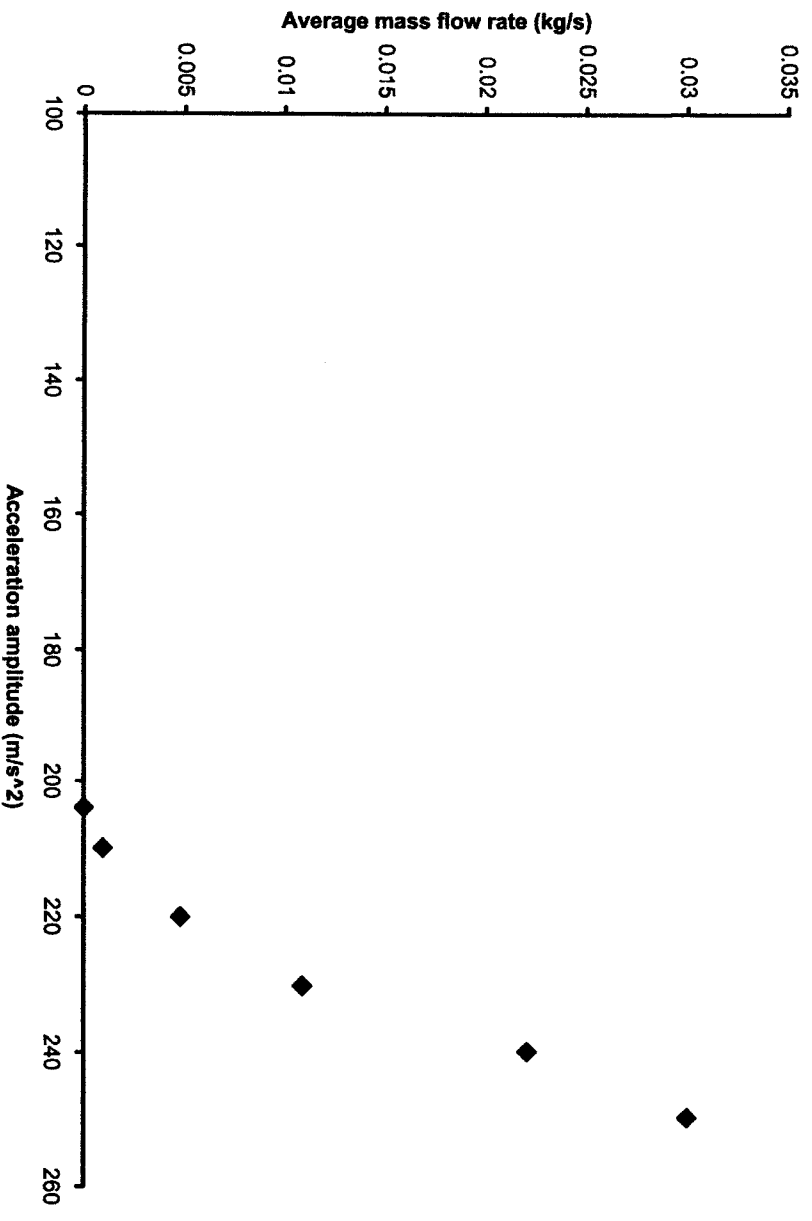


Figure 5.10

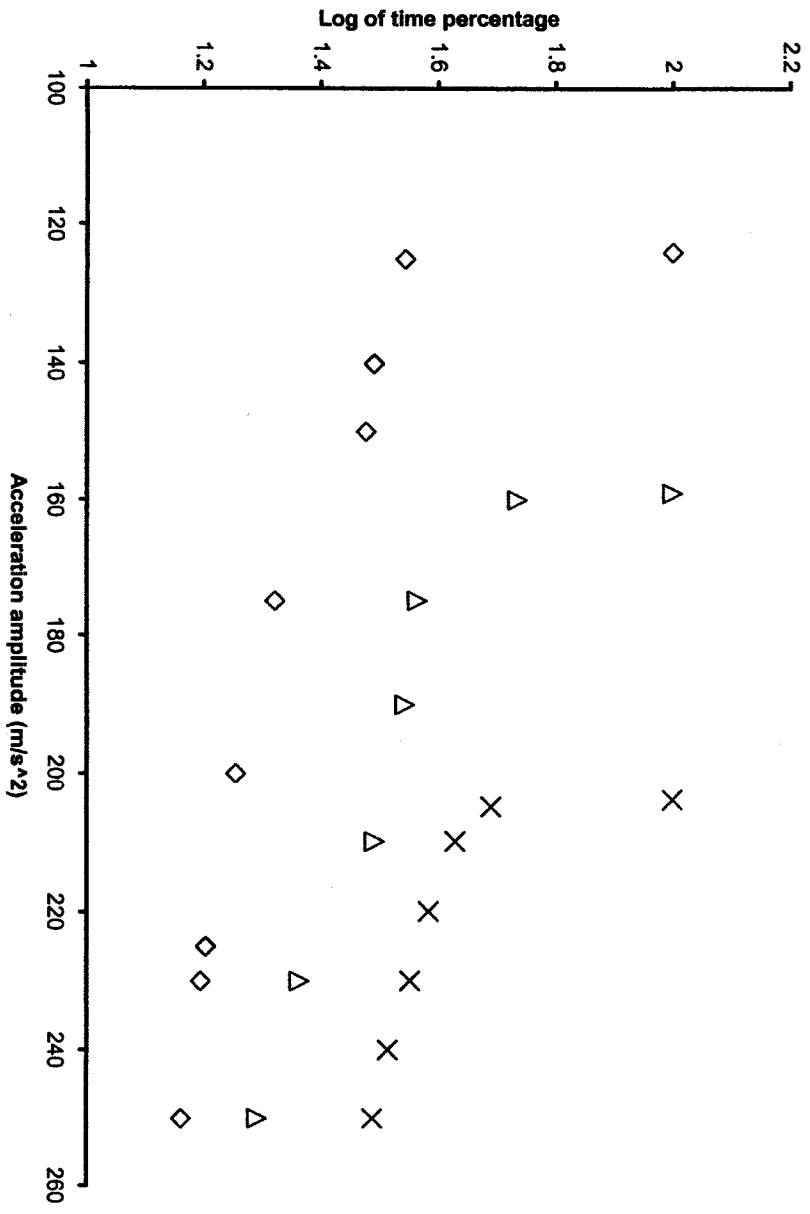


Figure 5.11

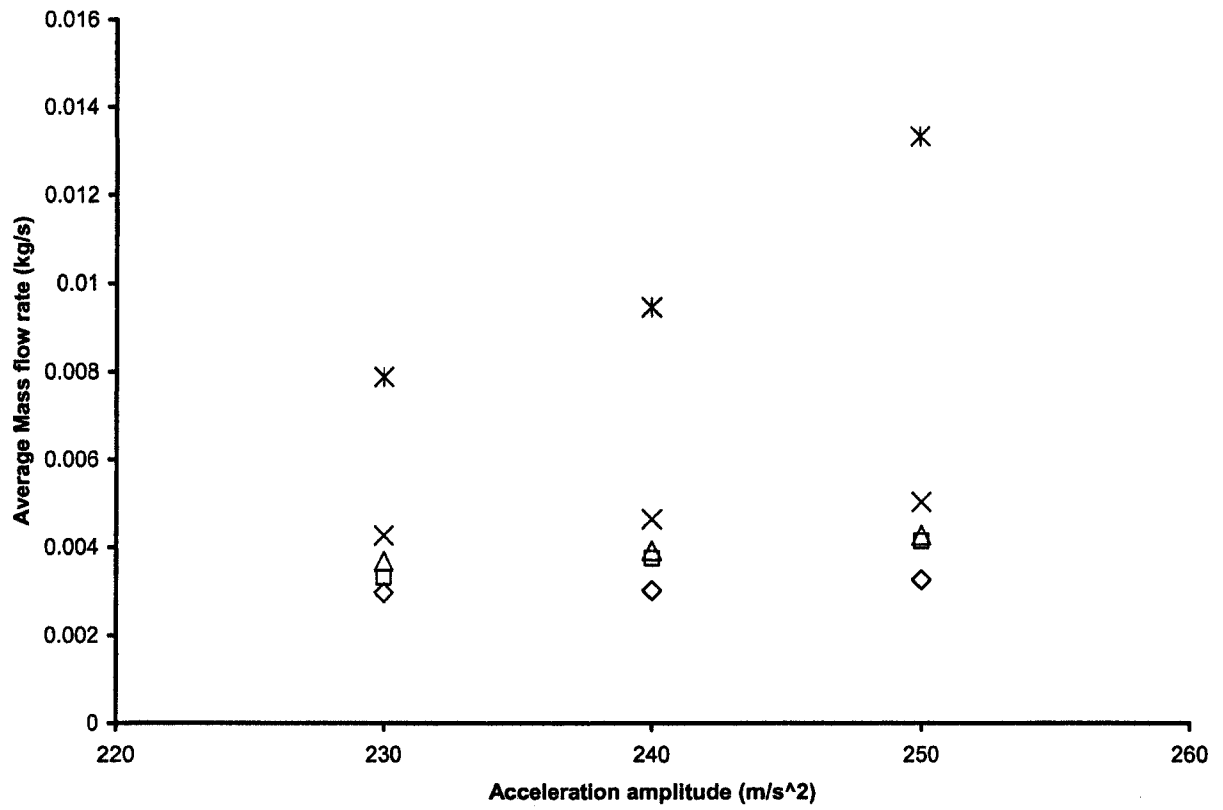


Figure 5.12

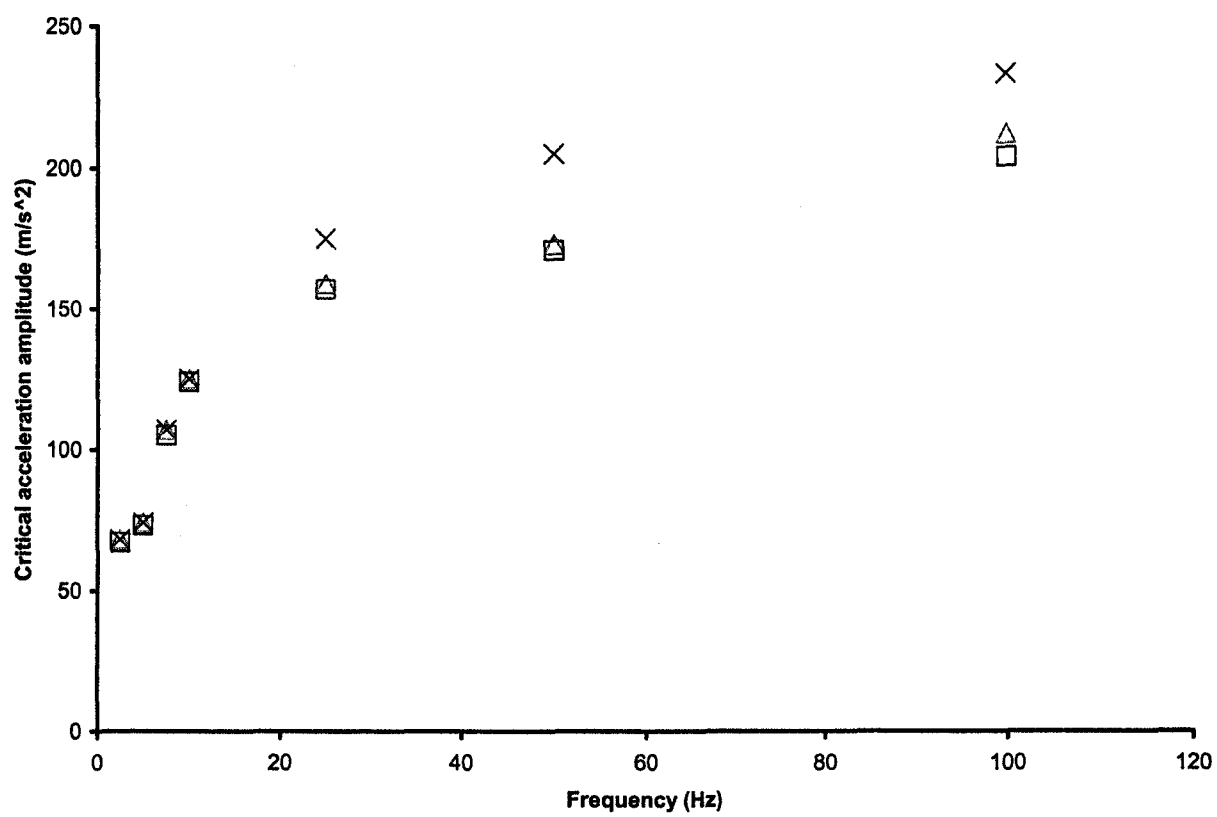


Figure 5.13

## CHAPTER 6. DROPLET BREAKUP DRIVEN BY INTERFACIAL TENSION IN CONSTRICTED CAPILLARY TUBES

Wenqing Li, R. Dennis Vigil, Igor A. Beresnev

A paper to be submitted to *Journal of Colloid and Interface Science*

### **Abstract**

Droplet deformation, breakup, and dynamics in constricted capillary channels are extensively studied in multiphase flow under external forces, as well as mechanism and dependence on physical parameters and properties. However, no quantitative relationship between occurrence of droplet breakup and characteristics of wavy-walls for capillary tubes was reported. In this study, a simple explicit criterion is derived to initiate droplet breakup in a sinusoidally constricted tube under the condition of no any external forces, which is validated by numerical calculations and some published data. In addition, dynamics of droplet breakup driven by interfacial tension is studied in terms of characteristics of tube, viscosity ratio, density ratio and interfacial tension.

### **Keywords**

Droplet, breakup, constricted capillary tubes, dynamics

## 6.1. Introduction

Elastic wave stimulation of drops and bubbles through constricted capillary tube has been extensively studied numerically and experimentally (Graham and Higdon, 2000a, 2000b; Li *et al.* 2005), and has been found to be an effective approach to mobilize trapped droplets or bubbles. However, in a constricted geometry, we are not sure if breakup or coalescence of individual drop can occur under specific physical and geometrical conditions, whether the performance can be affected by an elastic wave and how if the answer is positive, and how important do they contribute to mobilization of a trapped droplet and to its dynamics.

In a constricted capillary tube, breakup can be formulated under specific conditions as a hydrodynamic problem as the growth in the collar of suspend phase in the neck of the constriction until it totally separates the parts of the droplet on the left-hand side and the right-hand side of the neck. Numerous previous studies of droplet deformation, breakup, and dynamics were carried out by scientists.

Gauglitz and Radke (1990) employed an analytical approach to study the breakup of a gas bubble in which a nonlinear evolution equation for the collar's thickness was derived from the equations of momentum and the continuity equation to capture the entire evolution of a growing collar inside a constricted cylindrical capillary channel. The breakup took place when the thickness equaled to the radius of the neck. That was an approximation method because the assumption of small slope for constricted capillaries was made. But it still led to a good agreement with the experimental data for collar growth in constricted capillaries. However we are not sure if a similar approach can be applied to a system with a droplet suspended in a continuous phase and moving through a constriction. Also, the effect of an elastic wave such as vibration as an added time-dependent force has never been considered.

Tsai and Miksis (1994) reported a study of dynamics of a droplet in a constricted capillary tube driven by a pressure gradient, especially focused on the effect of the physical parameters such as the shape of the constriction, capillary number, and bubble size on the dynamics of the droplet. The inference of this study is that the snap-off is controlled by the trade-off between two opposite processes. On one hand, the higher the speed of the droplet,

the thicker is the collar of suspended phase in the constriction that causes the breakup because of elongation in the shape of the droplet, which facilitates breakup. On the other hand, a higher speed of the droplet also means a shorter residence time of the droplet in the constriction, which may prevent the breakup from developing. Oscillatory forcing was also not considered in the study.

Olgricht and Leal (1983) performed serials of experiments to investigate a pressure driven motion of immiscible drops through periodically varied diameter capillaries and obtained qualitative results for drop deformation and breakup, which demonstrated the relationship between capillary geometry and mobilization of drops. Furthermore, two distinct modes of drop breakup for small viscosity ratio drop and drop with viscosity equal to the suspended phase were reported and a conclusion was made that the extensional strength of the imposed flow contributed to the breakup of droplet.

Hemmat and Borhan (1996) focused on buoyance-driven motion of viscous drops and gas bubbles through a vertical capillary with periodic corrugations and carried a series of experiments to examine the role of capillary geometry on drop deformation and breakup over a wide range of the governing parameters such as drop size, viscosity, density, and Bond number. For a system with large enough drop size, sequential drop breakup was observed as long as the drop size was bigger than the critical drop size for the onset of drop breakup in a specific system. Moreover, the same mode of breakup was observed for systems with viscosity ratios of drop to continuous phase around 1. They suggested that the imposed flow and hydrodynamic interaction between drop and the capillary wall equally contributed to the drop deformation and breakup. "The role of the capillary geometry in determining the critical conditions for the onset of drop breakup warrants further investigation" (Hemmat and Borhan, 1996).

As for a study of dynamics, Gauglitz and Radke (1990) showed that time to breakup depended on several factors such as initial film profile, film thickness, pore geometry, fluid viscosity, and interfacial tension etc. It was shown that the film thickness at the neck of the constriction was crucial and the time to breakup was proportional to  $Ca^{-2}$ , where  $Ca$  is the capillary number.

In our study, we will mainly focus on the investigation of droplet breakup in a constricted capillary channel under the condition of no bulk flow and no any external forces. At first a theoretical criterion related to geometrical parameters is derived in order to initiate a droplet breakup. Then numerical simulations using a commercial CFD (Computational Fluid Dynamics) package are performed to validate the criterion, which is also verified by published data. In addition, dynamics of droplet breakup is studied to reveal the influence of geometry, viscosity ratio, density ratio, and interfacial tension, as well as some preliminary studies under the condition of external forces. The study will provide useful information to access effect of oscillatory forces on droplet breakup further in constricted capillary tubes.

## 6.2. Criterion to initiate droplet breakup

As shown in Figure 6.1, a big droplet (discrete phase  $\Phi_d$ ) is suspended in a continuous phase (phase  $\Phi_c$ ) in a sinusoidally constricted capillary tube, in which the axial variation in wall radius,  $R_w(z)$ , is described by the functional form  $R_w(z) = R_0 + A \sin(2\pi z / L)$ , where  $R_0 = (R_{w\max} + R_{w\min}) / 2$ ,  $A = (R_{w\max} - R_{w\min}) / 2$ ,  $L$  is the tube wavelength, and  $R_{w\max}$  and  $R_{w\min}$  are the maximum and minimum tube radii, respectively.

A film of phase  $\Phi_c$  with uniform thickness  $d$  is initialized between the droplet and the wall. Hence, the droplet has the same shape as the wall but with  $d$  smaller radius along the axial variation than the radius of the wall. Therefore, the droplet has wavelength  $L$ , maximum radius  $R_{\max} = R_{w\max} - d$  at locations such as point A, and minimum radius  $R_{\min} = R_{w\min} - d$  at locations such as point C.

According to Laplace equation, the pressure gradient across the interface at locations A and B could be written as  $\Delta P_{AB} = P_A - P_B = \sigma \left( \frac{1}{R_{\max}} + \frac{1}{R_g} \right)$ , and the pressure gradient across the interface at locations C and D could be written as

$\Delta P_{CD} = P_C - P_D = \sigma \left( \frac{1}{R_{\min}} - \frac{1}{R_g} \right)$ , where  $R_g$  is the radius of osculating circle for the interface

(equivalently the radius for the wall) at the location with minimal radius, and  $\sigma$  is the interfacial tension between the two immiscible phases. Under the assumption of uniform pressure in the film, the pressure gradient between locations C and A could be calculated by

$$\Delta P_{CA} = \Delta P_{CD} - \Delta P_{AB} = \sigma \left( \frac{1}{R_{\min}} - \frac{1}{R_{\max}} - \frac{2}{R_g} \right).$$

A positive pressure gradient  $\Delta P_{CA}$ , i.e.  $\frac{1}{R_{\min}} - \frac{1}{R_{\max}} - \frac{2}{R_g} > 0$ , will initiate a flow of phase

$\Phi_d$  in the droplet parallel to the direction from location C to location A, which will result in a narrower droplet at the throat of the tube and longer elongation of the droplet. The more positive the  $\Delta P_{CA}$ , the more helpful to start up the deformation of the droplet. Moreover, any change resulting in more positive value of  $\Delta P_{CA}$  such as decreasing  $R_{\min}$ , will facilitate a further extended elongation of the droplet. Finally a snap-off of the droplet could happen at the center of the throat if the deformation can continue and/or keep long enough.

For a sinusoidal wavy-wall, the relationship between the radius  $R_g$  and radii  $R_{\max}$

and  $R_{\min}$  can be described as  $R_g = \frac{L^2}{2\pi^2(R_{\max} - R_{\min})}$ . After substituting the relationship into

the criterion,  $\frac{1}{R_{\min}} - \frac{1}{R_{\max}} - \frac{2}{R_g} > 0$ , a simple form could be obtained,

$$L > 2\pi \sqrt{R_{\max} R_{\min}}, \quad (6.1)$$

which can be used to justify whether droplet snap-off can be initiated or not.

Notice that if the film thickness  $d$  is small compared with the radii of the geometry,  $R_{\max}$  is close to  $R_{w\max}$  and  $R_{\min}$  is close to  $R_{w\min}$ , therefore, the criterion is approximated by

$$L > 2\pi \sqrt{R_{w\max} R_{w\min}}.$$

Similarly, a criterion of  $L > \pi \sqrt{R_{w\max} R_{w\min}}$  could be derived in a special case of geometry with only one full cycle sinusoidal wavy-wall ( $R_{w\max}$  and  $R_{w\min}$  are maximum and

minimum radii of the wall, respectively) and straight walls upstream and downstream. For another special case, a straight tube with radius  $R$ , the criterion could be simplified as  $L > 2\pi R$ .

### 6.3. Problem formulation and numerical method

The dynamic of a big droplet filled with a suspended phase in a sinusoidally constricted capillary channel as shown in Figure 6.2(a) is simulated under the condition of no bulk flow and no any external forces (no gravitational body force, no external pressure gradient, and no oscillatory force). The tube consists of 6 complete cycles with total length  $0.72 \text{ mm}$ . The maximum and the minimum radii of the tube are  $0.03 \text{ mm}$  and  $0.01 \text{ mm}$ , respectively. Notice that the dimension of the tube is chosen closer to an on-site application.

A commercial CFD package, FLUENT, is chosen to run simulations and the VOF (Volume of Fluid) model is employed to simulate the simple immiscible two-phase flow. The governing equations including the volume fraction equation, the continuity equation, and the axial and radial momentum equations as shown in chapter 5 will be solved for the current two-dimensional axisymmetric pipe flow. During calculations, the energy equation is ignored because the change of energy and temperature isn't our concern. An incompressible flow is assumed and the flow is assumed irrotational. But an additional tangential stress term, due to the surface tension between the two fluids, is considered in the VOF model in the form of

$$S_{st} = \sigma \frac{\rho \kappa_1 \nabla \alpha_1}{(\rho_1 + \rho_2)/2}, \text{ where } \sigma \text{ is again the surface tension between the two phases;}$$

$$\kappa = \nabla \cdot \frac{n}{|n|}, \text{ which is the curvature; and } n = \nabla \alpha_q, \text{ which is the surface normal defined as the}$$

gradient of the volume fraction of the  $q$ th phase. A wall adhesion is integrated with the surface tension model by specifying the contact angle (thereby it results in the adjustment of the curvature of the surface near the wall through the specific calculations of unit normals near the wall, hence it adjusts the source terms due to surface tension).

A typical computational meshing is generated by the mesh generation package GAMBIT (version 2.2.30) and partially presented in Figure 6.2(b) and 6.2(c) for two pores

and one pore only, respectively. The meshing tends to cluster near the wavy-walls and is uniformly distributed on the axial direction.

In the study, water is used as the continuous phase but an oil phase with varying properties is used as the droplet. And basically viscosity and density for the oil phase are set to be equal to those for water in the simulations. No slip boundary conditions are set on the walls and the contact angle on the wall is set as  $180^\circ$ . The gauge pressure at the inlet and outlet are specified as  $0 Pa$  to guarantee zero external pressure gradient across the tube.

Following initializing simulations by setting all pressure, axial velocity, radial velocity, and bubble volume fraction values as zeros, a big droplet across two adjacent pores with a thin water film between the droplet and the walls are marked and patched symmetrically somewhere in the most upstream to set as the initial position of the oil drop (Figure 6.3(a)).

Exactly same algorithms as shown in chapter 5 are employed to do numerical calculations. Scaled residual convergence criteria of  $10^{-3}$  's are used after balancing available computational resources and accuracy requirements.

## **6.4. Results and discussion**

### **6.4.1. Mesh sensitivity study**

The accuracy of the computation is highly dependent on the number of grids of the meshing. The more refined computational meshing, the higher accurate solution can be achieved. In general there exists a threshold of the number of grids, beyond which the simulation results won't be improved much in terms of what we are interested in, hence not necessary.

To verify the accuracy of the numerical scheme, mesh sensitivity studies are conducted upon on three different meshes as shown in Table 6.1. Under the specific geometry shown in Figure 6.2 and described in section 6.3, same computational dynamics of breakup, measurement of time to breakup, and its dependence to parameters investigated in the study are observed for all the meshes. The only difference is that with the increasing of the number of grids droplet breakup with a thinner water film at the beginning between the

droplet and the wavy-walls could be observed, and a smoother interface by interpolation and more precise solution around the walls could be obtained. However, Mesh 2 is sufficient enough for the calculations in terms of accuracy and the objective of the study. Hence it is used extensively in the future to reduce computational cost.

#### 6.4.2. Validation of the criterion by simulations

Simulations in a series of tubes with different wavelength of a sinusoidally constricted wall as shown in Table 2 are performed. The column of breakup or not in Table 6.2 shows that the droplet breakup is observed in the tubes as long as the wavelength is bigger than  $0.1008 \text{ mm}$ , but breakup won't happen in the tubes with wavelength equal to or less than  $0.1008 \text{ mm}$ . The column of time to breakup in Table 6.2 shows the length of time from the beginning of the simulation to the time point when the droplet is separated into two smaller drops. Infinite time value means no breakup observed for the specific tubes in the entire simulations.

As it is shown that breakup of droplet is observed for the tubes with wavelength larger than  $0.1008 \text{ mm}$ , which is much closer and consistent to the cutoff, calculated from equation (6.1), for the specific tubes with fixed radii in the simulations because

$2\pi\sqrt{R_{\min}R_{\max}} = 2\pi\sqrt{(0.01-0.0025)\times(0.03-0.0025)} \approx 0.0902 \text{ mm}$  (a film of phase  $\Phi_c$  near the wall with uniform thickness  $0.0025 \text{ mm}$  is initialized over all the simulations since section 6.4.2).

Notice that there is discrepancy between the cutoff calculated from the criterion and the one observed from the simulation results, which is reasonable because the criterion is only applied for a static onset of droplet breakup. However, in the simulations, the entire process is wholly dynamic from the starting of deformation to droplet breakup, and the radii of the droplet change in the direction to decrease the pressure gradient  $\Delta P_{CA}$ , which deters the further development of deformation and hence increase the threshold to initiate a snap-off.

Another approximation to the cutoff can be calculated as  $2\pi\sqrt{0.01 \times 0.03} \approx 0.1088 \text{ mm}$  if the thickness of the thin water film is negligible, which is much closer to the cutoff observed from the simulations.

A typical evolution of droplet breakup in a sinusoidally constricted tube with wavelength of  $0.12 \text{ mm}$  is shown in Figure 6.3.

#### 6.4.3. Validation of the criterion by published data

In Hemmat and Borhan (1996) experiments, drop breakup was observed with large enough drop size. In the paper, a wavelength of the sinusoidal corrugation tube,  $L = 4 \text{ cm}$ , was reported. The minimum radius of the constricted section was  $R_{w\min} = 0.43 \text{ cm}$ , and the maximum radius of the constricted section was  $R_{w\max} = 0.57 \text{ cm}$ . So the critical wavelength was about  $2\pi\sqrt{R_{w\min}R_{w\max}} \approx 3.11 \text{ cm}$ , which was less than the used wavelength in the experiments. Therefore, drop breakup should be observed according to the criterion shown in equation (6.1), which is consistent with the experimental results.

Martinez and Udell (1988) performed a numerical study of axisymmetric creeping motion of drops through a periodically constricted tube but did not report any breakup. Now let's check the criterion again. In tube I, let  $R_{w\min} = R_t$ , then  $R_{w\max} = 1.8R_t$ , and wavelength was  $L = 3.33R_{w\max} \approx 5.99R_t$ , hence the critical wavelength was about

$$2\pi\sqrt{R_{w\min}R_{w\max}} \approx 8.43R_t, \text{ which was bigger than the used wavelength for the tube.}$$

Therefore, no drop breakup should be observed. Similarly, in tube II, let  $R_{w\min} = R_t$ , then  $R_{w\max} = 3R_t$ , and wavelength was  $L = 3.33R_{w\max} \approx 9.99R_t$ , hence the critical wavelength was about  $2\pi\sqrt{R_{w\min}R_{w\max}} \approx 10.88R_t$ , which was bigger than the used wavelength for the tube, too. Therefore, no drop breakup should be observed.

In all, the criterion for initiating droplet breakup shown in equation (6.1) can provide a good explanation to the observations of either drop breakup or without breakup shown in the publications.

#### 6.4.4. Dynamics study

First of all, the time to breakup versus wavelength of the tube is plotted in Figure 6.4, which illustrates that there exists a threshold for the wavelength of the wavy-walls to initiate droplet breakup. Only for a capillary tube with wavelength greater than the threshold,  $0.1008\text{ mm}$ , droplet breakup could be observed. In addition, as the wavelength increases the time to breakup decreases at the beginning and levels off very quickly. It could be explained that with wavelength  $L$  increasing, the radius  $R_g$  (shown in Figure 6.1) increases, then the pressure gradient  $\Delta P_{CA}$  (positive) in the droplet increases, which facilitates the droplet breakup. However, after the wavelength ascends a certain value, the decrease in the pressure gradient  $\Delta P_{CA}$  due to the increase of the radius  $R_g$  of the wavy-wall won't be important again compared with the other terms in the expression of the pressure gradient  $\Delta P_{CA}$ . Therefore, no more effect on the time to breakup is observed.

We now study the effect of viscosity ratio between the droplet and the continuous phase. In Figure 6.5, we show that the time to breakup versus viscosity ratio in a sinusoidal tube with wavelength of  $0.12\text{ mm}$ , which is greater than the threshold to initiate droplet breakup. We see that the time to breakup increases as the viscosity ratio increases, and the relationship is very close to a linear trend in the reasonable range of viscosity ratio from 0.1 to 10, which is consistent with the basic theory about the effect of viscosity, the more viscous the droplet, the less vulnerable to breakup.

The effect of density ratio is also studied in the same geometry as the one for the study of the effect of viscosity ratio. The time to breakup versus density ratio is shown in Figure 6.6, which demonstrates that the effect of density ratio is ignorable in the current studying range. The result is expectable because no any external forces are exerted on the system, hence density won't affect the process much.

The dependence of the snap-off dynamics on the interfacial tension is shown in Figure 6.7 (the simulations are carried out in the same tubes as the ones used in the studies of the other effects). The plot illustrates that the time to breakup decreases in the beginning then levels off when the interfacial tension increases. For a droplet breakup driven by interfacial tension only higher interfacial tension will fasten the deformation of droplet, hence will reduce the time to occurrence of droplet breakup.

## **6.4.5. Further discussion and future work**

### **6.4.5.1. Breakup of a longer droplet across multiple adjacent pores**

In the same geometry as the tube used to study the effects of viscosity ratio, density ratio, and interfacial tension (with wavelength of  $0.12\text{mm}$ ), a much longer droplet across almost four adjacent pores and throats is initialized at the beginning and the dynamic snapshots are shown in Figure 6.8, which shows that a series of smaller droplets are created finally. In addition, the time to breakup is about  $82\ \mu\text{s}$ , same as the case for a shorter initial droplet across two adjacent pores (shown in Table 6.2). Another exactly same simulation is performed in a tube with the wavelength of  $0.10\text{mm}$ , but no breakup is observed. The results are consistent with the discussion before.

### **6.4.5.2. Breakup under external pressure gradient and/or oscillatory force**

Based on the case (shown in Figure 6.3(q)) where a big droplet is breakup into two smaller droplets under the condition of no any external forces, an external pressure gradient of  $6000\ \text{Pa}$  is exerted between the inlet and the outlet of the tube. The dynamic snapshots are listed in Figure 6.9, which shows that there are further droplet deformation, coalescence, breakup as the droplets pass through consecutive pores in the capillary tube. The droplets will be pushed out of the tube finally if the simulation is running long enough.

In another case, an external pressure gradient of  $2000\ \text{Pa}$  rather than  $6000\ \text{Pa}$  is exerted. The dynamic snapshots are illustrated in Figure 6.10, which demonstrates that the smaller droplets are trapped in the capillary tube under the smaller pressure gradient. If an appropriately additional oscillatory force is overlapped on the trapped droplets, mobilization of the droplets could be expected.

Moreover, study of droplet breakup in a constricted capillary tube is performed overlapping an external pressure gradient of  $2000\ \text{Pa}$  from the early beginning of the simulation and the evolution is shown in Figure 6.11, which shows a different steady state for the smaller droplets between this simultaneously overlapping case and the case where breakup occurs first under no external forces then an external pressure gradient is exerted. In this simultaneously overlapping case, the upstream smaller droplet is trapped while the

downstream smaller droplet is floating in the center of the next adjacent pore after breakup. However, for the other sequential case, both the two smaller droplets are found trapped. But, for both cases, breakup of initially big droplet is observed and the smaller droplet(s) are found trapped under the conditions of the smaller pressure gradient.

In addition, for the case where smaller droplets are trapped in the capillary tube study of system under an elastic wave such as vibration can be carried out to validate and investigate mobilization effect of elastic wave.

#### **6.4.5.3. Full parameter investigation of dynamics for breakup**

In practice occurrence of droplet breakup will not only depend on the shape of the constriction and physical properties such as viscosity ratio, density ratio (not much influence of density ratio is observed in the study but it may play a role if the system is under the functioning of external forces), and interfacial tension etc., but also depend on some other factors, such as thickness of the film around the wall which is affected by the capillary number somehow (in general the smaller capillary number the thinner film), distribution of thickness of the film which changes the effective radii of the droplet and influences occurrence of breakup, and resident time on which breakup is allowed to occur. Generally speaking, thicker film near the wall and longer resident time favor droplet breakup.

#### **6.4.5.4. Breakup under the condition of no film near the wall**

So far, only the case with film between the wall and the droplet is studied. For a case without film near the wall, no droplet breakup was observed by simulations in a sinusoidally constricted tube whatever we change the wavelength, the size of the droplet, and the physical properties. However, exerting an appropriate oscillatory force may help to create further droplet deformation and lead to breakup finally because it was already shown that an appropriate oscillatory force was much effective to mobilize a trapped ganglion.

#### **6.4.5.5. Size distribution of resulting smaller droplets after breakup**

It is also very interesting to figure out a size distribution of resulting smaller droplets for an originally big drop, which will help to build a model to describe the characteristics of

the smaller droplets, hence to explain the effects of factors causing breakup, and will be useful for a further study of cases involving intensive droplet breakup such as emulsion.

#### **6.4.5.6. Droplet breakup moving through consecutive constrictions**

Droplet deformation is a very complex process and it may behave differently in each cycle when it passes through successive constrictions. Effects of important factors, especially configuration parameters, should be investigated to see their separate and accumulative functioning.

#### **6.4.5.7. Verification by experiments**

All the inferences should be contrasted with experimental results to verify their limits of applicability if possible.

### **6.5. Summary**

In the study, a simple explicit criterion is derived to initiate droplet breakup in a sinusoidally constricted tube under the condition of no external forces, which is validated by numerical calculations and some published data.

In addition, dynamics of droplet breakup driven by interfacial tension is also studied on the characteristics of a tube, viscosity ratio, density ratio and interfacial tension. A slowly varying constriction (equivalently a flatter constriction or a longer wavelength of the constriction) results in a shorter time to breakup. A higher viscosity ratio increases the time to breakup, but a higher interfacial tension decreases the time to breakup. The effect of breakup dynamic on density ratio is ignorable. In all, the dynamics in the study is strongly dependent on the shape of the constriction, viscosity ratio, and interfacial tension, but not on density ratio.

Finally, some preliminary studies about the effects on droplet breakup of overlapping external forces such as external pressure gradient are performed. Further investigations are worthy to do on how these external forces including oscillatory force affect droplet breakup and facilitate droplet flow.

## 6.6. References

- Gauglitz, P.A., and Radke, C.J., (1990). The dynamics of liquid film breakup in constricted cylindrical capillaries. *Journal of Colloid and Interface Science*, 134(1), 14-40.
- Graham, D.R., and Higdon, J.J.L., (2000a). Oscillatory flow of droplets in capillary tubes. Part 1. Straight tubes. *Journal of Fluid Mechanics*, 425, 31-53.
- Graham, D.R., and Higdon, J.J.L., (2000b). Oscillatory flow of droplets in capillary tubes. Part 2. Constricted tubes. *Journal of Fluid Mechanics*, 425, 55-77.
- Hemmat, M., and Borhan, A., (1996). Buoyancy-driven motion of drops and bubbles in a periodically constricted capillary. *Chemical Engineering Communications*, Vol. 148-150, 363-384.
- Li, W., Vigil, R.D., Beresnev, I.A., Iassonov, P., and Ewing, R., (2005). Vibration-Induced Mobilization of Trapped Oil Ganglia in Porous Media: Experimental Validation of a Capillary Physics Mechanism. *Journal of Colloid and Interface Science*, 289:193.
- Martinez, M.J., and Udell, K.S., (1988). Axisymmetric creeping motion of drops through a periodically constricted tube. *AIP Conference Proceedings 197, "Drops and Bubbles"*, 222-234.
- Olgricht, W.L., and Leal, L.G., (1983). The creeping motion of immiscible drops through a converging/diverging tube. *Journal of fluid mechanics*. 134, 329-355.
- Tsai, T.M., and Miksis, M.J., (1994). Dynamics of a drop in a constricted capillary tube. *Journal of Fluid Mechanics*, 274, 197-217.

## 6.7. Table and figure captions

Table 6.1. Meshing elements for three different meshes in the mesh sensitivity study.

Table 6.2. Time to breakup for tubes with different wavelengths.

Figure 6.1. The mechanism of droplet breakup in a constricted tube.

Figure 6.2. (a) Schematic of a sinusoidally constricted capillary tube. (b), (c) a typical computational meshing for two pores and one pore only, respectively.

Figure 6.3. Computational fluid dynamics simulation of big droplet breakup in a constricted capillary tube with wavelength of  $0.12\text{mm}$ , bigger than the cutoff, at time points of (a) 0, (b) 5, (c) 25, (d) 50, (e) 75, (f) 100, (g) 125, (h) 150, (i) 300, (j) 450, (k) 750, (l) 1050, (m) 1550, (n) 2050, (o) 3050, (p) 4050, and (q)  $4250\ \mu\text{s}$ .

Figure 6.4. Time to droplet breakup versus wavelength of the tube.

Figure 6.5. Time to breakup versus viscosity ratio.

Figure 6.6. Time to breakup versus density ratio.

Figure 6.7. Time to breakup versus interfacial tension.

Figure 6.8. Computational fluid dynamics simulation of a longer droplet across four adjacent pores in a constricted capillary tube with wavelength of  $0.12\text{mm}$ , bigger than the cutoff, at time points of (a) 0, (b) 5, (c) 35, (d) 75, (e) 80, (f) 85, (g) 90, (h) 1000, (i) 2000, (j) 3000, (k) 4000, and (l)  $5000\ \mu\text{s}$ .

Figure 6.9. Evolution of smaller droplets (as shown in Figure 6.3(q) after big droplet breakup) in a constricted capillary tube with wavelength of  $0.12\text{mm}$  under external pressure gradient of  $6000\ \text{Pa}$  at time points of (a) 4400, (b) 4800, ..., (av)  $23200\ \mu\text{s}$  (with a increment of  $400\ \mu\text{s}$ ).

Figure 6.10. Evolution of smaller droplets (as shown in Figure 6.3(q) after big droplet breakup) in a constricted capillary tube with wavelength of  $0.12\text{mm}$  under external pressure gradient of  $2000\ \text{Pa}$  at time points of (a) 4250, (b) 4300, (c) 4350, (d) 4400, (e) 4450, (f) 4500, (g) 4550, (h) 5000, (i) 9200, (j) 14200, (k) 19200, and (l)  $24000\ \mu\text{s}$ .

Figure 6.11. Evolution of big droplet breakup in a constricted capillary tube with wavelength of  $0.12\text{mm}$  overlapping an external pressure gradient of  $2000\ \text{Pa}$  from the beginning at time points of (a) 0, (b) 50, (c) 100, (d) 150, (e) 300, (f) 450, (g) 750, (h) 1050, (i) 1550, (j) 2050, (k) 3050, (l) 4050, (m) 4250, (n) 4450, (o) 5000, (p) 9200, (q) 14200, (r) 19200, and (s)  $24000\ \mu\text{s}$ .

<b>Meshes</b>	<b>Axial nodes</b>	<b>Radial nodes</b>
<b>Mesh 1</b>	<b>481</b>	<b>17</b>
<b>Mesh 2</b>	<b>481</b>	<b>65</b>
<b>Mesh 3</b>	<b>1921</b>	<b>129</b>

Table 6.1

Wavelength ( <i>mm</i> )	Breakup or not	Time to breakup ( $\mu s$ )
0.1600	Yes	82.00
0.1520	Yes	79.50
0.1440	Yes	83.50
0.1360	Yes	92.00
0.1280	Yes	92.40
0.1200	Yes	82.00
0.1120	Yes	90.50
0.1080	Yes	89.00
0.1056	Yes	110.40
0.1040	Yes	164.80
0.1024	Yes	192.20
0.1016	Yes	396.80
0.1008	No	Infinite
0.1000	No	Infinite
0.0984	No	Infinite
0.0960	No	Infinite
0.0920	No	Infinite
0.0902	No	Infinite
0.0890	No	Infinite

Table 6.2

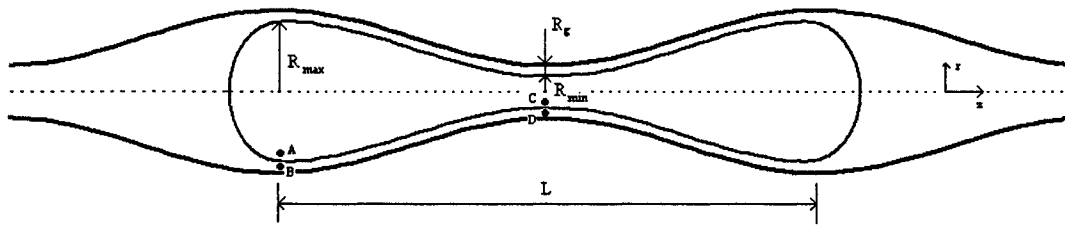
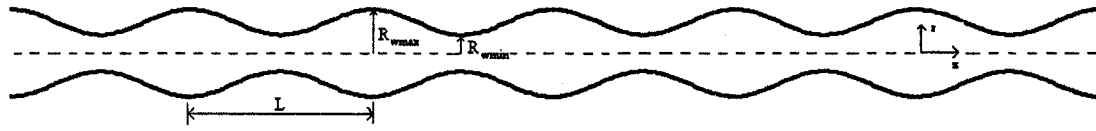
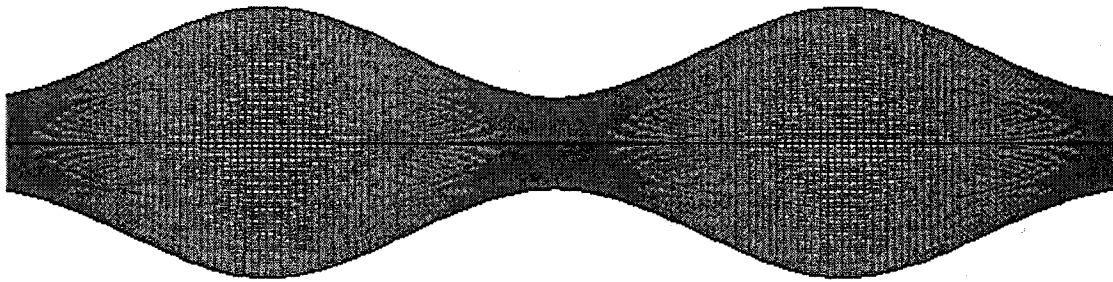


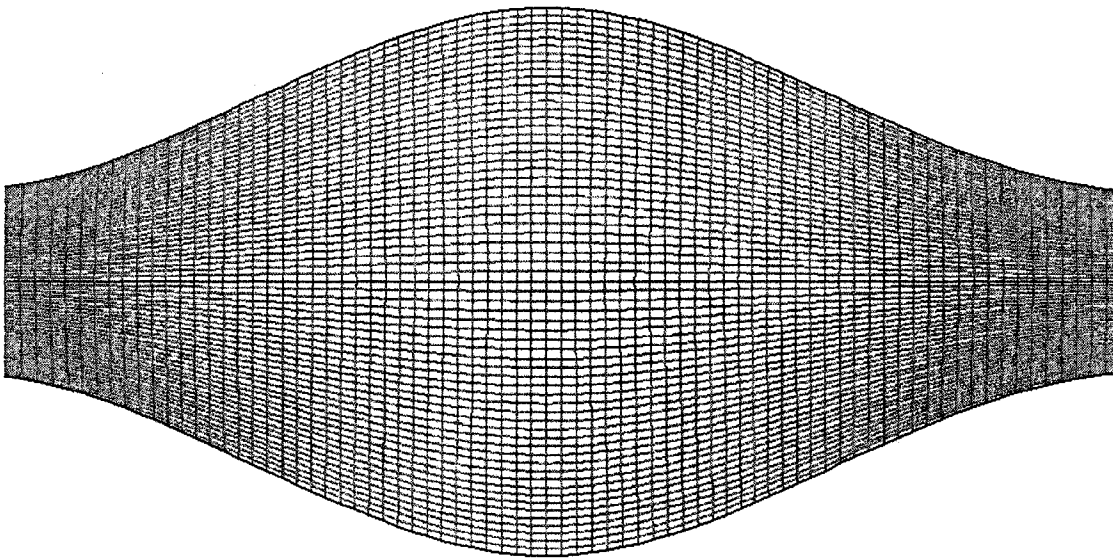
Figure 6.1



(a)

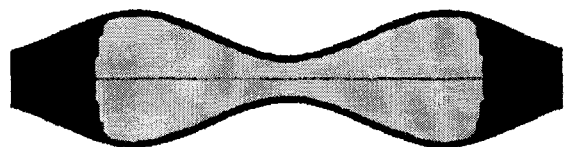


(b)

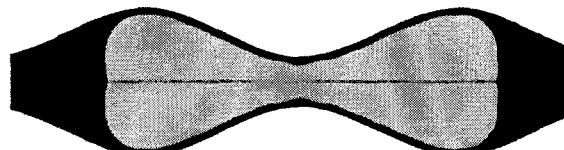


(c)

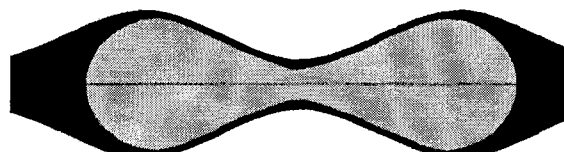
Figure 6.2



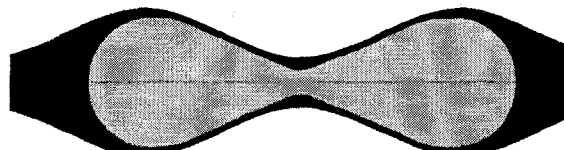
(a)



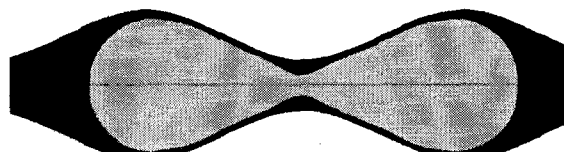
(b)



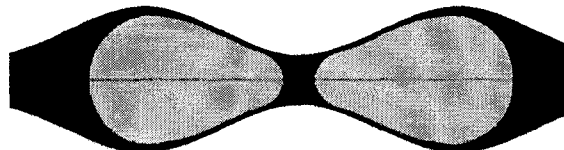
(c)



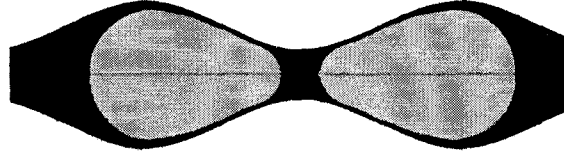
(d)



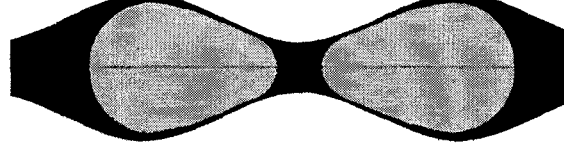
(e)



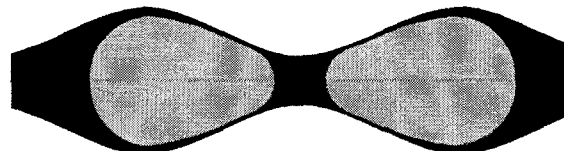
(f)



(g)



(h)



(i)

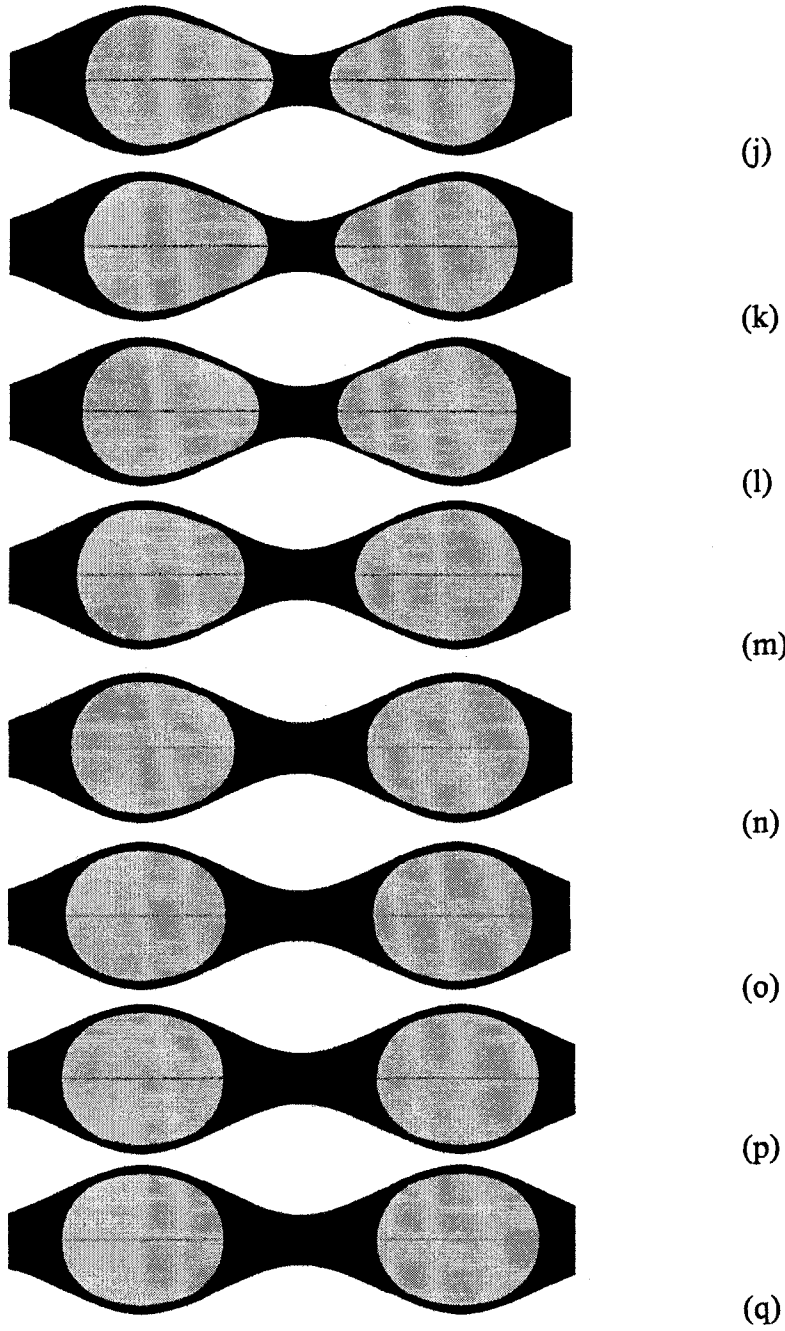


Figure 6.3

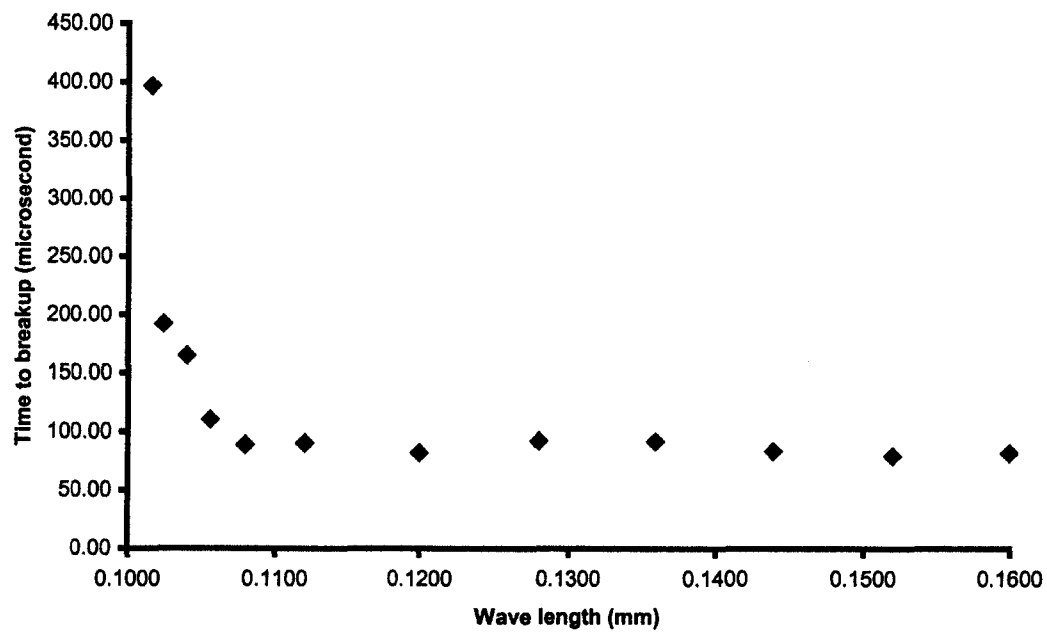


Figure 6.4

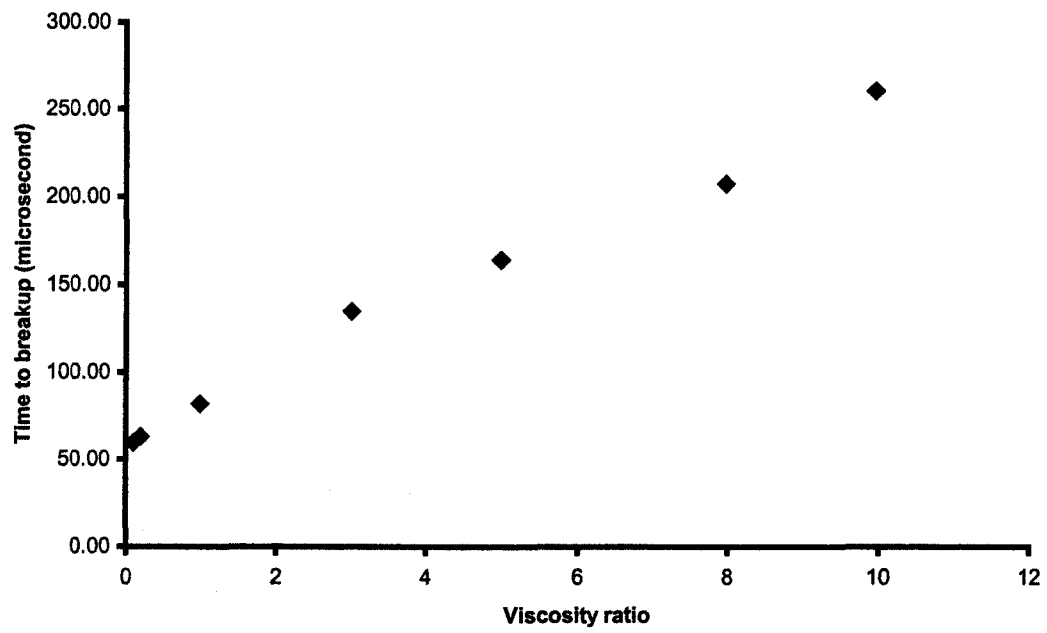


Figure 6.5

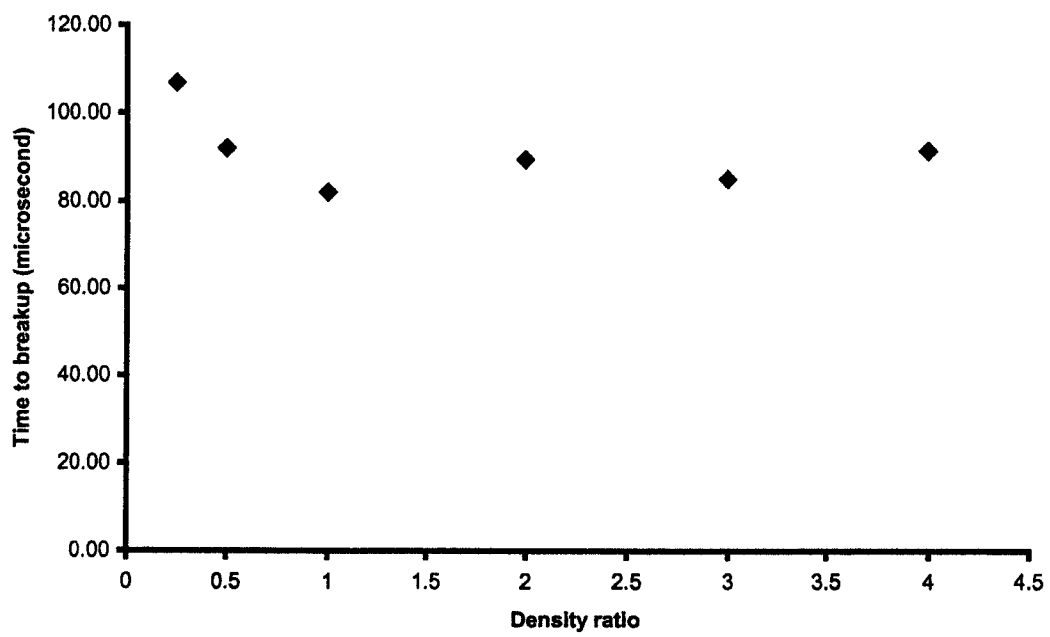


Figure 6.6

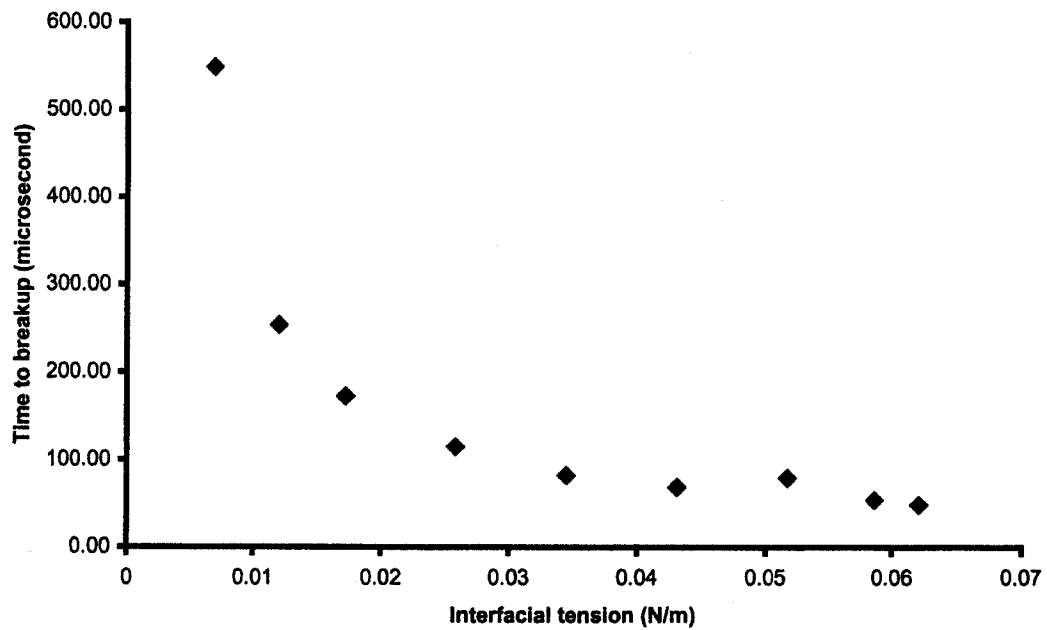


Figure 6.7

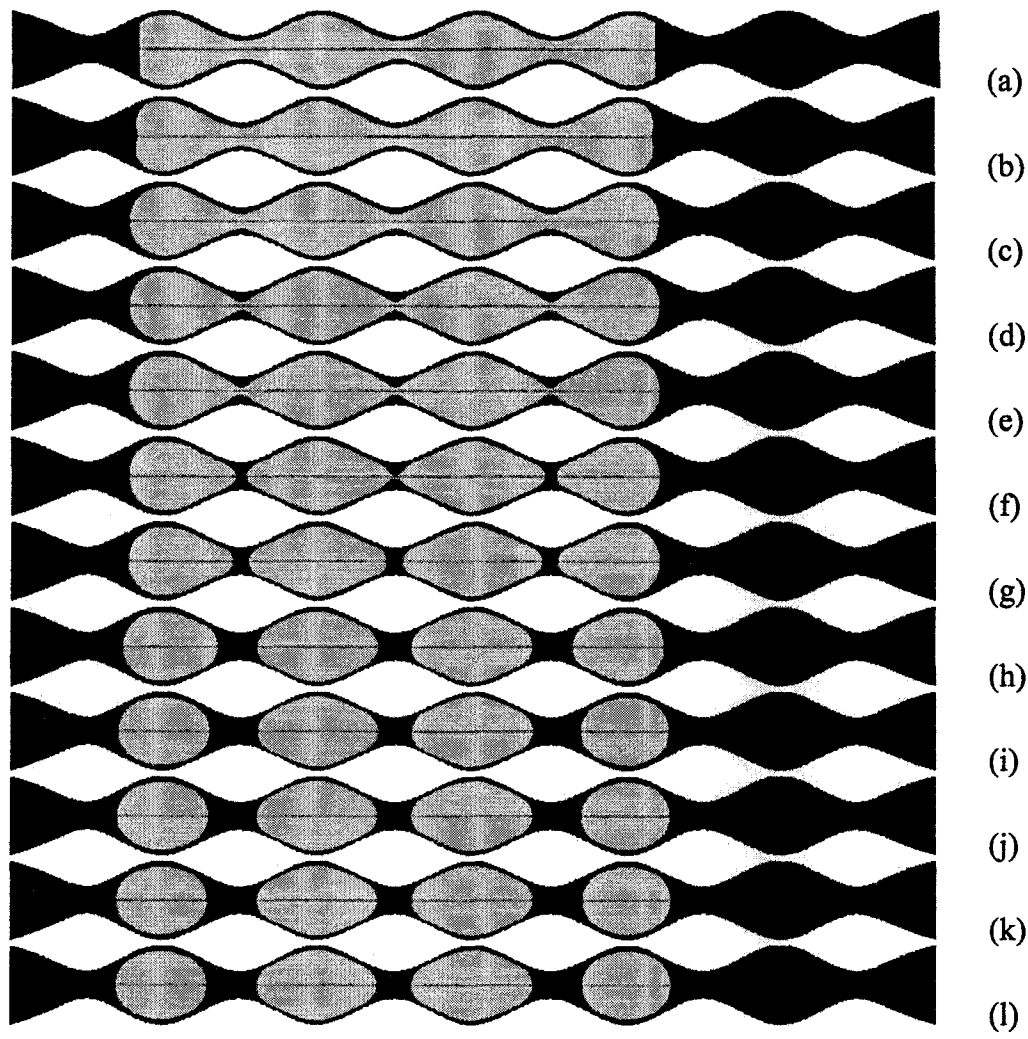


Figure 6.8

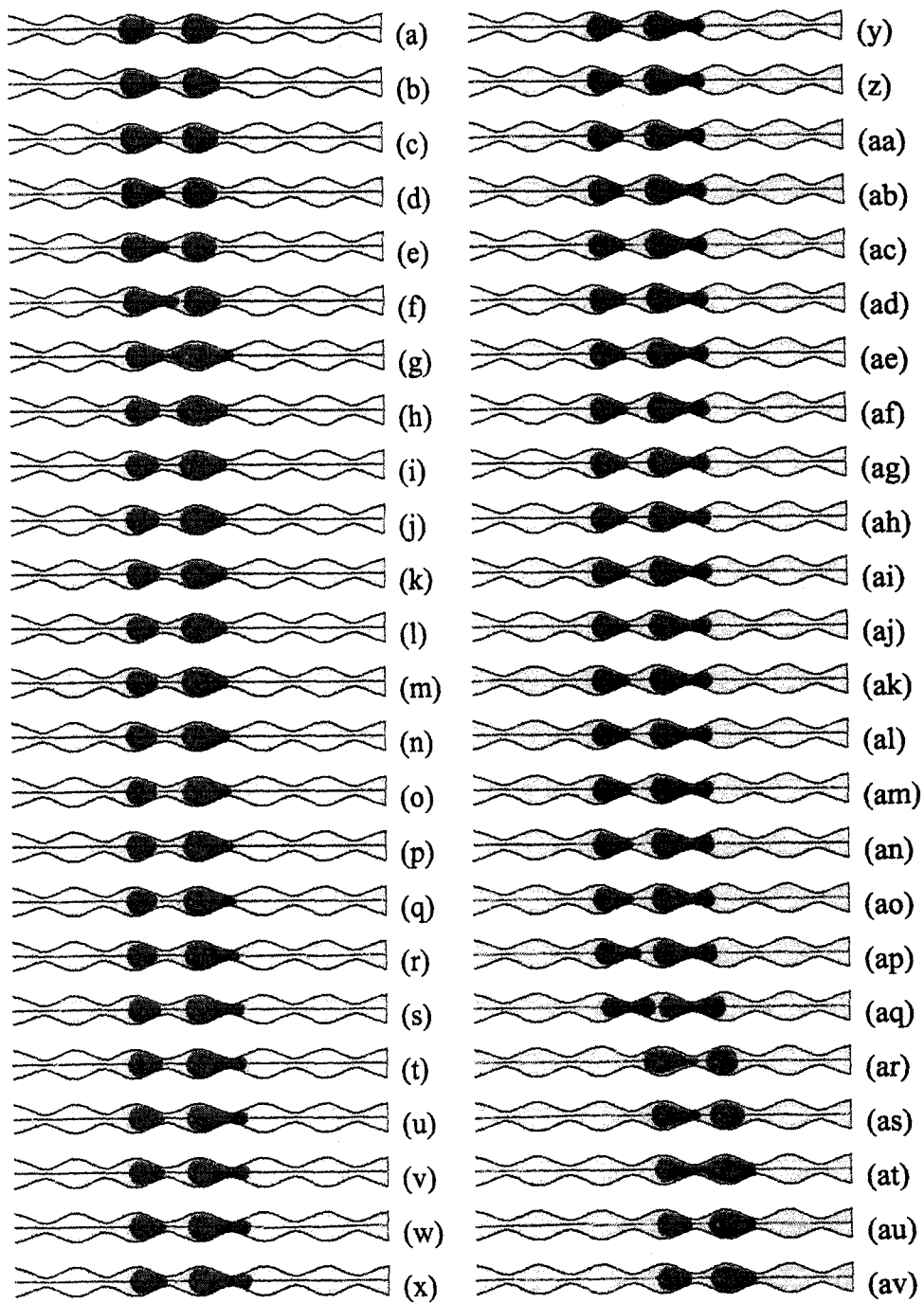


Figure 6.9

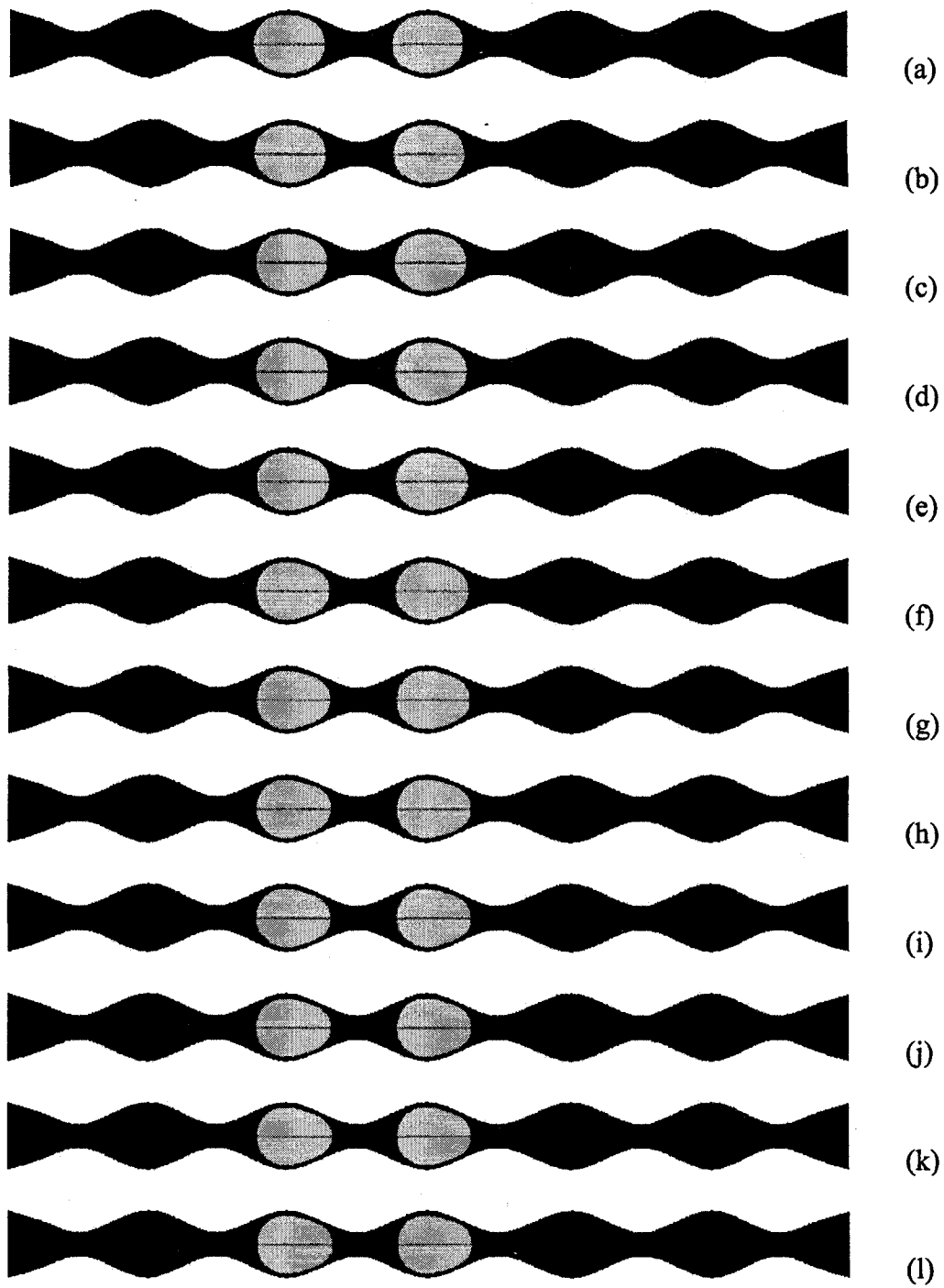
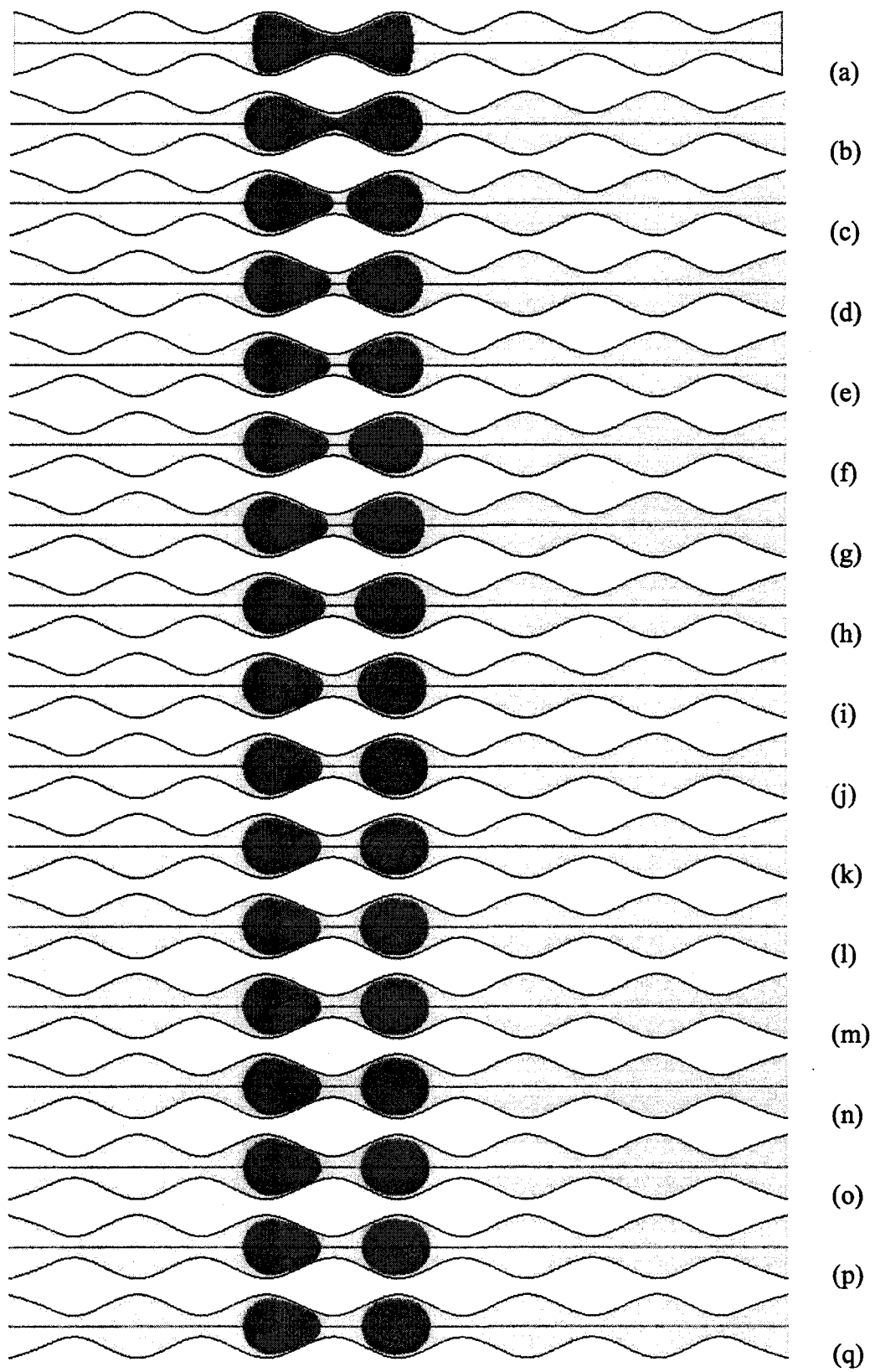


Figure 6.10



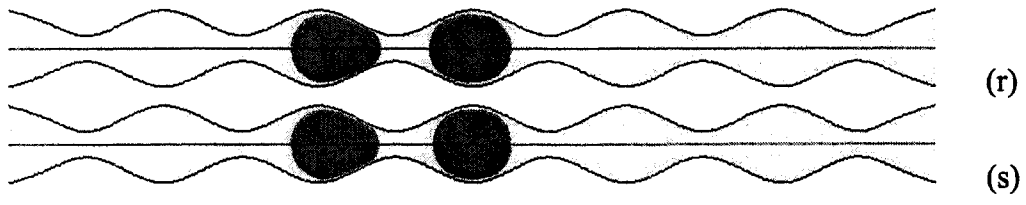


Figure 6.11

## CHAPTER 7. CONCLUSIONS

### 7.1. Summary

Acoustic wave stimulation, such as vibration-induced mobilization, is a promising enhancement approach to remove trapped NAPLs usually encountered in multiphase flows through porous media, especially the remediation of underground water contamination and incomplete petroleum recovery from oil reservoirs, with advantages of high efficiency, low cost and environmental safety relative to the traditional mobilization methods. Numerous experimental and theoretical studies about acoustic wave stimulation have been carried out and several related mechanisms are proposed by investigators, which include but are not restricted to the capillary-physics mechanism, effects of non-Newtonian fluid rheology, removal of liquid films adsorbed on pore boundaries, reduction of surface tension, etc.

According to the simple hypothesized capillary-physics mechanism, specific predictions can be deduced that vibration will be the most effective in mobilizing trapped non-aqueous phase liquids with a comparative higher acceleration amplitude and lower vibration frequency. Moreover, there exists a maximum-acceleration amplitude and minimum-frequency threshold for the mobilization.

A number of quasi-two-dimensional glass micro-model experiments were carried out to validate the predictions following from the capillary-physics mechanism of organic-ganglia mobilization under the influence of low frequency vibration. The experimental results demonstrated that for a fixed acceleration amplitude TCE, the trapped organic phase, was more quickly displaced and flew out in the waterflooding experiment as the vibration frequency decreased from 60 *Hz* to 10 *Hz*. And for a fixed vibration frequency, TCE displacement became more and more efficient as the acceleration amplitude increased from 0.5  $m/s^2$  to 5.0  $m/s^2$ . These findings were consistent with trends predicted by the capillary physics mechanism.

Why the rate of TCE production increases proportionally to the acceleration amplitude and inversely proportionally to the frequency when the whole system is under an appropriate function of vibration? That is because the nudging effect of vibration under

certain conditions can help the ganglia, which would have been trapped in a non-aided regular flow, overcome the capillary obstacle, hence prevent the entrapment of ganglia at any given instant of time, and thereof mobilize the ganglia.

Moreover, a series of well designed simulation experiments were done using a commercial CFD package, FLUENT, to investigate single droplet flow and the related stimulation effects of vibration in a more realistic convergence divergence capillary tube under the combination of fixed and vibratory forces. As for the droplet flow in a constricted capillary tube, an unplugging threshold exists and the value differs from system to system. However, the drop will be trapped if the total external force is less than the release threshold.

Implementing vibration was demonstrated to be more helpful and efficient to mobilize the trapped droplet than a constant external force only under same total forcing level. For a fixed acceleration amplitude, the efficiency would increase as the vibration frequency decreased from 50 *Hz* to 10 *Hz* in terms of average bulk mass flow rate and time percentage when the trapped droplet passing through the constricted area. For a fixed vibration frequency, average bulk flow rate increased and time percentage necessary to mobilize the trapped drop decreased as the acceleration amplitude increased. All of these deduced conclusions based on a more realistic constricted channel were also qualitatively consistent with the predictions following from the capillary physics mechanism and previous studies.

Moreover, the calculations illustrated that longer running time (greater than one period) was a little more helpful for vibrations under a higher frequency than under a lower frequency, with almost no stimulation effect if the frequency was lower than 10 *Hz*.

In all, this work together with the capillary physics mechanism can make it possible to understand the physics of the mobilization effect of low frequency vibration, which can then be applied to the predictions of the stimulation effect in the field after further full parameter space investigations are done.

In addition, analysis of droplet breakup and dynamics in constricted capillary tubes driven by interfacial tension only were carried out to determine how parameters affected droplet breakup in a sinusoidal-wavy-wall capillary tube and to make preparation for further

mobilization-effect study of an elastic wave under the conditions of droplet breakup and oscillatory force.

A simple criterion involving geometrical parameters was derived to determine whether droplet breakup could be initiated in a sinusoidally constricted tube under the condition of no external forces, and the criterion was further validated by numerical calculations and published data.

Also, dynamics of droplet breakup driven by interfacial tension was also studied on some interested parameters such as the characteristics of the geometry, viscosity ratio, density ratio, and interfacial tension between the two immiscible phases. A slowly varying constriction (equivalently a flatter constriction or a longer wavelength of the constriction) resulted in a shorter time to breakup. A higher viscosity ratio increased the time to breakup, but a higher interfacial tension decreased the time to breakup. The effect of breakup dynamic on density ratio was ignorable. Therefore, droplet breakup was shown to be strongly dependent on the shape of the constriction, viscosity ratio, and interfacial tension, but not on density ratio.

Finally, some preliminary studies about the effects on droplet breakup of overlapping external forces such as external pressure gradient were performed. But further investigations are worthy to do on how these external forces including oscillatory force affect droplet breakup and facilitate droplet flow.

## **7.2. Recommendations for future studies**

The work completed so far is still at the beginning, but has laid a solid foundation for future work. Further studies are necessary to generalize the findings and guide the in situ application before low frequency vibratory stimulation can be employed successfully and reliably in the field.

Several issues could be addressed in the two-dimensional quasi micro-model experiments. In particular, experiments should be carried out in a more realistic pore and throat network with media size distributions and special converging-diverging pore geometries typically found in oil reservoirs and/or in underground water aquifers. And some other micro-models with much better flow-distributed guiding areas should be examined and

explored because it is likely that the currently used diagonally etched model had some side effect on the flow. Also, the effects of fluid properties such as the relative densities and relative viscosities, and various porous media properties, as well as interfacial and wetting characteristics such as interfacial tension coefficient and contact angle, are needed to be inspected in a case as close to the field as possible. Moreover, it would be better to understand the physics of mobilization if movement of a single trapped ganglion could be manipulated with specifically designed equipment.

If our goal is extended to gain a complete and comprehensive pore-scale understanding of the mechanisms by which NAPL mobility is enhanced by vibration, three-dimensional experiments should be conducted, using PLIF (Planar Laser-Induced Fluorescence) or PIV (Particle Image Velocimetry) techniques to generate dynamic three-dimensional data sets with pore-scale resolution. Here, a number of factor effects could be examined, such as the size distribution of the packed porous media, the packing pattern of the media, the relatively physical fluid properties, the physical characteristics of the media, etc., as well as the vibration frequency, the acceleration amplitude, and the vibration directions.

As for the numerical calculation part, further studies under much more complex conditions, such as a complicated channel or network of channels consisting of multiple convergence divergence pores and throats with specific size distributions and a large droplet occupying several adjacent pores and throats rather than a smaller droplet in the current study with total volume less than a single pore, can be performed, which is much closer to the on site application. Moreover some other aspects of stimulation effects, such as relative physical fluid properties (densities, viscosities, etc.) and droplet size, can be investigated under the currently simple channel case and the complex channel(s) case. Also, the numerical calculations can be extended to three-dimensional computations with full parameters investigated using more advanced algorithms, higher performance computing, and/or optimization packages.

Furthermore, a much more complex phenomena involving droplet break-up and/or coalescence under external forces such as external pressure gradient, oscillatory forces including elastic waves and vibrations etc., which is expected to enhance trapped ganglion mobilization and bulk flow under specific conditions, should be studied in the future. Full

parameter dynamics study, especially effects of capillary number, distribution of thickness of film between droplet and wall, and resident time under a sinusoidal-wavy-wall capillary tube or other interesting varying constriction, is also worthy to be carried out. Some other issues, such as size distribution of resulting smaller droplets after breakup, dynamics of droplets moving through consecutive constrictions, possible droplet breakup under the condition of no thin film of continuous phase around wall etc., should also be interested to scientists.

## **APPENDIX. PAPER: ELASTIC WAVES PUSH ORGANIC FLUIDS FROM RESERVOIR ROCK**

Igor A. Beresnev, R. Dennis Vigil, Wenqing Li, Wayne D. Pennington,  
Roger M. Turpening, Pavel P. Iassonov, and Robert P. Ewing  
Published in *Geophysical Research Letters*, 32, L13303, (2005)

### **Abstract**

Elastic waves have been observed to increase productivity of oil wells, although the reason for the vibratory mobilization of the residual organic fluids has remained unclear. Residual oil is entrapped as ganglia in pore constrictions because of resisting capillary forces. An external pressure gradient exceeding an “unplugging” threshold is needed to carry the ganglia through. The vibrations help overcome this resistance by adding an oscillatory inertial forcing to the external gradient; when the vibratory forcing acts along the gradient and the threshold is exceeded, instant “unplugging” occurs. The mobilization effect is proportional to the amplitude and inversely proportional to the frequency of vibrations. We observe this dependence in a laboratory experiment, in which residual saturation is created in a glass micro-model, and mobilization of the dyed organic ganglia is monitored using digital photography. We also directly demonstrate the release of an entrapped ganglion by vibrations in a computational fluid-dynamics simulation.

The author of this dissertation performed the experiments where mobilization effect was observed and conducted the numerical simulations of ganglion release by vibrations.

## ACKNOWLEDGEMENTS

First and foremost, I wish to thank my advisor, professor R. Dennis Vigil, for all of his full support, excellent guidance and consistent encouragement throughout this work. I would also like to thank professor Igor A. Beresnev for his tireless efforts to guide, advise and inspire. Without their help, this dissertation would hardly be written.

Also, I wish to thank my committee members, professor James C. Hill, professor Derrick K. Rollins, and professor J. Adin Mann for your services, excellent suggestions and support. Special thank to professor J. Adin Mann for providing some of the equipment used in the experiments, and professor Steve W. Martin and graduate students Jason E. Saienga and Young Sik Kim for annealing the glass plates.

I would also like to thank my group members, Dr. Robert Ewing and Pavel P. Iassonov, for their insightful discussions and suggestions. Also, another group members and fellow graduate students, for stimulating discussions and generous help.

I would also acknowledge my friends and family for your support, love and help all through.

Finally, I wish to thank my wife, Haiguang, Chen, who shared with me the happiness and bitterness in my life. I am deeply grateful for your love, understanding, patience, encouragement, sacrifice, and support.